Nuclear Magnetic Resonance Sensors and Methods for Chemical Sensing in Tissue

by

Ashvin Bashyam

B.S. Biomedical Engineering
The University of Texas at Austin (2014)

Submitted to the
Department of Electrical Engineering and Computer Science
in Partial Fulfillment of the Requirements for the Degree of

Master of Science in Electrical Engineering and Computer Science
at the
Massachusetts Institute of Technology

June 2016

Signature of Author ..... Signature redacted .....
Department of Electrical Engineering and Computer Science
May 19, 2016

Certified by..... Signature redacted .....
Michael J. Cima
Professor, Department of Materials Science and Engineering
Thesis Supervisor

Accepted by ..... Signature redacted .....
Leslie A. Kolodziejski
Chair, Department Committee on Graduate Students

Nuclear Magnetic Resonance Sensors and Methods for Chemical Sensing in Tissue

by

Ashvin Bashyam

Submitted to the Department of Electrical Engineering and Computer Science
On May 19, 2016 in Partial Fulfillment of the
Requirements for the Degree of Master of Science in
Electrical Engineering and Computer Science

Abstract

Rapid, sensitive, and minimally invasive sensing of metabolites, chemicals, and biological molecules within tissue is a largely unsolved problem. Sensing molecular oxygen, pH, and water content is of particular interest as they have been shown to be useful for improving disease diagnosis and treatment monitoring in a diverse range of medical fields including trauma, solid tumor cancers, tissue grafts, wound healing, dehydration, athletic performance, and congestive heart failure.

Nuclear magnetic resonance (NMR) offers a non-ionizing, rapid, repeatable, and molecularly sensitive measurement technique for chemical sensing. Existing hardware for highly versatile single sided measurement systems is insufficient for clinical use due to constraints on the size and shape of samples that can be measured, inadequate magnetic field performance, and low sensitivity.

This thesis describes the development of a portable, single-sided NMR system for research and clinical use. A magnet assembly based on a linear Halbach array was developed to produce a large, remote, and uniform field. Suitable impedance matching circuitry was designed and constructed to efficiently transmit signals between NMR probes and a radiofrequency spectrometer. This system is suitable for use in NMR measurement within a clinical environment.

Thesis Supervisor: Michael J. Cima
Title: Professor, Department of Materials Science and Engineering

Contents

List of Figures

List of Tables

This page intentionally left blank

Chapter 1

Clinical motivation

Rapid, sensitive, and minimally invasive sensing of metabolites, chemicals, and biological molecules within tissue is a largely unsolved problem. The ability to sense the concentration of clinically relevant biomarkers *in vivo* with longitudinal stability would revolutionize clinical practice across a wide range of medical specialties. Sensing molecular oxygen, pH, and water content is of particular interest as they have been shown to be useful for improving disease diagnosis and treatment monitoring in a diverse range of medical fields including trauma, solid tumor cancers, tissue grafts, wound healing, dehydration, athletic performance, and congestive heart failure [1]–[4].

1.1 Tissue oxygenation and pH

Measurement of the concentration of molecular oxygen and pH within tissue is useful for diagnosing, staging, and guiding treatment of a multitude of pathologies such as cancer, trauma, and acute compartment syndrome.

1.1.1 Tumor oxygenation and pH

Hypoxia, a hallmark of solid cancer tumors, is a strong indicator of how a patient responds to chemotherapy and radiotherapy due to its relation to tumor metabolism, perfusion, sensitivity to radiation, and metastatic potential [5]. Furthermore, these tumors are often more acidic than normal tissue since poorly perfused cells, especially towards the center of the tumor, undergo anaerobic respiration which produces lactic acid [6]. The pH of the environment immediately surrounding the affected cells decreases during successful administration of chemotherapeutic agents [7]. A precise, highly localized measurement of intratumoral oxygenation and pH is critical for more nuanced treatment planning [8], [9]. Currently, there is no reliable predictor of response for many cytotoxic chemotherapeutic drugs and, therefore, patients are often treated with multiple lines of therapy. This inefficient approach incurs significant economic cost and impacts therapeutic success rates [10], [11]. A highly-localized, longitudinal measurement of tumor pH and oxygen levels would provide clinicians with unprecedented insight into the relative progression of the tumor, potential for metastasis, and efficacy of chemotherapy significantly before those results would otherwise manifest themselves [12].

1.1.2 Acute compartment syndrome

Acute compartment syndrome, caused by restricted flow into a muscle compartment is a significant secondary injury after crush trauma, fractures – especially of the lower leg, and vascular disease [13], [14]. It results in significant morbidity which includes neurological deficit, permanent disability, tissue necrosis leading to amputation, and even death. The most effective therapy is a fasciotomy, a highly invasive surgical procedure that relieves the pressure within the compartment to restore flow. Oftentimes, these surgeries are performed preventatively due to a lack of information on tissue health [15]. The current standard of care, an invasive pressure probe and a physical exam, oftentimes inaccurately predicts the severely of injury [4], [16]. Measuring oxygen tension within the compartment would provide physicians with a predictive indicator of disease progression [13].

1.1.3 Methods for assessing tissue oxygenation and pH

The best efforts, to date, at in vivo oxygen and pH monitoring have failed to provide a robust, long-term, and minimally invasive solution without significant shortcomings that have limited their clinical applicability.

1.1.3.1 Electrode probes

Commonly-used electrode probes for both oxygen and pH sensing involve significant invasiveness in reaching the target location and cannot be used over extended time periods due to infection risk, patient discomfort, and signal degradation from the foreign body response [17]. Further, the Clark electrode, the standard for electrode-based oxygen sensing, consumes oxygen which perturbs the environment in which sensing is taking place.

1.1.3.2 Positron emission tomography (PET)

PET imaging, which relies upon detection of anti-parallel photons produced by an annihilation event between an emitted positrons from an exogenous contrast agent, can only detect deficiencies, not excesses, of oxygen [18]. These specialized radiotracers, such as ^{18}F-fluoromisonidazole, have an associated toxicity due to their emission of radioactive positrons and the additional load they place on the renal system as they are cleared from the body. PET does not have high spatial resolution and cannot directly measure the partial pressure of oxygen.

1.1.3.3 Optical fiber based sensor

An optical fiber tipped with an oxygen-dependent lifetime fluorescent dye, such as ruthenium chloride, can measure oxygen tension at the tip of the probe [18]. This technique provides a rapid and accurate measurement of oxygen concentration, but

is unable to provide longitudinal measurements due to its invasiveness. Spatially correlated longitudinal measurements are critical to reduce variability in measurement from probe placement and reduce induced trauma to tissue from repeated probe insertion.

1.1.3.4 Diffuse optical techniques

Optical techniques for pH and oxygen sensing have very limited penetration depth which restricts their applicability when considering deep muscle compartments and solid tumors [19], [20]. Pulse oximetry, the most well-known optical oxygenation sensor, requires well-perfused tissue with pulsatile blood flow, is inaccurate for low blood oxygenation levels, and is unable to perform precise spatial localization [19], [21]. Diffuse optical tomography, commonly used to assess perfusion levels in a variety of pathologies, is unable to provide a direct measure of molecular oxygen concentration as it relies on the change in absorbance of hemoglobin as it is oxygenated [22], [23]. These techniques are not viable in cases of poor or no perfusion as is often the case during compartment syndromes or within solid tumors.

1.1.3.5 Nuclear magnetic resonance based techniques

Previous efforts have led to the development of contrast agents for oxygen and pH [24], [25]. Oxygen contrast agents were designed based on measurement of changes in relaxation time of paramagnetic oxygen with siloxanes. pH contrast agents were designed based on sensing changes in the rate of proton exchange with a polymer. These contrast agents allow measurement of the presence and concentration of chemical species to which proton NMR is not intrinsically sensitive.

Although an MRI scan is theoretically sensitive enough to measure the relaxation rates of small depots of these contrast agents within tissue, there are numerous barriers to practical implementation of this strategy in clinical use. Most importantly, sensitivity limitations require relatively large depots to be injected and long scan times which precludes precise use in particular applications where accurate spatial localization is required. The exceptionally high cost associated with MRI limits accessibility and widespread adoption. Furthermore, migration of the contrast agent over time precludes longitudinal use and quantitative measurements due to bulk migration of the depot as well as diffusion into surrounding tissue.

A biopsy implantable sensor, filled with the relevant contrast agent, would be capable of improving measurement sensitivity and localization of pH or oxygen [26]. This sensor, implanted into the tissue through a standard biopsy needle, would be interrogated through inductively coupled NMR performed from an external reader.

Longitudinal measurements of its contents would be possible opening new opportunities in preclinical and clinical research.

1.2 Fluid volume status

Maintenance of fluid balance in the body is critical to physical and cognitive function yet no accurate, robust, and practical assessment method currently exists. Healthy individuals can correct for fluid volume fluctuations through ingestion and excretion of fluids under normal conditions, however changes in disease state, stress, age, and environmental conditions can affect the ability of individuals to regulate their fluid status. Proper fluid management is especially necessary for renal and heart failure patients, competitive athletes, soldiers, and the elderly. Current approaches rely on indirect measures that are subject to significant variability during physician interpretation or invasive measures that cannot be routinely performed. There is a clear need for an improved technique to measure fluid volume status.

1.2.1 Fluid volume overload

Overload of fluid volume, or volume expansion, occurs due to changes in the ability of the body to regulate its ion and fluid balance. Frequent causes include heart failure, kidney failure/nephrotic syndrome, and liver failure/cirrhosis [27]. Inflammatory pathologies that may lead to nephrotic syndrome or chronic renal disease impairs water excretion function increases vascular volume and leads to edema [28]. Decreased cardiac output decreases blood pressure in cases of heart failure. Baroreceptors react to this decreased blood pressure by increasing renal water retention to raise vascular fluid volume. Once again, increased vascular fluid volume eventually leads to edema [28]. Cardiac decompensation may occur, if edema is left untreated, which significantly increases patient mortality [29].

Initial progression of fluid overload begins with increased vascular fluid volume and subsequent tissue edema. Further fluid accumulation increases cardiac load which threatens cardiac decompensation in heart failure patients [30]. Edema decreases tissue function due to increased diffusion distance for incoming nutrients and outgoing waste products. Edema in encloses spaces, such as the skull and muscle compartments, can increase interstitial pressure which impairs function and threatens viability due to restriction of vascular and lymphatic flow.

1.2.2 Fluid volume depletion

Depletion of fluid volume, or volume contraction, occurs due to changes in the ability of the body to regulate its ion and fluid balance. Frequent causes include vomiting, decreased cardiovascular function sweating, urination, diarrhea, severe

burns, kidney failure, and disrupted thermoregulation. Under normal conditions, recovery is straightforward through oral rehydration [31]. In more extreme scenarios involving exercise without fluid replacement, diminished thirst perception caused by mental or environmental stress or physiological changes from aging, more aggressive fluid replacement may be necessary. Decreased thirst perception has been known to occur in competitive athletes, soldiers, and elderly populations for differing reasons. In athletes and soldiers, the simultaneous loss of water and sodium allows plasma osmolality to remain constant [32], [33]. Further central blood volume can be elevated during physical activity. In the elderly, the exact etiology is unknown although it is hypothesized to be related to decrease nervous and renal system function [34].

Symptoms of fluid volume depletion begin with thirst, changes in skin turgor, and sometimes dry mucous membranes. Moderate dehydration can induce tachycardia, hypotension, and decreased blood pressure. In severe cases, shock (tachypnea, tachycardia, hypotension, confusion, poor capillary refill) and unconsciousness can occur [27].

1.2.3 Methods for assessing fluid volume status

A wide range of approaches have been considered for assessment of fluid volume status. These methods are based on biological changes, chemical changes, and physical changes driven by fluctuations in fluid volume status. None ultimately succeed at providing clinicians with a robust, rapid, non-invasive, and accurate measurement suitable for use in guiding clinical interventions.

1.2.3.1 Physical markers

Total body weight has shown some diagnostic value for fluid overload, especially in the congestive heart failure population. Frequent measurements hold some predictive power for hospital admissions [35]. However, a large number of strongly confounding factors such as changes in muscle mass, fluid redistribution, changes in diet, and other comorbidities reduce the accuracy of this test [36]. It will likely find continued use despite the development of other techniques, due to its simplicity and cost effectiveness.

Skin turgor assessment physically tests the elasticity of skin as an indirect indicator of fluid volume status. The rate of recoil of skin after pinching between the examiners fingers indicates the hydration state of the patient [37]. This technique is not quantitative and relies upon the assumption that skin elasticity is solely influenced by the hydration state of the patient [38]. It has poor diagnostic utility, especially in cases of limited dehydration, as the changes in skin elasticity may not be present.

Mucous membranes, epithelial cell layers that secrete mucus, remain wetted except in cases of dehydration. Visual examination of easily accessible mucous membranes – skin, mouth, and nasal cavity – can be indicative of dehydration [39]. However, this examination has very low specificity as mucous hydration exhibits significant variability between individuals [40]. Additionally, this test can only indicate dehydration and relies on a trained professional precluding widespread use.

Peripheral pitting edema, swelling from interstitial fluid accumulation, can be observed in the lower extremities of patients suffering from fluid overload. It is evaluated qualitatively by evaluating the presence of pitting after pressure is applied to the tissue [41]. Furthermore, it is easily confounded due to changes in blood vessel tone and changes in lymphatic and renal system function. Due to its poor sensitivity and qualitative nature, it is unable to provide treatment modifying diagnostic information [42].

Jugular venous distension (JVD), a qualitative technique used to asses fluid overload in congestive heart failure patients, relies upon reduced filling pressures to create venous congestion which ultimately affects the height of the visible jugular vein [43]. This technique is dependent on a qualitative visual assessment and therefore suffers from poor sensitivity and is highly susceptible to confounding factors such as the presence of excessive adipose tissue, body position, and subjective interpretation of results [44], [45]. Further, studies have indicated poor specificity as an elevated JVD was not present in 50% of congestive heart failure patients [46]. This technique is highly dependent on specialized training which precludes its use in an outpatient or home setting.

Generally, these techniques lack the precise sensitivity and specificity of other techniques due to lack of quantitative outcomes and evidence-based metrics on which to base diagnoses [47].

1.2.3.2 Physiological markers

The total amount of water within the body, known as total body water, is a useful indicator of the hydration status of a patient though rapid and accurate measurement is difficult. One method of assessment involves administering a deuterium bolus intravenously and measuring its concentration within the blood as it is distributed throughout the body. Deuterium spreads throughout the body into all tissue compartments and, therefore, indicates the extent of its dilution can be used to find total body water [48]. Unfortunately, this technique relies upon empiric models which may not extrapolate well to different demographic groups [49]. Further the time to equilibration can be up to 10 hours which precludes its use as a rapid or acute measurement technique [50].

Blood volume, and therefore hematocrit over a limited time interval, can fluctuate in response to fluid volume overload or depletion. Hematocrit variations have been associated with increased mortality in kidney and heart failure patients [51]. Hematocrit measures are highly susceptible to orthostatic confounding factors as such the position of the patient [52]. Hematocrit is highly controlled by physiological compensatory mechanisms which seek to maintain intravascular volume and cardiac output. This limits the applicability of hematocrit as an indicator of fluid volume status. The poorly characterized time dependency of the measurement and the strong tendency of homeostasis to attempt to maintain intravascular volume limits its use as a direct indicator of fluid volume status, especially in mild and moderate cases [53].

Plasma volume, similarly to total body water, can indicate total body water and intravascular volume. Therefore it can serve as an indicator of fluid volume status [54], [55]. The concentration of an intravenously infused dye, such as Evans blue which preferentially binds albumin, can be measured as it equilibrates primarily within the plasma to indicate total plasma volume. This technique relies upon a baseline that can vary significantly between individuals and requires extended time periods to produce accurate results [56]. Similarly, to blood volume, plasma volume is highly conserved to maintain blood volume. Changes in plasma volume can be easily confounded by environmental factors such as temperature and physical exertion [57].

Plasma osmolality represents the electrolyte-water balance within the body and has found use in measuring hydration state in patients despite the presence of considerable confounding factors [58]. Most importantly, plasma osmolality is highly regulated which reduces its variability in response to changes in fluid volume status. Differences in measurement protocol, especially timing of measurements, significantly affects its accuracy. Furthermore, significant variation in the response of plasma osmolality to fluid loss across patient populations limits is applicability as a diagnostic tool [59].

Several physical properties of urine including its color, osmolality, specific gravity, and conductivity have been shown to indicate fluid volume status [60]. Measurements of urine are more favorable than many other methods due to the low associated cost and lack of invasiveness. While these indicators act as reliable indicators in some cases, their sensitivity is very poor, especially in cases of hyperhydration [61]. There is also a time delay associated with both the production of urine and the presentation of changes in fluid volume status in urine which limits the utility of urine based measurements in acute cases [61]. Changes in urine are easily confounded by changes in diet, recent fluid ingestion, timing of measurement, and the presence of other indications impacting metabolism, circulation or renal clearance.

Many of these techniques elucidate a fundamental physiological metric directly affected by fluid balance within the body. The very strong compensatory mechanisms in the body preclude highly sensitive observation of physiology as an indicator of fluid volume status except in severe cases or when these homeostatic mechanisms have failed.

1.2.3.3 Biochemical markers

Atrial natriuretic peptide (ANP), a vasodilator secreted by the heart, increases in response to volume overload as a result of increased atrial transmural pressure [62]. Its wide variability and poor correlation with extracellular volume preclude its use as a clinical diagnostic [63]. ANP levels are not responsive to hypovolemia and therefore can only be used in cases of volume overload.

Cyclic GMP (cGMP), the second messenger to ANP, has been shown to correlate with increased plasma volume and fluid overload [64]. Despite this, high variability between patients and the existence of other confounding factors limits its clinical utility. Similarly to ANP levels, cGMP levels are not responsive to hypovolemia limiting their utility to cases of volume overload [47].

Brain natriuretic peptide (BNP), secreted by the heart ventricles, concentrations in circulation have been shown to be elevated in overloaded patients [62]. BNP has demonstrated value in diagnosing cardiac and renal disease progression [65], [66]. BNP may not be suitable for use in patients undergoing more acute changes in fluid volume status [67].

These techniques are easily confounded by other indicators, show a lack of specificity towards changes in fluid volume status, and have limited utility in acute cases due to their slow temporal response.

1.2.3.4 Imaging techniques

Ultrasound imaging of the diameter of the inferior vena cava and the aorta has demonstrated success as a measure of fluid status in children [68]. This technique cannot be performed in patients with altered cardiovascular function, such as those suffering from congestive heart failure or tricuspid regurgitation. Furthermore, the timing of the measurement impacts its accuracy, thus limiting its applicability to acute cases. Ultrasound techniques require the availability of equipment in most clinical settings and a specially trained operator which limits accessibility and affordability. These techniques are susceptible to variability in probe positioning which is often poorly controlled in clinical settings [69].

Bioimpedance and impedance cardiography, measurements of the impedance of flow of applied electrical current at various frequencies by the body, can detect shifts in

fluid associated with acute heart failure and normal hemodynamic shifts [70], [71]. Significant variability in these measurements creates significant difficulty in widespread adoption of impedance cardiography to monitor heart failure patients [71]. The reliance of the technique on empirically generated values limits its applicability to well-studied patient populations under controlled environments [72], [73]. This technique is highly susceptible to timing when used in patients undergoing acute fluid volume change due to dialysis [47].

1.2.3.5 Nuclear magnetic resonance

^{1}H NMR relaxometry, the measurement of the rate of nuclear relaxation of protons within the sample, provides a direct measure of water volumes and concentration. The nucleic specificity of MR intrinsically measures only signal from water, which vastly improves sensitivity compared to other, easily confounded diagnostic methods. Magnetic resonance imaging (MRI) can measure fluid levels, as demonstrated in patients undergoing diuretic treatment, but is highly impractical for routine diagnostic use due to extended measurement times, high cost, and limited availability [74]. NMR relaxometry has been demonstrated as a tool to measure both dehydration and fluid-overload in mice using tabletop sensors [75], [76].

Multiple unique mechanisms of sensing fluid volume status have been proposed. The balance of water between the interstitial and intracellular space has been observed to fluctuate predictably in response to changes in body hydration levels [77]. Suitably high sensitivity NMR relaxometry could measure the relative contribution of water located in each of these compartments [78], [79].

Hematocrit, the fraction of blood volume composed of erythrocytes, can be measured via NMR as shifts in relaxation times [80]. Dehydration has been shown to elicit changes in hematocrit during exercise in healthy subjects [81]. This suggests that NMR relaxometry could provide a noninvasive, rapid measurement of hydration state through hematocrit measurements. These measurements would be subject to similar confounding factors as existing clinical hematocrit measurements such as homeostatic compensation.

1.3 Thesis overview

Effective NMR based measurement of oxygen and pH in the body using inductively coupled implanted resonators and the measurement of fluid volume status both rely upon a robust, high sensitivity system for performing NMR relaxometry measurements in living subjects. Existing NMR hardware does not suitably balance measurement capabilities, ability to image on various anatomical locations, portability, and robustness in various environmental conditions. Magnetic

resonance imaging systems, while capable of producing exquisite images of human anatomy and functional activity, are very expensive, require dedicated space within the imaging facility, and are not conductive to fast measurements due to the significant calibration required before a scan. Laboratory NMR spectrometers produce high signal to noise ratio NMR measurements of a sample, but are unsuitable to measuring most anatomical regions (such as the upper leg, lower leg, arm) due to their enclosed measurement bore. Furthermore, they are typically not portable or cost effective, precluding widespread clinical use. One commercially available single-sided NMR measurement system, the NMR-MOUSE, is not conducive to high sensitivity measurements over a large volume of tissue as its uniform region of its magnetic field is very thin [82].

There is a clear need for a single-sided NMR system capable of producing high sensitivity measurements of a wide variety of samples. This will allow further investigation in the best methods for measurement of oxygen, pH, and hydration within tissue at various anatomical sites.

1.3.1 Single sided magnet

Existing single-sided magnets – those that can produce a region of magnet field remote from and unenclosed by the magnet – such as the NMR MOUSE, while capable of taking measurements on large objects, have a very thin sensitive region which limits sensitivity and, therefore, places a maximum bound on the signal to noise ratio [82]. Furthermore, the depth of the uniform region in the NMR MOUSE is not sufficient to measure tissue compartments beyond the dermis and subcutaneous layers which may prove essential to accurate determination of physiological conditions.

Chapter 3 details the design, construction, and testing of the single sided magnet for a portable NMR measurement system for laboratory and clinical use designed to measure relaxation times with high signal to noise ratio within a sensitive region located tens of millimeters inside of tissue. It begins with a discussion of the design problem for this single sided magnet and then considerations in magnet and material selection. The theoretical basis for the magnet geometry is then introduced. The numerical simulation used to model the field profile of the magnet is introduced. Results of numerical simulations help understand the influence of each dimension of the magnet on its performance. Magnet dimensions are then set by making trade-offs in various performance metrics based on the results of these simulations. A discussion of the impact of temperature variation and a solution to this through active temperature regulation is detailed. The process of construction of the magnet is discussed along with special efforts to assist in assembly. The magnet assembly is characterized and differences between simulation results are discussed.

1.3.2 RF impedance matching circuit

Chapter 4 motivates the circuit that interfaces the spectrometer to the transceiver coil along with detailing its theoretical basis, design, fabrication, and testing. Efficient power transmission into the transceiver coil as well as high sensitivity measurement of the induced current with the coil requires precise impedance matching of the spectrometer and the NMR probe. The theory and design principles of a simple, tunable RF impedance matching circuit for single sided NMR are discussed. A mechanical and electrical design for the circuit and its housing is detailed along with experimental validation of the performance of this circuit.

This page intentionally left blank

Chapter 2

Nuclear magnetic resonance

Nuclear magnetic resonance (NMR), the same physical phenomena behind magnetic resonance imaging, offers a non-ionizing, rapid, repeatable, and molecularly sensitive measurement technique for chemical sensing within tissue. Its broad range of contrast mechanisms are robust to measurement through opaque, conductive and heterogeneous biological tissue.

2.1 Physical phenomena

Nuclear magnetic resonance (NMR), discovered by Bloch and Purcell in 1945, describes the process where atomic nuclei in a magnetic field absorb and emit electromagnetic radiation at a specific resonant frequency [83], [84]. This resonant frequency is dependent on both the strength of the applied magnetic field and the magnetic properties of the particular species of interest and relies on the system possessing both magnetic moments and angular momentum. NMR allows the investigation of atomic properties not generally accessible via other measurement techniques and has found applications in chemistry, molecular physics, biology, medicine, and other sciences [85].

This thesis relies upon a classical description of ^{1}H NMR which is justified because ^{1}H is a spin-1/2 system, samples contains a very large number of spins (~10^{20}), and all samples are at a suitably high temperature (~300 K) [83]. Therefore, the net magnetization vector can be described by a continuously varying vector rather than a discrete, or quantized, system. ^{1}H NMR was selected as hydrogen is the most abundant atom in the body and, therefore, provides the strongest NMR signal. Contrast agents can be readily designed to modulate the relaxation times (T1 or T2) in an ^{1}H NMR system in response to changes in environmental conditions.

2.2 NMR signal origin

2.2.1 Static magnetic field

Nuclear magnetic resonance measurements depend on the precession and alignment of the nuclear spins of the sample of interest. To achieve this alignment, an external magnetic field, $\vec{B}_0 = B_0\hat{z}$, must be applied to the sample in the direction.

The axial or longitudinal direction, $\hat{z}$, is the direction in which the static magnetic field is applied by convention. The transverse plane is defined as the xy plane.

This applied magnetic field creates a net magnetization vector, $\vec{M}_0 = M_0\hat{z}$, aligned with the magnetic field, created by aligning the spins of the nuclei of atoms within the sample. The strength of this net magnetization vector is proportional to the applied magnetic field, $\vec{B}_0$, and is given by,

$$M_0 = \frac{\gamma^2\hbar^2}{2k_B}\frac{N}{T}B_0 \tag{2.1}$$

where the sample, maintained at a temperature, T, contains N protons and the nuclei of interest have a gyromagnetic ratio, γ; $\hbar$ is the reduced Planck constant and k_B is the Boltzmann constant. This expression comes from taking the ratio of the occupation probabilities of nuclei between the two spin states ($m = \pm 1/2$) based on the Boltzmann distribution [86].

2.2.2 Nuclear precession

The gyromagnetic ratio, γ, relates the strength of the applied static magnetic field and the frequency of precession of the nuclei, known as the Larmor frequency, as shown by,

$$\omega = \gamma B_0 \tag{2.2}$$

where ω is the angular frequency of precession of the nuclei. This precession occurs due to the balance between the force of the static magnetic field aligning the magnetic moment and the angular momentum of the nuclear spins. This work focuses on hydrogen nuclei, ^{1}H NMR, and therefore is concerned only with the $\vec{M}_0$ created by hydrogen nuclei. Therefore, the gyromagnetic ratio can be expressed by the following,

$$\gamma = g_p\mu_n/\hbar \tag{2.3}$$

where g_p is the g-factor of a proton, a proportionality constant that relates the magnetic moment of a particle to its angular momentum quantum number and a unit of magnetic moment, and μ_N is the nuclear magneton, a physical constant of magnetic moment. The gyromagnetic ratio for a proton is approximately equal to 42.576 MHz/Tesla which sets the basis for the radio frequency electromagnetic excitation of the sample in an NMR experiment.

2.2.3 RF electromagnetic pulse

An applied electromagnetic field, $\vec{B}_1(t)$, oriented perpendicularly to $\hat{z}$, oscillating at the frequency of the precession of the protons within the sample, is used to perturb the net magnetization vector. This applied electromagnetic field can be defined as

$$\vec{B}_1(t) = B_1(\cos(\omega t)\,\hat{x} + \sin(\omega t)\,\hat{y}) \tag{2.4}$$

where B_1 is the magnitude of the pulse.

The angle of rotation of the net magnetization vector is given by

$$\phi = \gamma \int_0^{t_p} B_1(t)dt \tag{2.5}$$

where ϕ is the angle of rotation and t_p is the pulse duration. The expression for the angle of rotation simplifies in the case of a uniform intensity B_1 pulse, given by

$$\phi = \gamma B_1 t_p \tag{2.6}$$

Two commonly used electromagnetic pulses aim to rotate the net magnetization 90° into the transverse direction (onto the xy plane) or 180° into the negative longitudinal direction. For a constant amplitude pulse, the duration and the amplitude of the 90° pulse are related by

$$t_{90} = \frac{\pi}{2}\frac{1}{\gamma B_1} \tag{2.7}$$

and the 180° pulse duration and the amplitude, simply twice that of a 90° pulse, by

$$t_{180} = \pi\frac{1}{\gamma B_1} \tag{2.8}$$

where t_{90} and t_{180} are the duration of a 90° and 180° pulse, respectively.

2.2.4 Rotating frame of reference

A rotating frame of reference provides a convenient method by which to analyze the magnitude and orientation of $\vec{M}_0$ as a function of time, especially since the time scale time over which $\vec{M}_0$ changes its magnitude is much slower than the time scale over which it changes orientation within the transverse plane. This rotating frame of reference rotates at the Larmor frequency around the z axis. The $\hat{z}$ vector still points in the longitudinal direction, but now $\hat{r}$ describes a vector on the xy plane that rotates at the Larmor frequency. Therefore, the electromagnetic pulse can simply be described as $\vec{B}_1(t) = B_1\hat{r}$.

2.2.5 Induced current from precession

The transverse component of the net magnetization vector, oriented alone the xy plane, precesses around the z axis at the Larmor frequency. This procession induces a voltage in a loop of wire, or a coil, oriented parallel to the xy plane. This induced voltage is proportional the time derivative of the change in magnetic flux through the current loop, as stated by Faraday's law of induction. The induced voltage is given by

$$\varepsilon = \omega M_0 \hat{B}_1 \tag{2.9}$$

where ε is the induced voltage and $\hat{B}_1$ is the magnetic field at the sample created by passing a unit current through the receiver coil.

This analysis assumes that the sample is homogenous, the static magnetic field is constant and also homogenous across the sample, and the applied electromagnetic pulse is of uniform amplitude.

2.3 Magnetic relaxation

The net magnetization vector is in equilibrium when it is aligned with the static magnetic field. Upon application of the electromagnetic pulse at the Larmor frequency, the magnetization vector rotates away from this equilibrium position. Its amplitude immediately begins to both decrease in the transverse direction and increase in the longitudinal direction until it has returned to equilibrium. This process is known as relaxation and forms the basis for the signals measured in pulsed NMR experiments.

This process of relaxation can be characterized by two time constants as shown by Bloch [83]. The first, known as spin-lattice relaxation or longitudinal relaxation, is denoted as T_1. The second, known as spin-spin relaxation or transverse relaxation, is denoted as T_2. The initial equilibrium state of the magnetization vector is assumed to be $\vec{M}(t) = M_z(t) + M_r(t) = M_z(t) + M_{xy}(t) = M_0\hat{z} + 0\hat{r}$. Following the application of a 90° pulse, the magnetization vector can be described as $\vec{M}(t) = 0\hat{z} + M_0\hat{r}$. Longitudinal relaxation causes the component of $\vec{M}(t)$ oriented along the $\hat{z}$ direction to increase with time as shown by

$$M_z(t) = M_0\left(1 - e^{-t/T_1}\right) \tag{2.10}$$

where t indicates the time since the application of the 90° pulse and T_1 is the longitudinal relaxation time. Transverse relaxation simultaneously causes the component of $\vec{M}(t)$ oriented along the $\hat{r}$ direction to decrease with time as shown by

$$M_r(t) = M_0 e^{-t/T_2} \tag{2.11}$$

where T_2 is the transverse relaxation time. Values for T_1 and T_2 can range from as short as a few milliseconds to as high as several seconds depending on the structure, composition, and state of the material in which the observed protons are located. Relaxation times are oftentimes dependent on the strength of the static magnetic field, B_0.

The rate of relaxation can be affected by a broad range of physical and chemical phenomena which can be taken advantage of to measure the intrinsic characteristics of a sample. Alternatively, a material that exhibits a well characterized change in relaxation time in response to an environmental change can be observed to infer information about its local environment. This forms the basis for the NMR contrast agents necessary for oxygen and pH sensing discussed previously. A single or multi component exponential function is fit to the acquired free induction decay signal in order to extract useful information. The results of this fit can indicate the values of T_1 or T_2 depending on the pulse sequence applied to the sample.

This page intentionally left blank

Chapter 3

Magnet design for single sided NMR

Successful NMR measurements are dependent upon the presence of a static magnetic field to magnetize the sample. The mere existence of a magnetic field, while sufficient to magnetize the nuclei of the sample, is not sufficient to produce a high sensitivity NMR measurement. Only nuclei that share a similar Larmor frequency can be excited by a single B_1 pulse. A large and uniform magnetic field is essential to induce precession of a large number of protons at the same Larmor frequency. For a clinical NMR measurement system, the size of this uniform region must be well controlled to best suit the anatomy in which it will be applied. A convex uniform region with a highly regular shape provides a straightforward region of tissue over which the B_1 pulse needs to be applied. This region will be easy to characterize and localize when identifying the anatomical region over which the measurement is being taken. Measuring particular anatomical regions of interest, such as lean muscle tissue, requires that the magnetic field extend beyond the subcutaneous regions.

We hypothesized that an array of rare-earth permanent magnets arranged as a linear Halbach array would be capable of producing a suitable uniform field. An investigation into the effect of varying the defining parameters of the linear Halbach geometry was undertaken. The results of this were used to design an optimal magnet array that achieved the design goals.

3.1 Magnet selection

Initial approaches to designing a magnet capable of producing a suitably strong magnetic field in clinical conditions considered both superconducting coils as well as permanent magnets. Robust operation in a clinical, home, or field environment precluded the use of superconducting coils – both due to the high current requirements and the significant infrastructure required to keep the coils sufficiently cold.

Neodymium iron boron permanent magnets were selected over other options, such as samarium cobalt, alnico, and ceramic or ferrite magnets due to their high energy product range and coercivity which allows them to be very strongly magnetized and resist demagnetization. These magnets can be readily manufactured into precisely controlled shapes with high tolerances of dimensions, magnetization strength, and

magnetization orientation. The major disadvantages of neodymium magnets, its relatively high temperature coefficient and low Curie temperature compared to samarium cobalt magnets, are not important design criteria as the system will not experience significant temperature fluctuations during use.

Type of magnet	Neodymium iron boron	Samarium cobalt	Alnico	Ceramic or ferrite
Maximum energy product [T*A/m * 10^6]	0.75 – 3	0.4 – 1.4	0.12 – 0.4	0.02 – 0.2
Remanence [T]	1 – 1.5	0.8 – 1.1	0.6 – 1.4	0.2 – 0.5
Coercivity [A/m * 10^6]	0.75 – 2	0.5 – 1.3	0.2 – 0.3	0.1 – 0.3
Curie temperature [K]	600	1100	1100	700
Temp. coefficient of remanence [%/K]	−0.12	−0.03	−0.02	−0.2

Table 3.1. Summary of relevant physical characteristics of commercially available permanent magnets.

3.2 Conceptual magnet geometry

The particular constraints imposed by the proposed clinical application of our NMR system required the design the novel magnet geometry capable of generating a large, highly uniform magnetic field oriented horizontal to the surface of the magnet. This geometry allows an RF transceiver coil placed on the surface of the magnet to generate a perpendicular oscillating electromagnetic field. A single sided system was necessary to enable a broad class of measurements on anatomical locations, such as the upper leg, which are unable to fit inside of a small bore NMR scanner. Furthermore, to enable measurement deep into the tissue, the uniform region needed to be exist at a region remote, or at a distance, from the surface of the magnet. The magnet needed to remain portable and therefore a limit to its total magnetic mass was enforced.

It is not straightforward to design a magnet, under these design constraints, capable of generating a very strong, uniform region and there do not exist clear guidelines or methods to guide magnet design.

3.2.1 Prior art in remote, uniform magnetic field geometries

Many previous attempts at creating a remote magnetic field exist in the literature as shown in Figure 3.1. Rectangles represent magnets with inset arrows indicating magnetization direction. Circles represent remote uniform magnetic field position with inset arrows indicating field direction. Unfortunately, these efforts fail to meet the design criteria set forth by this thesis, typically due to limitations in the size, orientation, or uniformity of the field while limiting the mass and volume of the magnet.

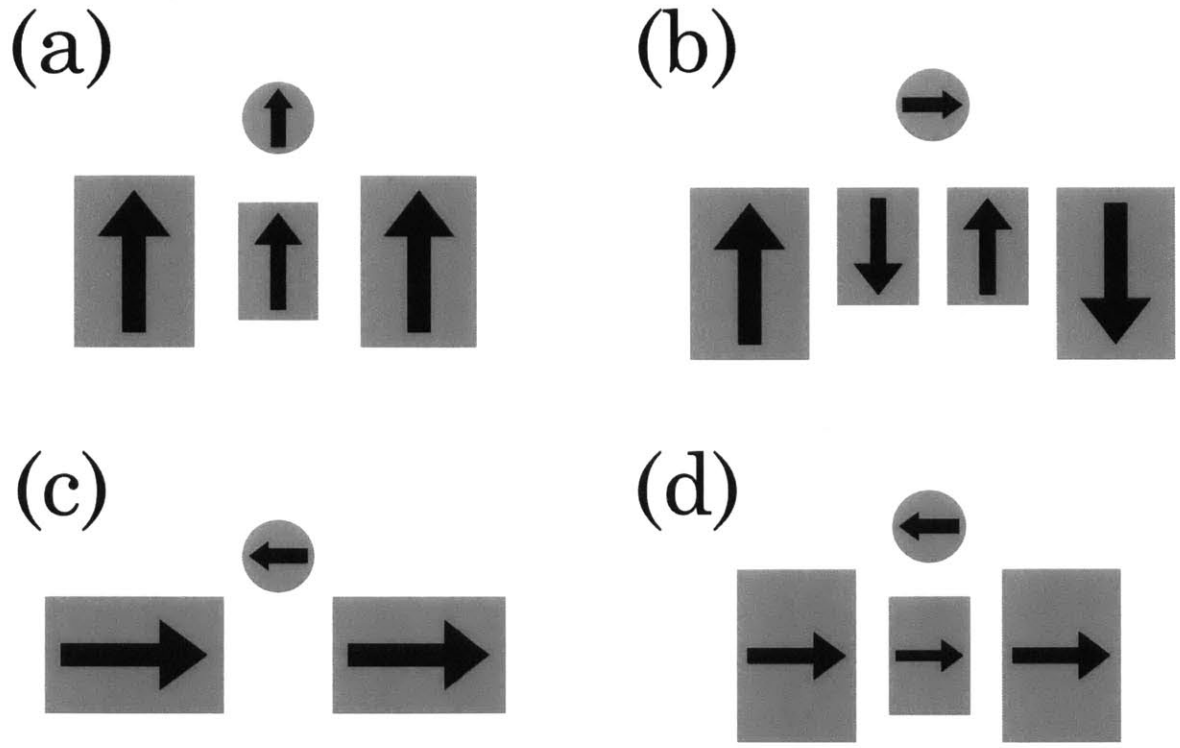

Figure 3.1. Summary of prior art related remote magnetic fields for NMR [87].

3.2.2 Linear Halbach array

A linear Halbach array is capable of producing a magnetic field with its flux concentrated on one side of the magnet assembly with the field at the other side equal to zero. This magnet configuration is produced by rotating the magnetization direction of the magnet in one direction, as shown in Figure 3.2c. In the ideal case, the rotation of the magnetization direction is a continuous function space, given by

$$B_r(x) = B_{r,0}e^{-kx} \tag{3.1}$$

where $B_r(x)$ is the magnetization as a function of space, $B_{r,0}$ is the magnitude of the remanence of magnetization, k is the spatial wavenumber indicating the rate of

rotation of the magnetization, and x is the spatial dimension. The more practical case, shown in Figure 3.2c, consists of a series of discrete magnets which, together, produce a linear Halbach arrangement, the flux on the low side is very low, but not exactly equal to zero [88], [89]. The principle of operation of this magnet, as shown in Figure 3.2, can be thought of as the superposition of two magnet arrangements (a) and (b) such that the field above the magnet is reinforced by each arrangement while the field below the magnet is canceled by the superposition of the two arrangements (c).

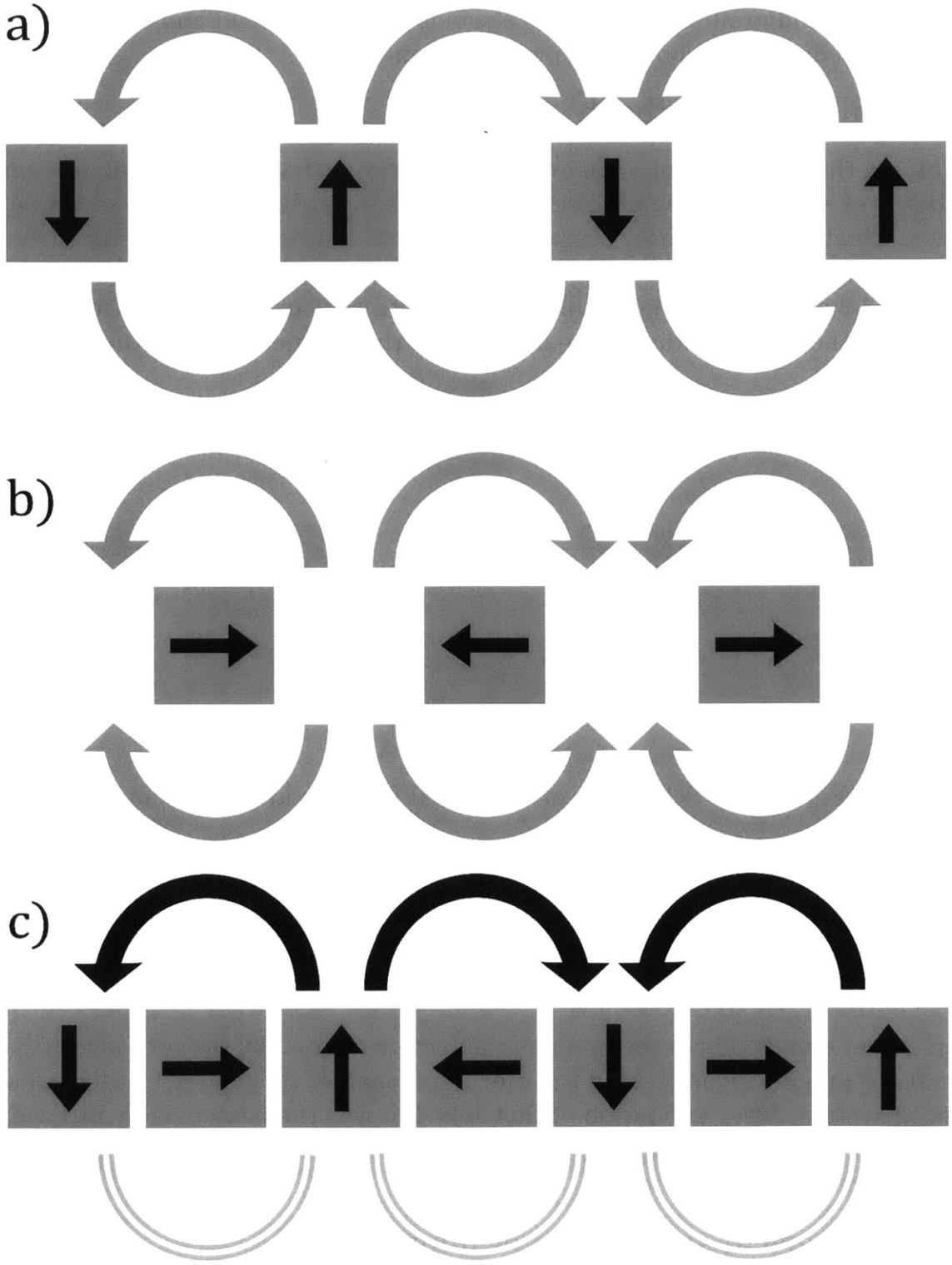

Figure 3.2. Principle of operation of a linear Halbach array.

The concentration of the field strength on one side of the magnet is promising for NMR applications because of the need for a high field strength. Unfortunately,

these systems have yet to find application for NMR measurements because of the relative high field gradient present on the side of the high field and the rapidly rotating field direction along the length of the magnet.

3.2.3 Unilateral Halbach array

Combining the principles of a linear Halbach array with that of a previous attempt by Marble et al., a new magnet geometry – a unilateral Halbach array – can be realized which offers a remote uniform region with improved flux density through the inclusion of linear Halbach elements [87]. A schematic of this geometry is shown in Figure 3.3 where the squares indicate magnets, the circle indicates the uniform region, and the arrows indicate the direction of the magnetic field within either.

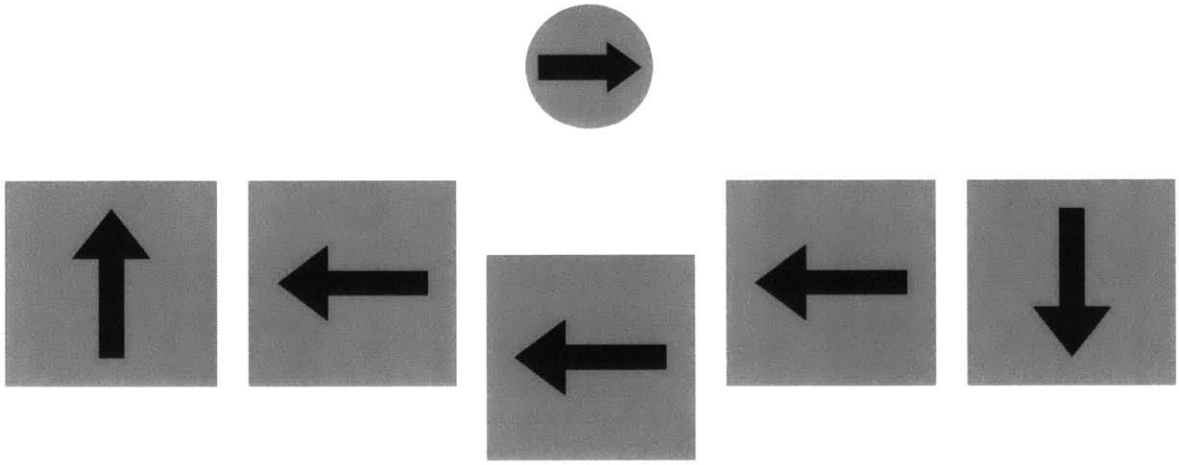

Figure 3.3. Schematic of unilateral Halbach array geometry.

The combination of the Halbach geometry for field concentration and the depressed middle magnet for field uniformity creates a large uniform region with a stronger field strength than typically possible.

3.3 Magnet geometry simulation

A numerical simulation of the magnetic induction created by the presence of permanent magnets was created in order to implement this magnet design in a physical system. After validation of this model, it was then extensively utilized to understand the effect of magnet positioning on the strength and uniformity of the generated remote field.

3.3.1 Numerical simulation of magnet

The orientation and strength of the magnetic field generated by a single magnet is not trivial to express analytically unless considering the field very far from the magnet. The complexity of this problem quickly grows intractable by analytical

approaches when considering the interaction of fields very close to their source. This problem is further complicated by the presence of changes in magnetic permeability at magnet-air interfaces. Therefore, numerical simulations were relied upon to design the magnet assembly.

3.3.1.1 COMSOL simulation

COMSOL Multiphysics 5.2 (Burlington, MA) provided the necessary framework and simulation tools to perform a numerical simulation of the magnetic field produced by the presence of magnets by specifying their remanence (remanent flux density) and magnetic permeability as well as that of the surrounding medium, air. This analysis was performed through finite element analysis on a user-defined mesh on which it solves Gauss' Law for the magnetic field using the magnetic potential. The following outlines the conditions and parameters used for computational modeling within the COMSOL models.

3.3.1.2 Governing equations of simulation

The main constitutive relation set in the model is given by

$$\boldsymbol{B} = \mu_0 \mu_r \boldsymbol{H} + \boldsymbol{B_r} \tag{3.2}$$

where $\boldsymbol{B}$, μ_r, $\boldsymbol{H}$, $\boldsymbol{B_r}$, $\boldsymbol{J}$ are the magnetic induction, relative permeability, magnetic field, remanent flux density, and current density. These equations are converted into second order differential equation with just one field quantity in order to be solved.

The magnetostatic field is governed by Gauss's law, given by

$$\nabla \cdot \boldsymbol{B} = 0 \tag{3.3}$$

and Ampere's law at steady state, given by

$$\nabla \times \boldsymbol{H} = \boldsymbol{J} \tag{3.4}$$

Gauss's law can be satisfied by defined $\boldsymbol{B} = \nabla \times \boldsymbol{A}$, where $\boldsymbol{A}$ is the vector potential and $\nabla \cdot (\nabla \times \mathbf{A}) = 0$. Appropriate substitution of the constitutive relation and the expression for the vector potential into Ampere's law gives a single second order differential equation, given by

$$\nabla \times (\nabla \times \boldsymbol{A} - \boldsymbol{B_r}) = \mu_0 \mu_r \boldsymbol{J} \tag{3.5}$$

The following gauge condition must be enforced to uniquely define $\boldsymbol{A}$:

$$\nabla \cdot \boldsymbol{A} = 0 \tag{3.6}$$

In addition to these field relations, a set of boundary conditions is enforced in the model, given by

$$\boldsymbol{n} \times (\boldsymbol{H}_1 - \boldsymbol{H}_2) = 0 \tag{3.7}$$

and

$$\boldsymbol{n} \cdot (\boldsymbol{J}_1 - \boldsymbol{J}_2) = 0 \tag{3.8}$$

where $\boldsymbol{n}$ is the normal unit vector on the boundary and the subscripts denote fields across a boundary. Finally, magnetic insulation is defined at the edges of the model by enforcing

$$\boldsymbol{n} \times \boldsymbol{A} = 0 \tag{3.9}$$

3.3.1.3 Defining the magnets

A cube with a side length of 12.7 mm was defined for each neodymium magnet. Each magnet was positioned in space independently. All magnets were given a remanent flux density of 1.48 Tesla as this is the theoretical remanence of a N52 neodymium magnet. All magnets were defined with a relative permeability of 1. The entire magnet assembly was surrounded by air, defined as having a relative permeability of 1. This boundary of air was defined as a rectangular prism centered with the center of mass of the magnet and with a size equal to twice that of the magnet assembly in each direction.

3.3.1.4 Domain discretization

Finite element methods are a numerical technique for approximating boundary value problems by simplifying the underlying equations which govern the physics over a finite number of small elements through an interpolation function. Therefore, the equations only have to be solved at the edges of these tetrahedral elements, known as subdomains. Through this, the problem is reformulating as a system of equations. The process of creating a mesh requires foresight into the conditions of the simulation. While a mesh with increased density will improve simulation accuracy, this increase in density necessarily comes with an increase in computational and memory requirements.

The mesh was defined coarsely throughout the entire simulation region except for a small region above the middle of the magnet where the uniform region was located. In this region, known as the region of interest, the mesh was defined much more finely to ensure accuracy and robustness of further computational analysis. The region of interest was typically defined as cube with a 3 cm size length located immediately adjacent to the top of the magnet.

The coarse mesh was defined using the COMSOL predefined mesh setting of 'Fine' which set the following parameters: a maximum element size of 0.0196 m, a minimum element size of 0.00245 m, a maximum element growth rate of 1.45, a curvature factor of 0.5, and a resolution of narrow regions of 0.6. Successively more refined meshes were shown not to appreciably improve the accuracy of the results which suggested that this mesh was suitably dense for these studies.

The denser mesh used for the region of interest in which analysis was performed was defined using the COMSOL predefined mesh setting of 'Extremely Fine' which set the following parameters: a maximum element size of 4.89 mm, a minimum element size of 0.0489 mm, a maximum element growth rate of 1.3, a curvature factor of 0.2, and a resolution of narrow regions of 1. This mesh was shown to be too sparse for accurate computation of properties such as the field gradient and boundaries of the uniform region. Therefore, the maximum element size was further decreased to 0.5 mm.

The magnetic vector field generated by the finite element model only contains values at the nodes defined by the mesh. This makes further computational analysis difficult since this mesh does not define a Cartesian or rectilinear grid. Therefore, the magnetic field is interpolated onto a Cartesian grid with grid spacing of 300 μm which yielded a dataset with 1,000,000 points.

3.3.2 Validation of numerical model

The model was validated with experimental data before performing extensive use. A single 12.7 mm cube, representing a magnet, was created in a large air box. The remanence of the magnet was set to 1.48 Tesla and the magnetic field throughout the entire volume was computed. The field values in a line directly above the magnet were compared with measurements with a gaussmeter (Model 475 DSP Gaussmeter, Lake Shore Cryotronics, Westerville, Ohio). Values at three distances were compared and all of them were within 5% of that of the simulation. The error is attributed to positional error and differences in the remanence between the simulated and measured magnets.

3.3.3 Measuring the performance of a magnetic field

A set of metrics were derived from the magnetic field which defined its geometry and strength in order to compare the fields generated by magnets with different configurations. The uniform region was found by finding the contiguous region, of $B_z(x, y, z)$ defined as the volume $\mathcal{V}$, which maximized an approximation of the signal to noise ratio of a thermal noise limited NMR experiment as calculated by Hoult and Richards [90]. The approximate expression for the signal to noise ratio, assuming a well-designed transceiver coil, is given as

$$SNR \cong \int_{\mathcal{V}} B_z(x,y,z)^{\frac{7}{4}}\, d\mathcal{V} \tag{3.10}$$

The following constraint was enforced to ensure that the uniform region, denoted as $B_z(\mathcal{V})$, was sufficiently uniform:

$$\max\left(B_z(\mathcal{V})\right) - \min\left(B_z(\mathcal{V})\right) \leq \epsilon * B_{z,0} \tag{3.11}$$

where ϵ is the uniformity of the magnetic field.

The following constraint was enforced to ensure that the uniform region was sufficiently uniform in orientation as off axis precession can introduce artifacts into the measurement:

$$\tan^{-1} \sqrt{\frac{B_x(\mathcal{V})^2 + B_y(\mathcal{V})^2}{B_z(\mathcal{V})^2}} \leq 1°, \forall\, \mathcal{V} \tag{3.12}$$

where $B_{z,0}$ is the magnetic field strength of the uniform region and is defined as the mean of the minimum and maximum field strengths within the uniform region.

The following metrics were computed, once the optimal uniform region for a particular magnet geometry was selected, to allow comparison of the field with other fields: magnetic field strength, volume, size in the y direction measured from the center, size in the z direction measured from the center, size in the x direction measured from the center, and distance from the surface of the magnet to the center of the field. An illustration of a subset of these metrics is shown in Figure 3.4.

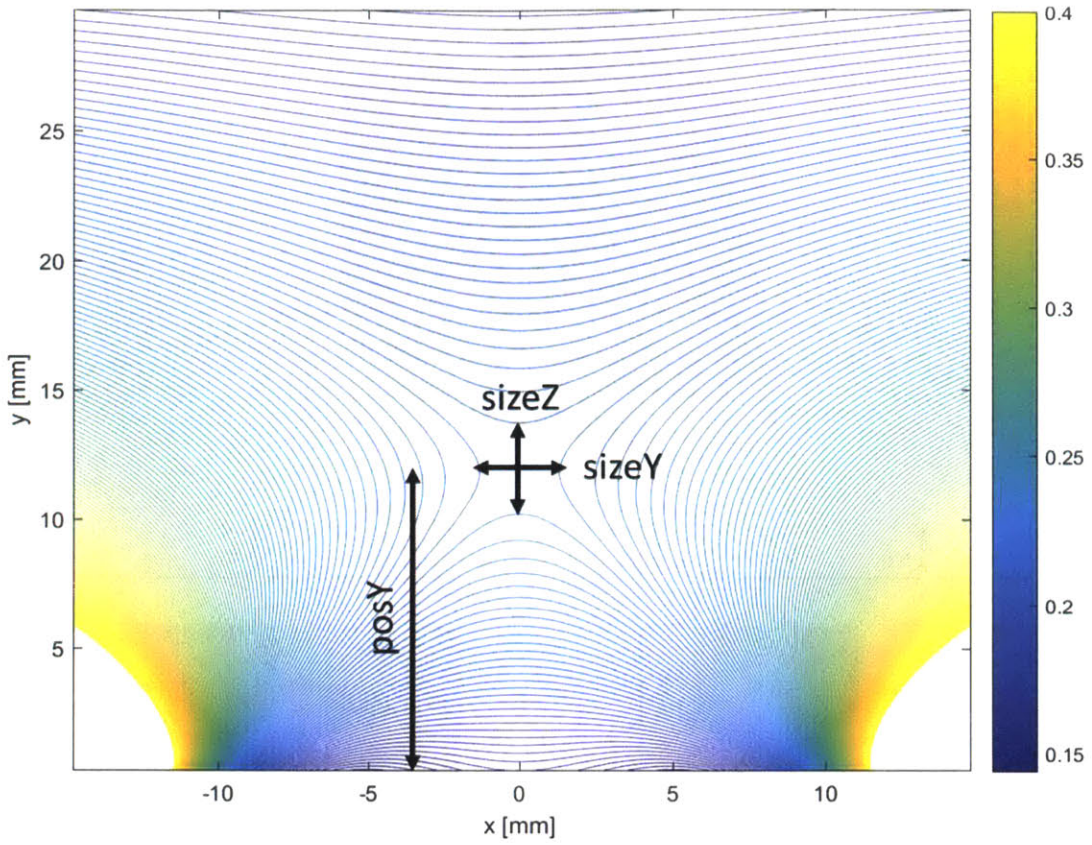

Figure 3.4. Annotated contour plot of magnetic field profile.

3.3.4 Description of magnet geometry

The magnet consists of many identical neodymium cube magnets placed in one of three orientations, up $(+y)$, down $(-y)$, or left $(-z)$ as shown in Figure 3.3. A schematic of the parameters driving the modified linear Halbach array magnet arrangement, based on the concept in Figure 3.3, is shown in Figure 3.5. The magnets are defined based on their side length, relative spacing from each other ($gapX$, $gapY$, $gapZ$), the distance that the middle slice is depressed ($sliceDropY$), and the number of magnets tiled in each direction (Nx, Ny, Nz) as shown in Table 3.2.

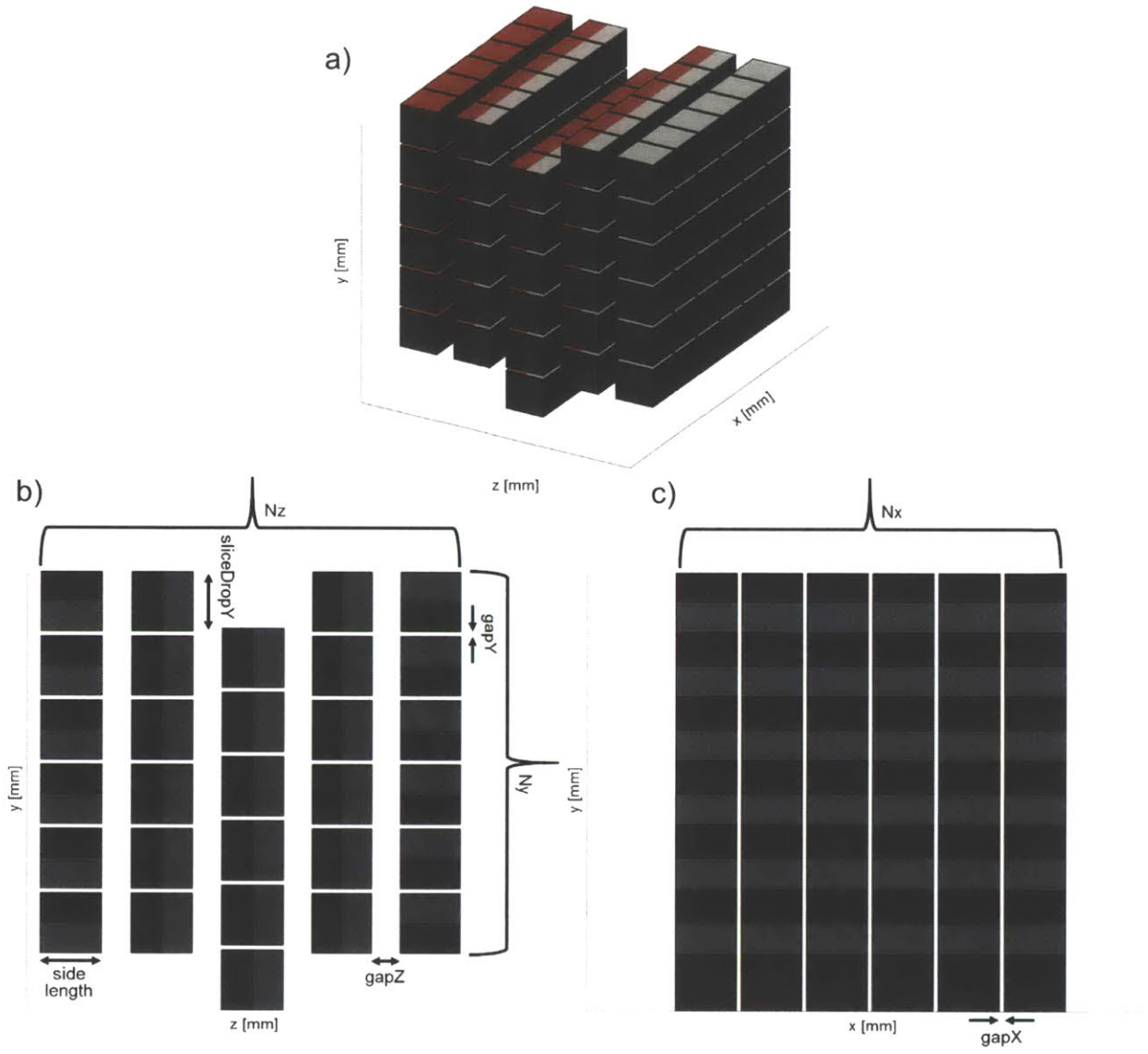

Figure 3.5. Schematic illustration of dimensioned linear Halbach array.

Nx	Number of magnets in x direction
Ny	Number of magnets in y direction
Nz	Number of magnets in z direction
gapX	Air gap between adjacent magnets in x direction, [mm]
gapY	Air gap between adjacent magnets in y direction, [mm]
gapZ	Air gap between adjacent magnets in z direction, [mm]
sliceDropY	Displacement of middle slice in $-y$ direction, [mm]

Table 3.2. Description of magnet dimensions.

Starting with the magnet geometry shown in Table 3.3 and illustrated in Figure 3.5, each parameter was varied, each individually and some in conjunction with others, and the effect of these changes on the performance of the magnet measured. An understanding of the effect of varying each parameter was used to inform development of a magnet geometry that met the design specifications.

Magnet side length	12.7 mm
Nx	6
gapX	1 mm
Ny	6
gapY	1 mm
Nz	5
gapZ	6 mm
sliceDropY	12 mm

Table 3.3. Initial magnet geometry.

3.3.5 Exploration of design space

3.3.5.1 Varying Nz

The first parameter that was explored was the number of magnets in the z direction, known as Nz. The number of magnets in the z direction was set to 5, 7, and 9 in order to preserve symmetry. Only the slices on the extreme z positions were positioned vertically while the rest were horizontal. Only the middle slice was depressed. Illustrations of the three magnet configurations are shown in Figure 3.6.

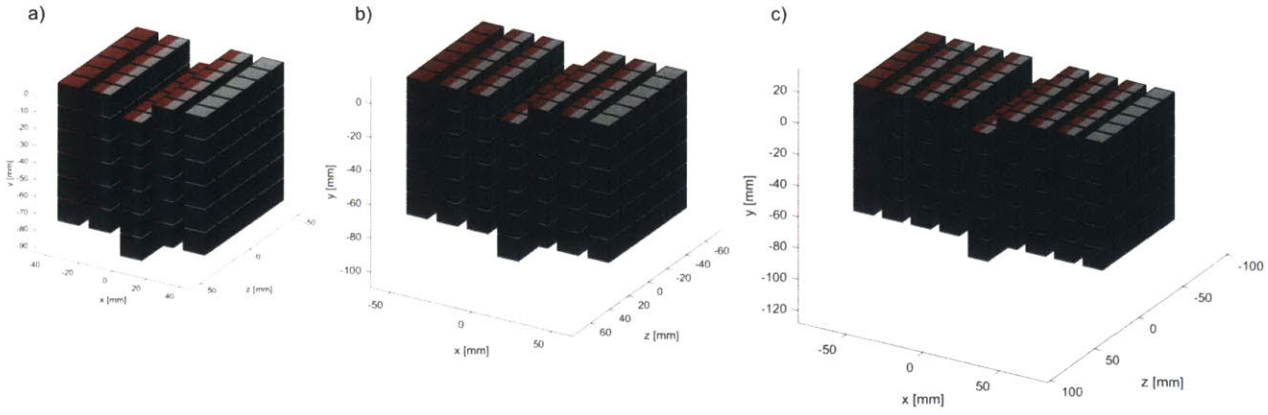

Figure 3.6. Illustration of magnet arrangements for each magnet configuration as Nz was varied.

It was expected that the uniform region would move further from the surface of the magnet as the size of the magnet increased.

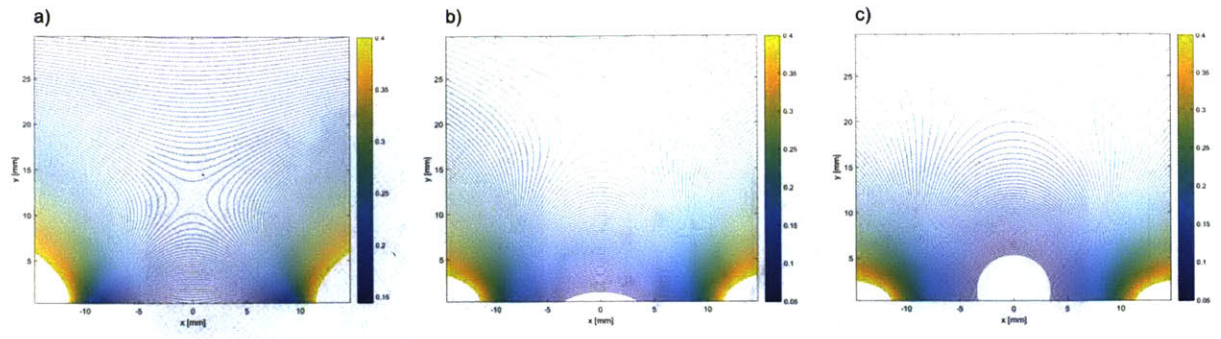

Figure 3.7. Contour plots of field for each magnet configuration as Nz was varied.

Nz	5	7	9
Magnetic field strength [Tesla]	0.21	0.16	0.15
Depth [mm]	11.7	19.5	26.7
Size, x [mm]	11.4	16.2	27.0
Size, y [mm]	3.6	5.1	6.0
Size, z [mm]	1.8	3.0	4.2

Table 3.4. Magnetic field metrics for each magnet configuration as Nz was varied.

Numerical models of magnets with a varied number of slices in the *z* direction indicate that an increased number of slices rapidly increases the size and depth of the uniform region while decreasing the strength of the magnetic field as shown by Figure 3.7 and Table 3.4. It is evident that the shape of the uniform region changes as Nz is varied therefore further considerations beyond simply the well-defined metrics shown in Table 3.4.

3.3.5.2 Varying Nx

The number of magnets in the *x* direction, Nx, was varied sequentially from 5 to 8 while holding all other dimensions constant. Illustrations of these magnet arrangements are shown in Figure 3.8.

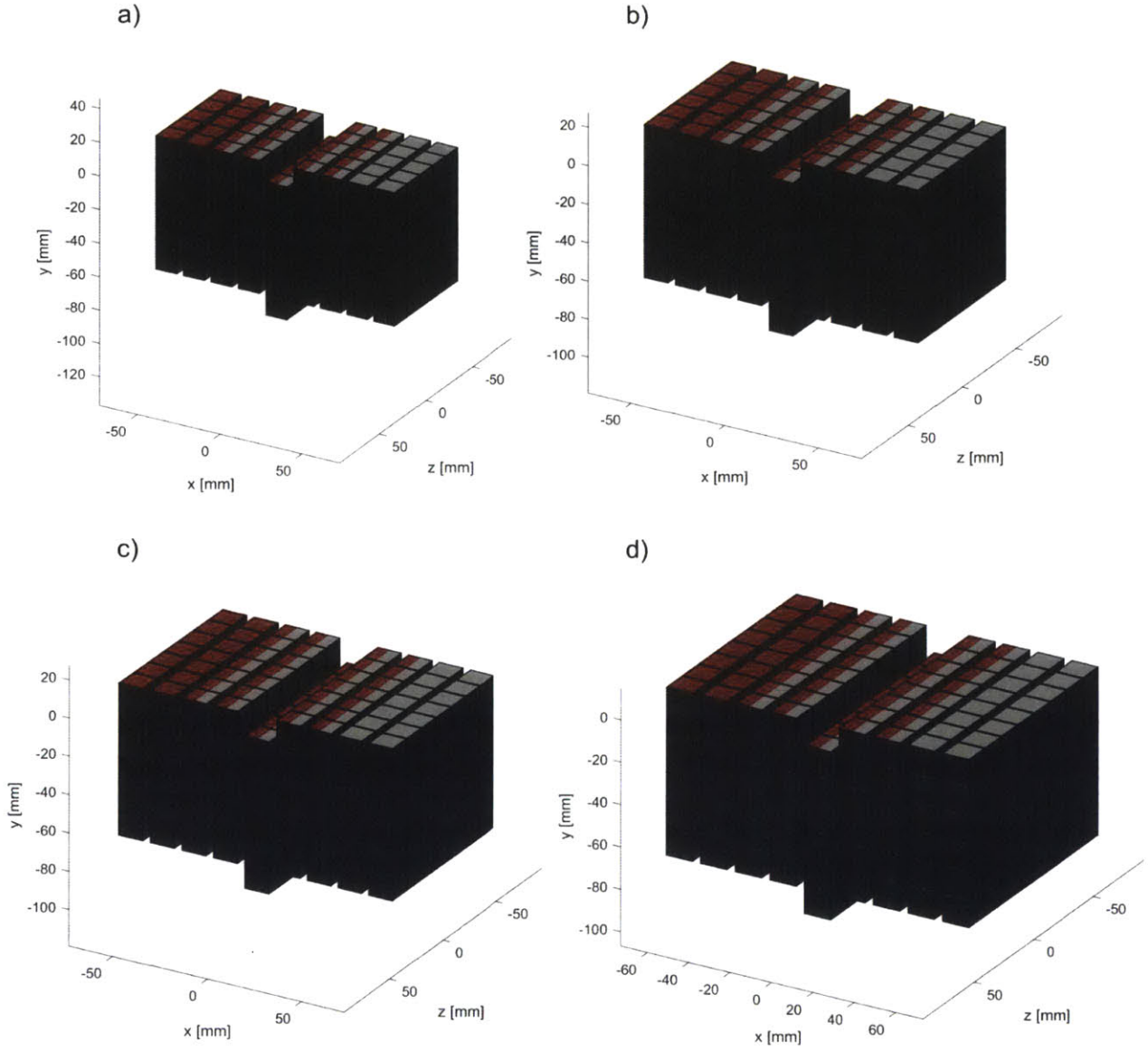

Figure 3.8. Illustration of magnet arrangements for each magnet configuration as Nx was varied.

It was expected that the magnetic field strength would increase, the size in the x direction of the uniform region would increase, and all other metrics would remain unchanged.

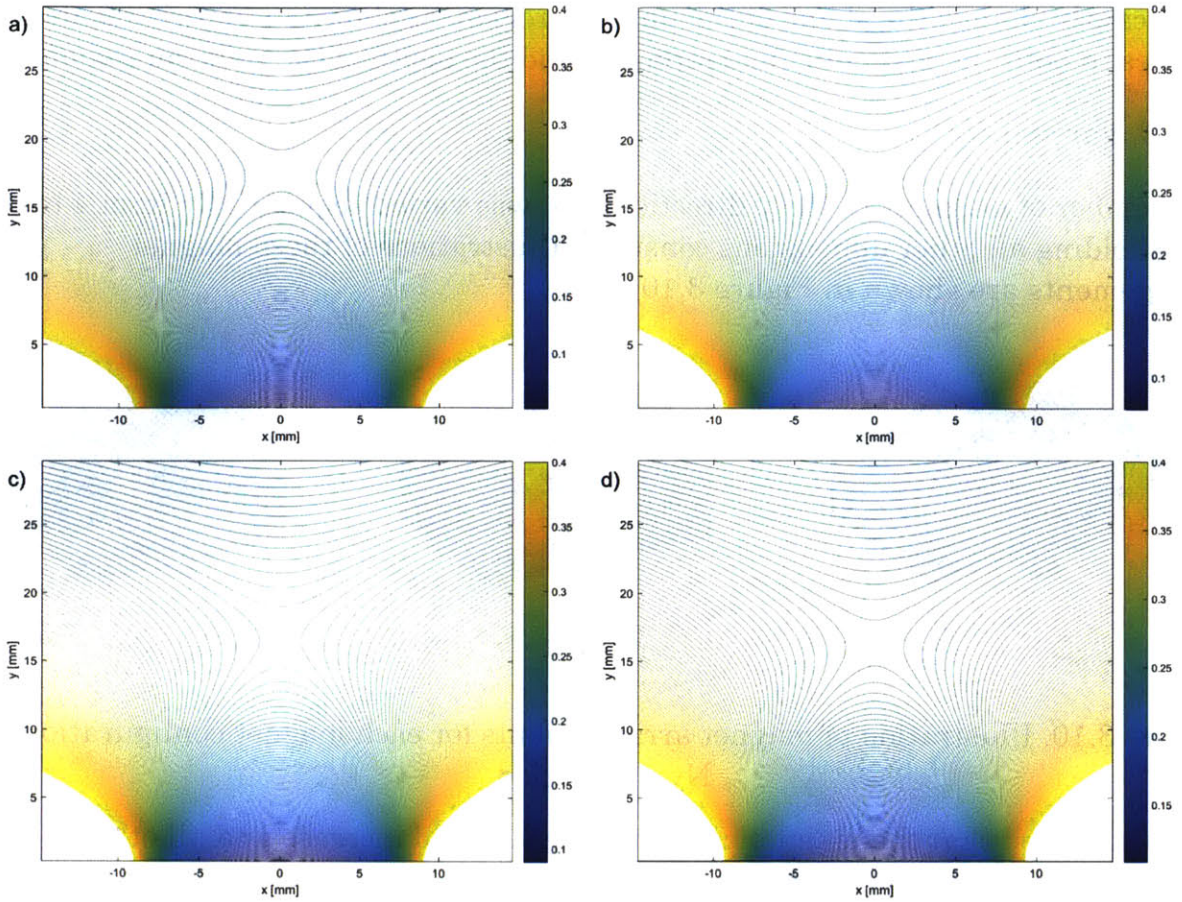

Figure 3.9. Contour plots of field for each magnet configuration as Nx was varied.

Nx	5	6	7	8
Magnetic field strength [Tesla]	0.2141	0.2286	0.2429	0.2563
Depth [mm]	17.4	16.8	16.35	15.9
Size, x [mm]	14.4	14.4	15.0	16.2
Size, y [mm]	4.8	4.8	4.7	4.7
Size, z [mm]	3.0	3.0	3.0	3.0

Table 3.5. Magnetic field metrics for each magnet configuration as Nx was varied.

Numerical models of magnets with a varied number of slices in the x direction indicated that an increased number of slices increases the magnetic field strength and size in the x direction significantly while slightly decreasing the depth of the uniform region as shown by Figure 3.9 and Table 3.5. Varying Nx did not

significantly change the shape of the uniform region, as shown in Figure 3.9, despite changes in both the magnetic field strength and the depth of the uniform region.

3.3.5.3 Varying Ny

The number of magnets in the *y* direction, Ny, was varied sequentially from 4 to 6 while holding all other dimensions constant. Illustrations of these magnet arrangements are shown in Figure 3.10.

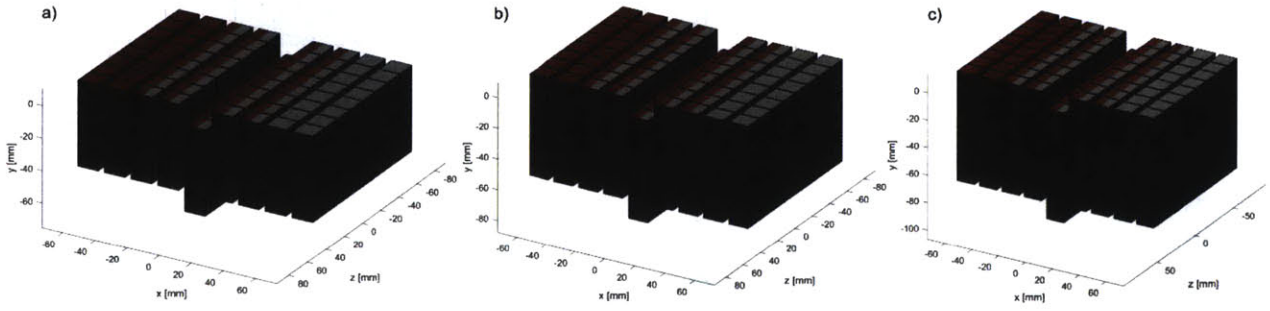

Figure 3.10. Illustration of magnet arrangements for each magnet configuration as Ny was varied.

It was expected that the magnetic field strength would increase and all other metrics would remain unchanged.

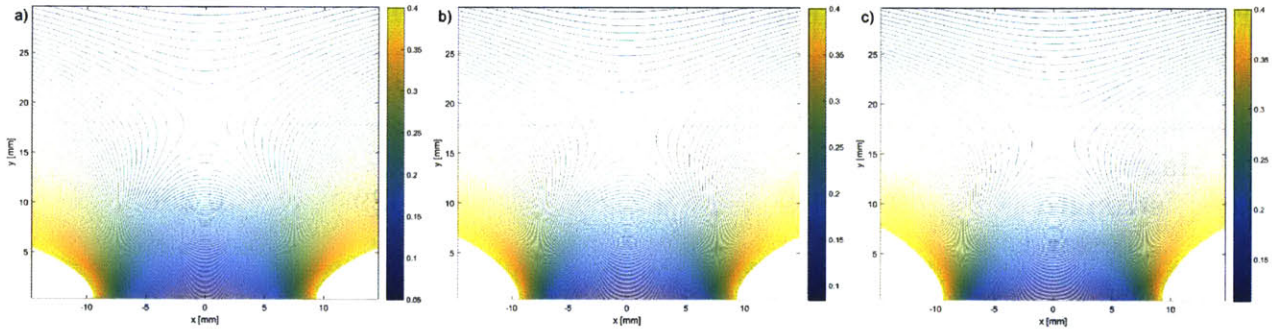

Figure 3.11. Contour plots of field for each magnet configuration as Ny was varied.

Ny	4	5	6
Magnetic field strength [Tesla]	0.217	0.240	0.256
Depth [mm]	17.7	16.5	15.9
Size, x [mm]	16.1	16.1	16.1
Size, y [mm]	4.9	4.8	4.7
Size, z [mm]	3.0	3.0	3.0

Table 3.6. Magnetic field metrics for each magnet configuration as Ny was varied.

Numerical models of magnets with a varied number of slices in the *y* direction indicated that an increased number of slices increases the magnetic field strength while decreasing the depth. A minor decrease in size in the *y* direction was also observed as shown by Figure 3.11 and Table 3.6. Varying Ny did not significantly change the shape of the uniform region, as shown in Figure 3.11, despite changes in both the magnetic field strength and the depth of the uniform region.

3.3.5.4 Varying gapX

The gap between the magnets in the *x* direction, gapX, was varied from 0.6 to 2 mm in increments of 0.1 mm while holding all other dimensions constant. Illustrations of a subset of these magnet arrangements are shown in Figure 3.12

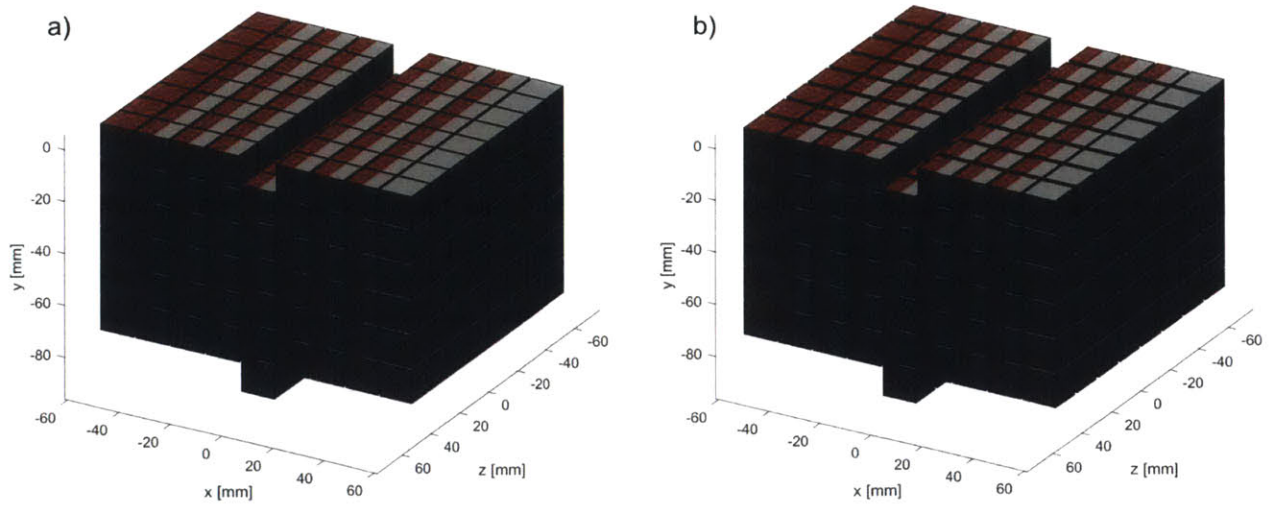

Figure 3.12. Illustration of magnet arrangements as gapX was varied.

It was expected that, as gapX was increased, the magnetic field strength would decrease and the depth would increase.

gapX	0.6 mm	1.3 mm	2.0 mm
Magnetic field strength [Tesla]	0.259	0.252	0.245
Depth [mm]	16.4	16.4	16.2
Size, x [mm]	16.8	17.1	17.4
Size, y [mm]	4.8	4.8	4.7
Size, z [mm]	3.0	3.0	3.0

Table 3.7. Magnetic field metrics as gapX was varied.

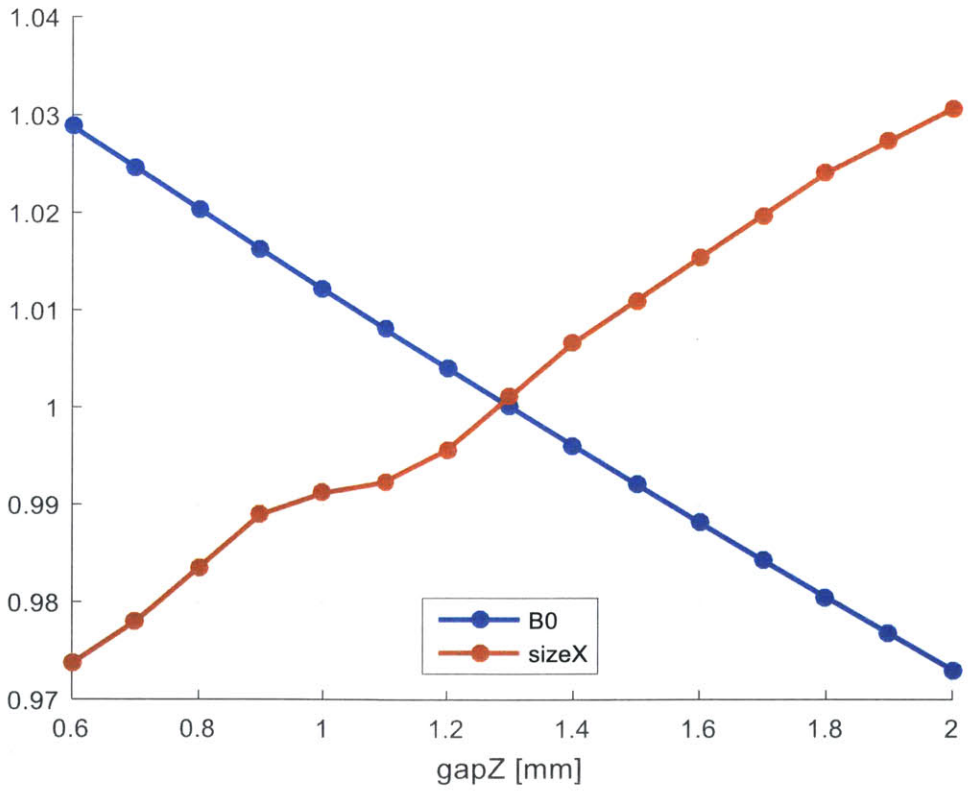

Figure 3.13. Normalized magnet metrics versus gapX.

Numerical models of magnets with a varied gapX indicated that an increased gapX led to a decreased field strength and increase size of the uniform region in the x

direction while all other metrics were relatively unchanged as shown in Table 3.9 and Figure 3.13.

3.3.5.5 Varying gapY

The gap between the magnets in the *y* direction, gapY, was varied from 0 to 4 mm in increments of 0.5 mm while holding all other dimensions constant. Illustrations of a subset of these magnet arrangements are shown in Figure 3.14 where a) indicates a magnet with a gapY of 0 mm and b) indicates a magnet with a gapY of 4 mm.

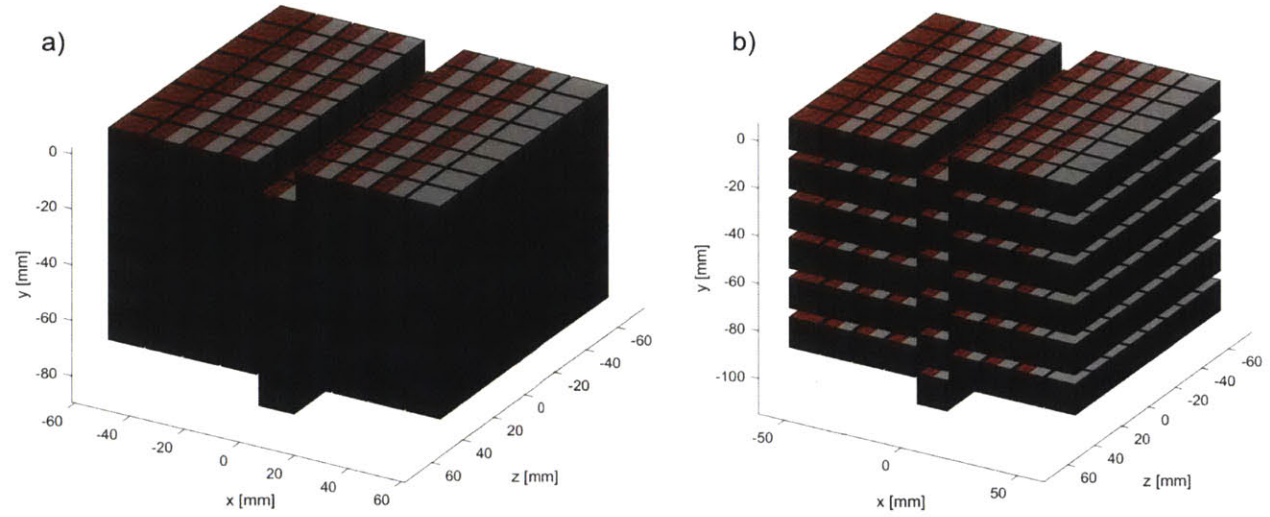

Figure 3.14. Illustration of magnet arrangements with varied gapY.

It was expected that, as gapY was increased, the magnetic field strength would decrease.

gapY	0 mm	2 mm	4 mm
Magnetic field strength [Tesla]	0.262	0.240	0.220
Depth [mm]	16.4	16.6	16.8
Size, x [mm]	16.8	17.1	17.1
Size, y [mm]	4.7	4.7	4.7
Size, z [mm]	3.0	3.0	3.0

Table 3.8. Magnetic field metrics as gapY was varied.

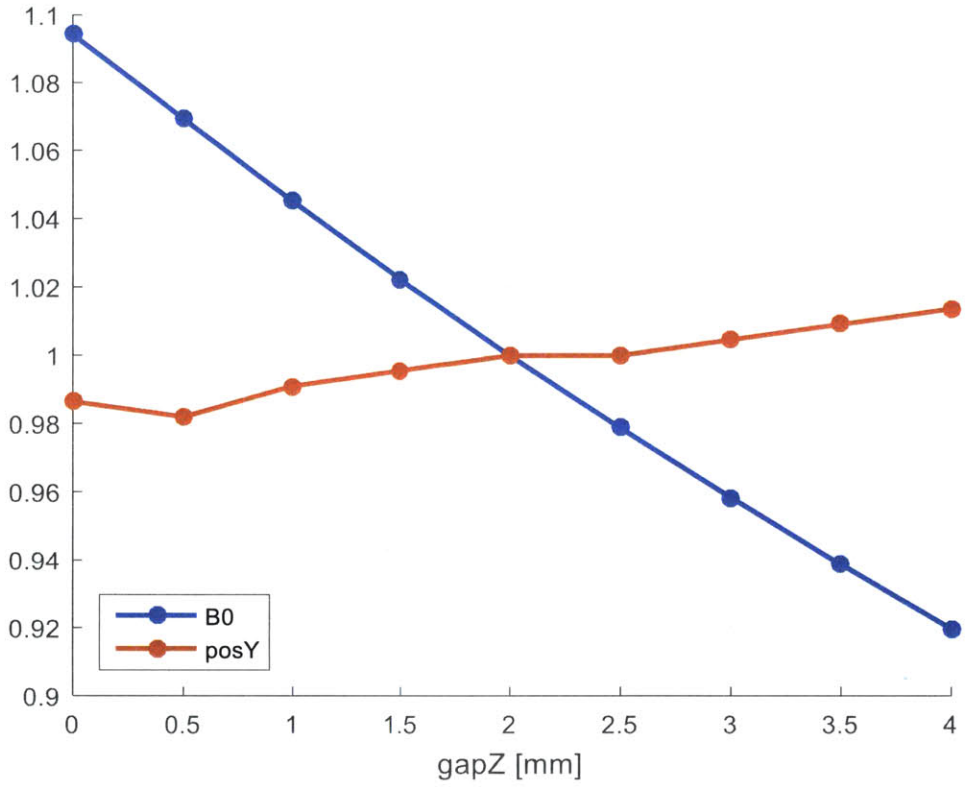

Figure 3.15. Normalized magnet metrics versus gapY.

Numerical models of magnets with a varied gapY indicated that an increased gapY led to a decreased field strength and slight increase in depth of the uniform region while all other metrics were relatively unchanged as shown in Table 3.8 and Figure 3.15.

3.3.5.6 Varying gapZ

The gap between the magnets in the *z* direction, gapZ, was varied from 0.6 to 1.2 mm in increments of 0.1 mm while holding all other dimensions constant. Illustrations of a subset of these magnet arrangements are shown in Figure 3.16 where a) indicates a magnet with a gapZ of 0.6 mm and b) indicates a magnet with a gapZ of 1.2 mm.

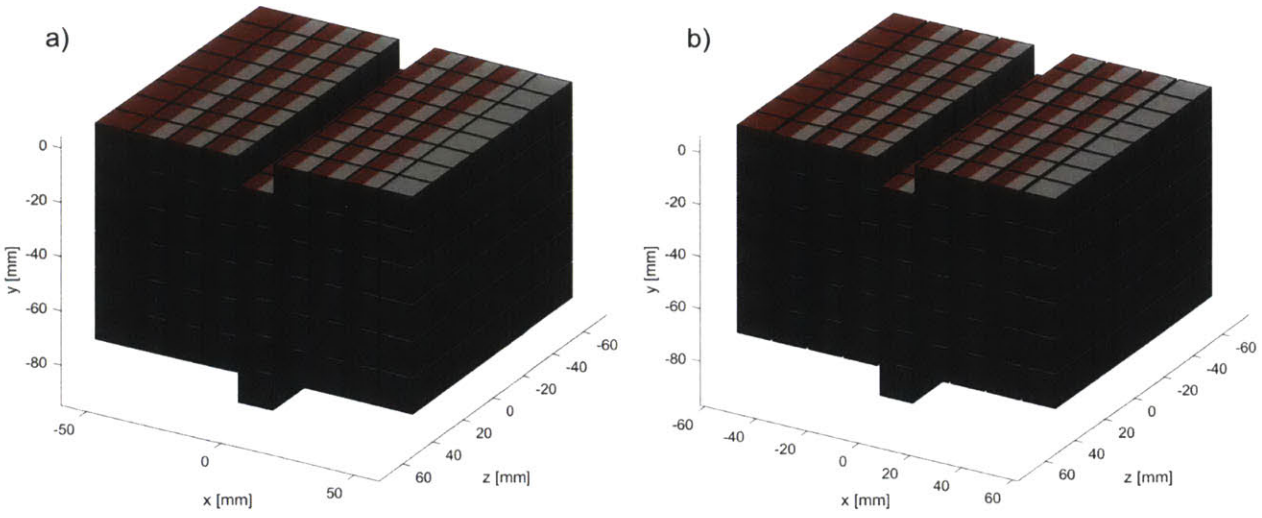

Figure 3.16. Illustration of magnet arrangements with varied gapZ.

It was expected that, as gapZ was increased, the magnetic field strength would decrease and the depth would increase.

gapZ	**0.6 mm**	**0.9 mm**	**1.2 mm**
Magnetic field strength [Tesla]	0.270	0.261	0.253
Depth [mm]	15.8	16.3	16.8
Size, x [mm]	16.4	16.7	16.8
Size, y [mm]	4.6	4.7	4.9
Size, z [mm]	3.0	3.0	3.0

Table 3.9. Magnetic field metrics as gapZ was varied.

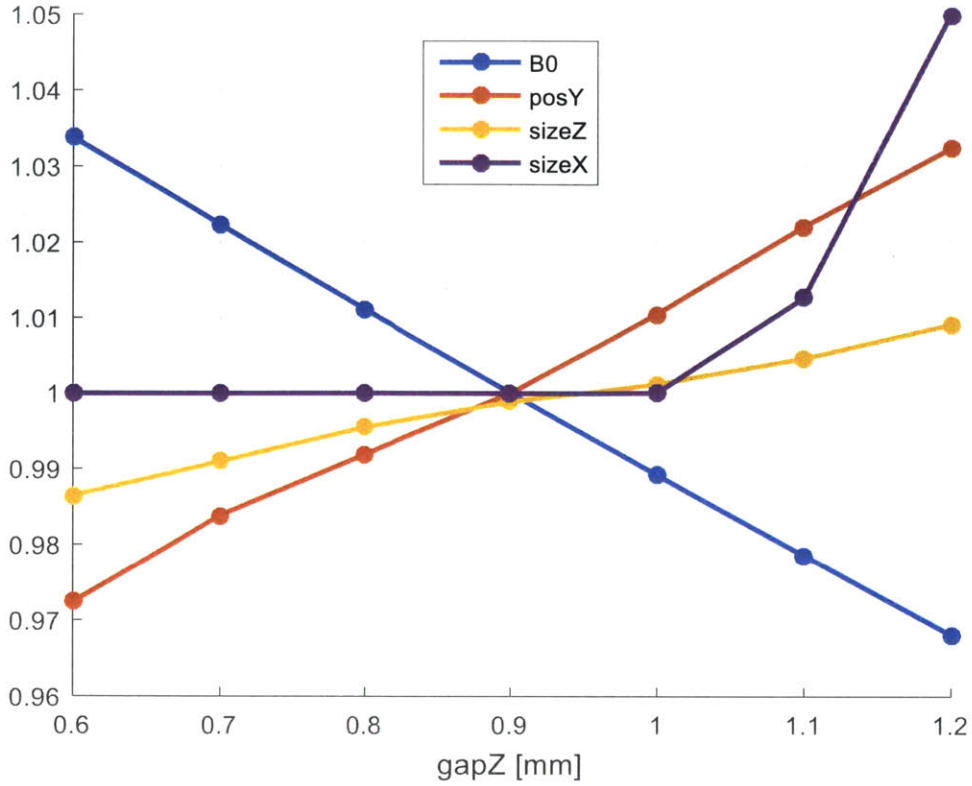

Figure 3.17. Normalized magnet metrics versus gapZ.

Numerical models of magnets with a varied gapZ indicated that an increased gapZ led to a decreased field strength, increased depth, increased size in y direction, and increased size in the x direction while all other metrics were relatively unchanged as shown in Table 3.9 and Figure 3.17.Figure 3.7

3.3.5.7 Varying sliceDropY

The displacement of the middle slice in the $-y$ direction, sliceDropY, was varied from 0 to 15 mm in increments of 0.2 mm holding all other dimensions constant. Illustrations of a subset of these magnet arrangements are shown in Figure 3.18 where a) indicates a magnet with a sliceDropY of 0 mm, b) indicates a magnet with a sliceDropY of 7.6 mm, and c) indicates a magnet with a sliceDropY of 15 mm.

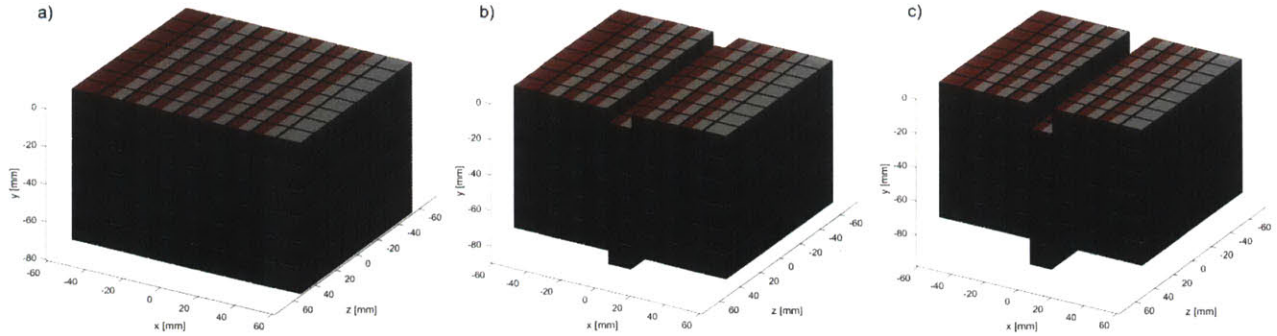

Figure 3.18. Illustration of magnet arrangements with varied sliceDropY.

It was expected that, as sliceDropY was varied, an optimal placement of the middle slice would be found that created a uniform region with both a strong field strength and a large depth.

sliceDropY	**1 mm**	**8 mm**	**15 mm**
Magnetic field strength [Tesla]	0.3467	0.271	0.246
Depth [mm]	6.3	15.2	17.7
Size, x [mm]	13.5	16.5	16.8
Size, y [mm]	1.2	4.7	4.8
Size, z [mm]	6.9	3.0	3.0

Table 3.10. Magnetic field metrics as sliceDropY was varied.

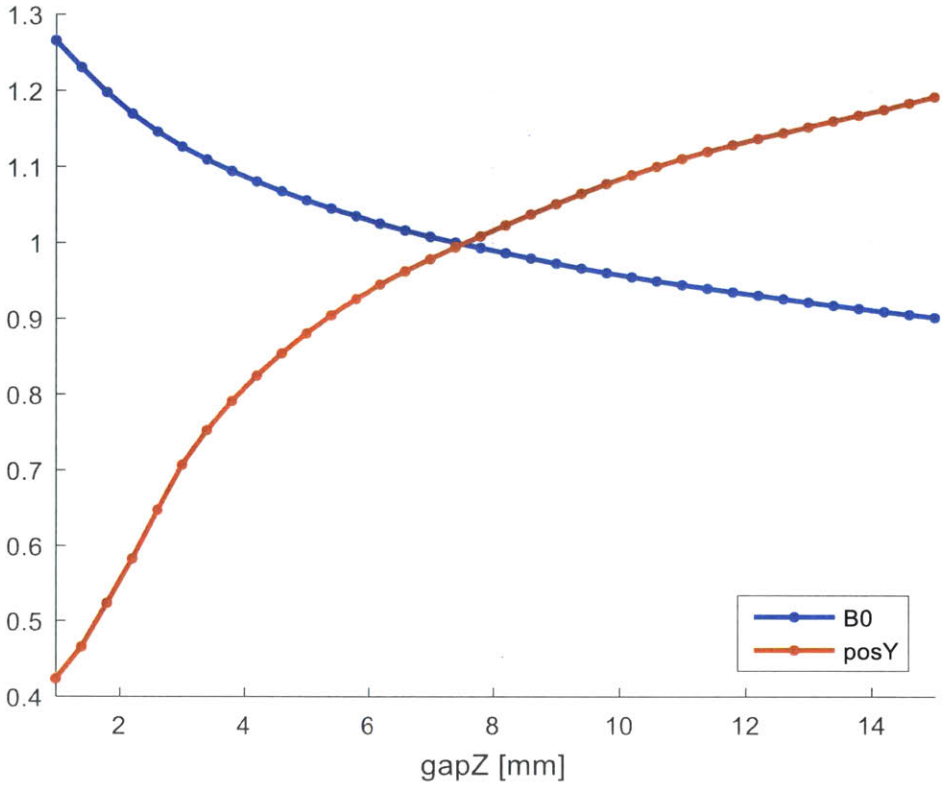

Figure 3.19. Normalized magnet metrics versus sliceDropY.

Numerical models of magnets with a varied sliceDropY indicated that when sliceDropY is below 1 mm, there is no uniform region created in the region directly above the magnet. Therefore, only values of sliceDropY equal to or greater than 1 mm were considered. An increased sliceDropY led to a deeper uniform region with a more isotropic shape and decreased field strength as shown in Table 3.10 and Figure 3.19. Normalized magnet metrics versus sliceDropY.. The rate of decrease in the magnetic field strength and the rate of increase in the depth of the uniform region both decreased with increased sliceDropY. All other metrics were relatively unchanged except at very small sliceDropY values where both sizeX and sizeZ took on extreme values due to the highly irregular shape of the uniform region.

3.3.5.8 Varying both gapZ and sliceDropY

Some parameters were varied in conjunction due to the highly linked nature of these parameters on the performance of the magnet. The gap between the magnets in the z direction, gapZ, and the displacement of the middle slice in the $-y$ direction, sliceDropY, were both varied and the performance of the magnet characterized through numerical simulation. gapZ was varied from 4 to 12 mm in increments of 1 mm. sliceDropY was varied from 6 to 15 mm in increments of 3 mm. Representative

illustrations indicating the extreme values of each parameter are shown in Figure 3.20 where gapZ and sliceDropY are equal to 4 mm and 6 mm in a), 4 mm and 15 mm in b), 12 mm and 6 mm in c), and 12 mm and 15 mm in d).

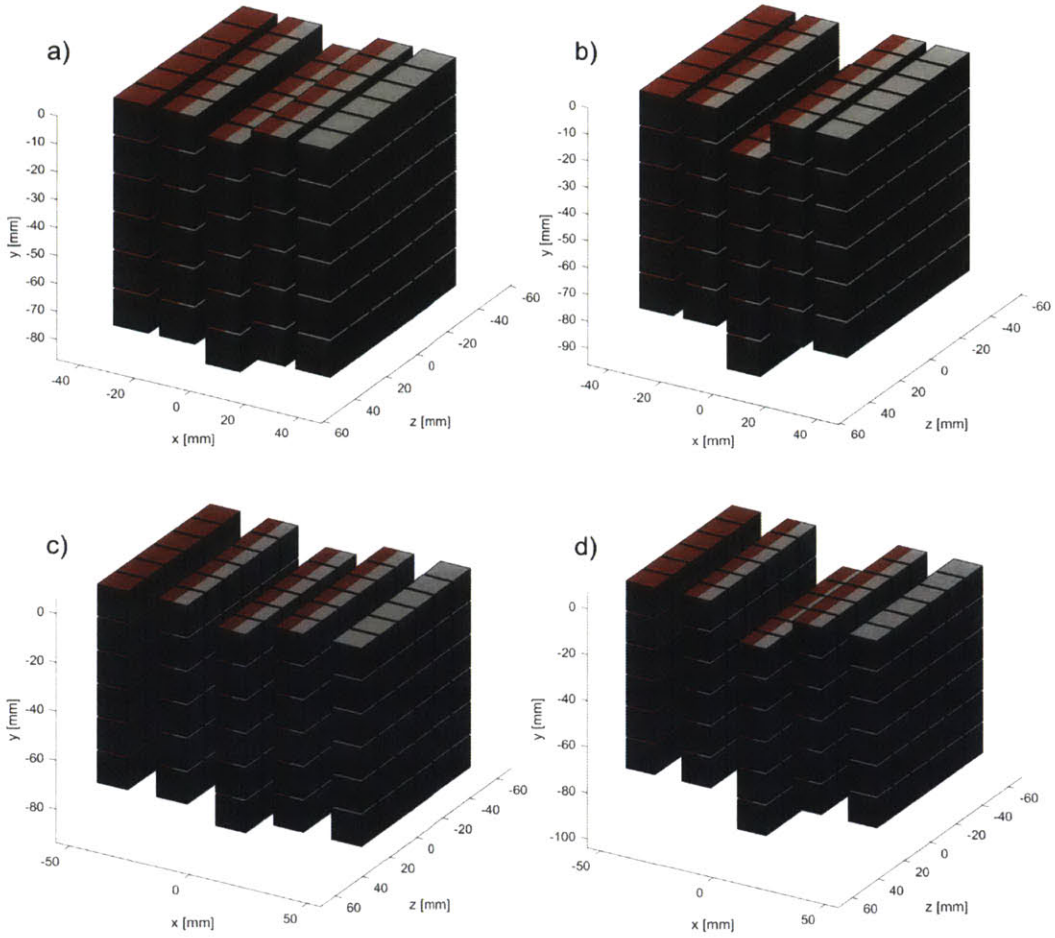

Figure 3.20. Illustration of magnet arrangements with varied gapZ and sliceDropY.

It was expected that there would be a complementary effect from increased sliceDropY and gapZ which would lead to a decreased field strength and increased depth of the uniform region.

gapZ	**4 mm**	**8 mm**	**12 mm**
sliceDropY	**6 mm**	**12 mm**	**15 mm**
Magnetic field strength [Tesla]	0.287	0.179	0.132
Depth [mm]	5.6	12.9	17.4
Size, x [mm]	9.9	12.2	14.0
Size, y [mm]	6.0	4.2	5.1
Size, z [mm]	3.6	2.4	3.0

Table 3.11. Magnetic field metrics as gapZ and sliceDropY were varied together.

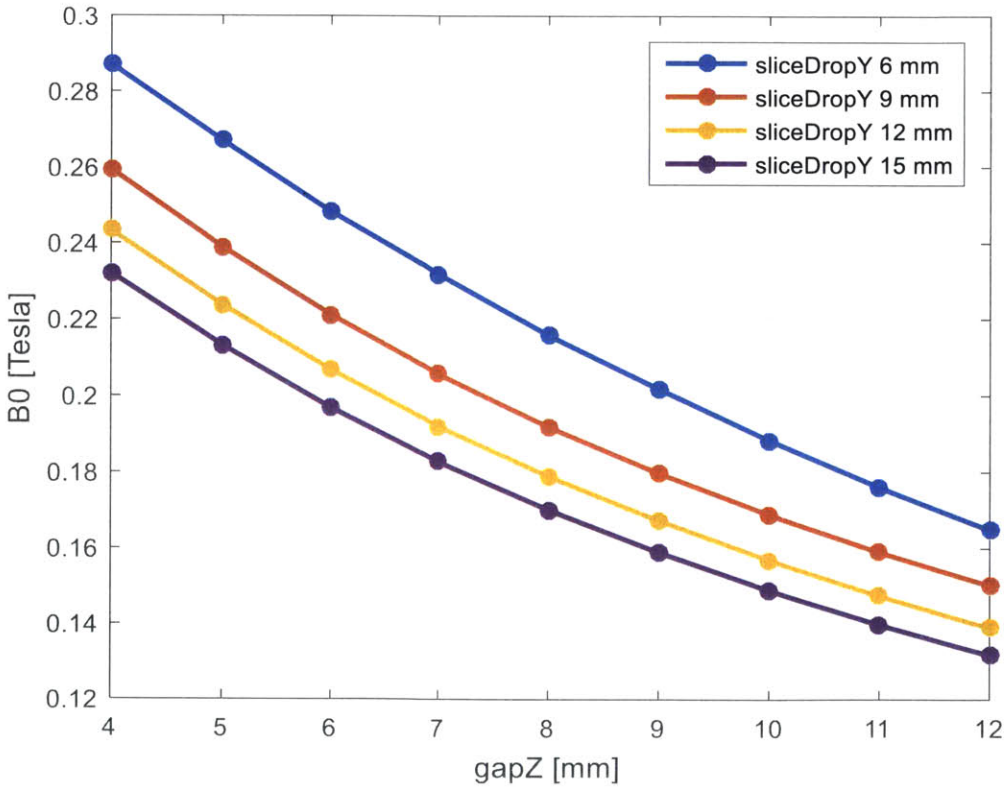

Figure 3.21. Magnetic field strength versus gapZ for different sliceDropY values.

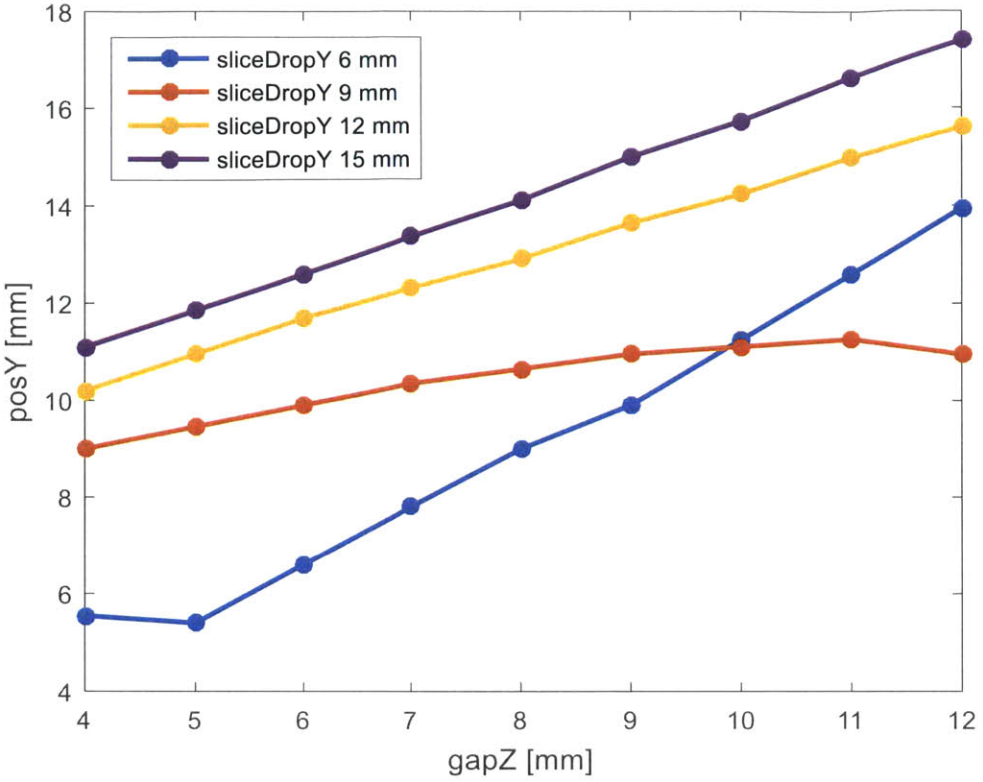

Figure 3.22. Depth versus gapZ for different sliceDropY values.

Numerical models of magnets with varied gapZ and sliceDropY indicated that the effects previously seen when each parameter was varied independently are still present as shown in Table 3.11, Figure 3.21, and Figure 3.22. Furthermore, it was observed that a uniform region directly above the magnet was only produced when the ratio of gapZ to sliceDropY remained within a particular range. When either sliceDropY was very small or gapZ was very large, the uniform region was not well defined directly above the middle of the magnet.

3.3.5.9 Summary of design space exploration

The results of this exploration of the design space indicated with parameters can be tuned to produce stronger, deeper, and larger uniform magnet fields, as shown in Table 3.12.

	Field strength	Depth	Size, *x*	Size, *y*	Size, *z*
Nz	+	+	+	+	+
Nx	+	−	+		
Ny	+	−			
gapX	−		+		
gapY	−	+			
gapZ	−	+	+	+	
sliceDropY	−	+	+	+	

Table 3.12. Summary of findings from design space exploration.

3.3.6 Final magnet design

These findings were utilized to design an optimal magnet assembly for measurement of chemical status within tissue for oxygen, pH, and hydration applications. The main functional requirements of the magnet required that the uniform field magnetize a sufficient volume of tissue at a useful depth at a high enough field to produce a signal sensitivity measurement.

A field strength of approximately 0.2 Tesla was considered sufficient as that was similar to that of previous work in single sided NMR for research purposes [82], [87]. The volume of the magnetic field was maximized with a nominal goal of magnetizing 1 cm^3 of tissue. A depth of at least 15 mm was sought in order to ensure measurement beyond the dermis and subcutaneous layers [91]. The ratio of size of the uniform field in the *y* and *z* direction was desired to be close to unity in order for location of the magnetized tissue to be more easily characterized. A volume of roughly 1 cm^3 was sought for the uniform region when defined as having a field deviation of 1% from its center. The volume of the magnet was limited to approximately 1000 cm^3 to ensure portability as this magnet would weigh less than 9 kg. Minimum values for gapX, gapY, and gapZ were set based on manufacturing capabilities.

The gap between the magnets was minimized as the increase in field strength from this minimization was more valuable than the minor loss in size and depth of field. The number of magnets in the *y* and *z* direction were maximized without exceeding the maximum allowed size of the magnet. Then the optimal Nx and sliceDropY for the given magnet were selected.

Magnet side length	12.7 mm
Nx	8
gapX	2.22 mm
Ny	6
gapY	0.64 mm
Nz	9
gapZ	1 mm
sliceDropY	11 mm

Table 3.13. Final magnet dimensions.

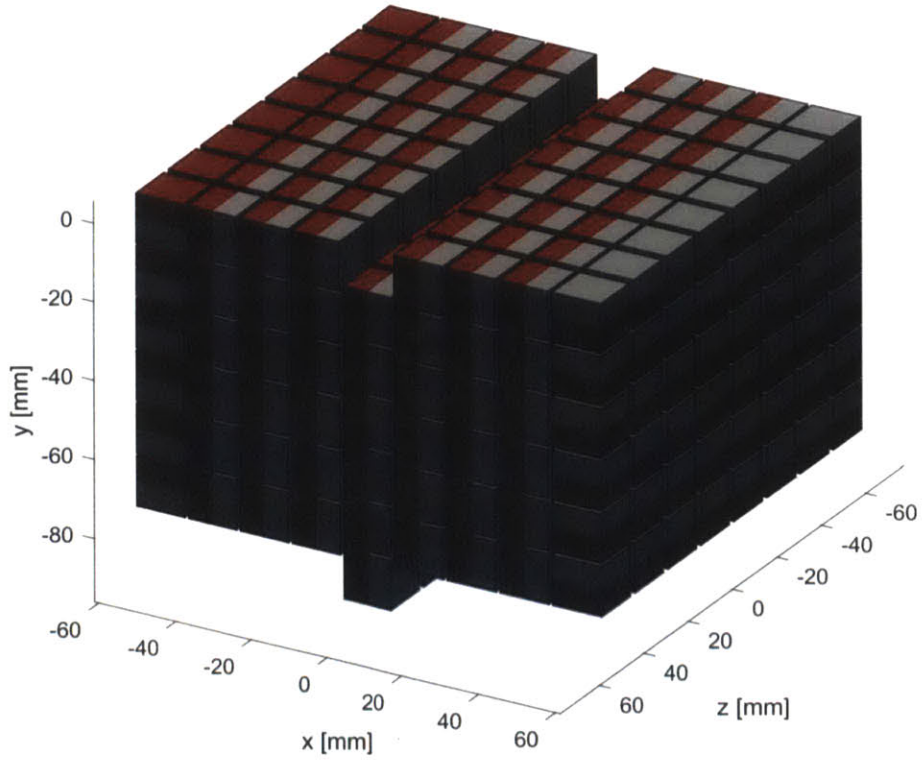

Figure 3.23. Illustration of final magnet design.

Field strength	0.243 Tesla
Depth	16.2 mm
Size, x	17.8 mm
Size, y	4.8 mm
Size, z	3.0 mm

Table 3.14. Magnetic field metrics of final magnet design.

The dimensions of the final magnet design are shown in Table 3.13 and an illustration of this magnet is shown in Figure 3.23. The simulated performance of the uniform region generated by the magnet is shown in Table 3.14. The field strength predicted by the simulation and depth were in excess of that required by the stated functional requirements.

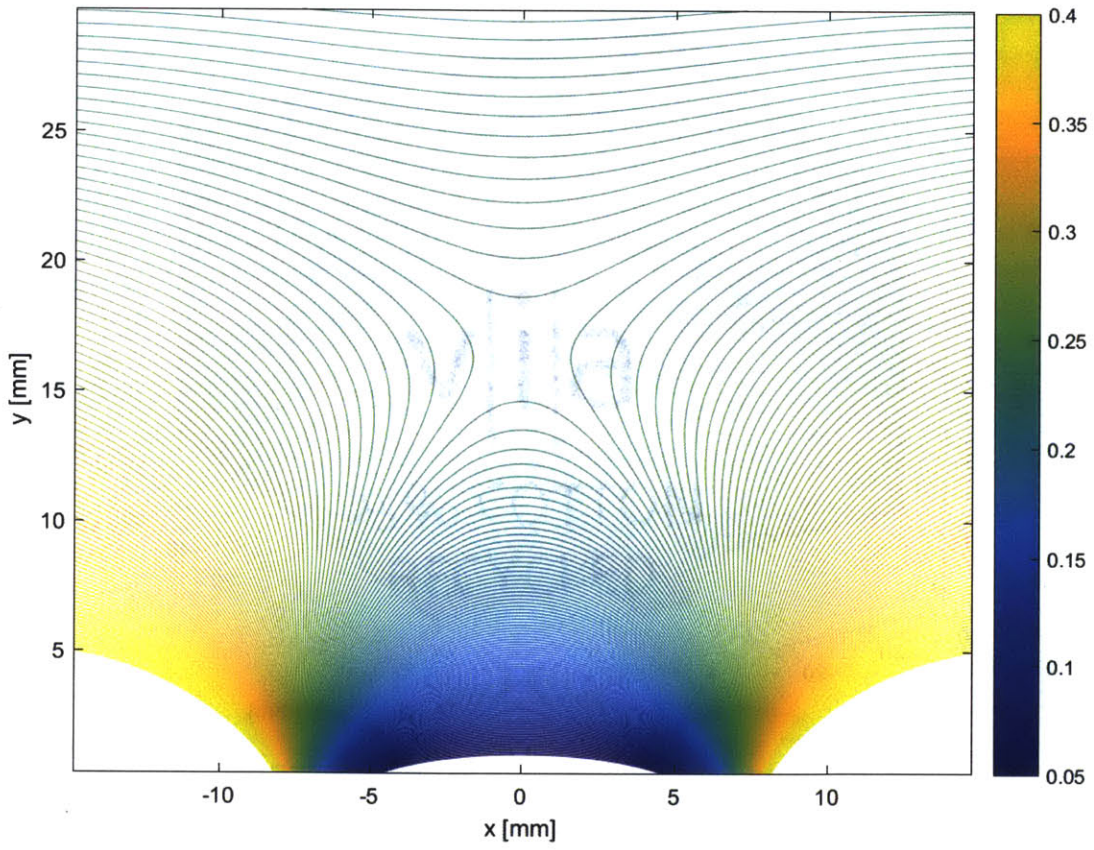

Figure 3.24. Field profile directly above the center of the final magnet design.

3.4 Magnet temperature

Neodymium magnets have a non-zero temperature coefficient of remanence as previously mentioned. This means that the remanence, and thus the external field strength, is a function of temperature. While we do not expect our sensor to be used in extremely high or low temperature environments which could permanently damage the neodymium magnets, there is still an appreciable range of temperatures over which the magnet could be used. Furthermore, a difference in magnetic remanence between magnets towards the periphery and those at the center of the magnet due to a temperature gradient could also affect performance.

Therefore, a temperature regulation system was designed to improve robustness of the magnet to fluctuations in environmental temperature.

3.4.1 Effect of temperature shift on magnet performance

The temperature coefficient of remanence for neodymium magnets is –0.12% per C°. As shown in Figure 3.25, a 1% deviation in field strength occurs with a temperature deviation of less than 10 C° which represents a moderately high, but reasonable temperature fluctuation that the system may experience. This deviation in field strength would significantly impact the operation of the system since both the RF electronics and the electromagnetic pulse would be tuned to the wrong frequency. Assuming a Q factor of approximately 100, a 1% deviation in frequency of operation would reduce sensitivity by 50%.

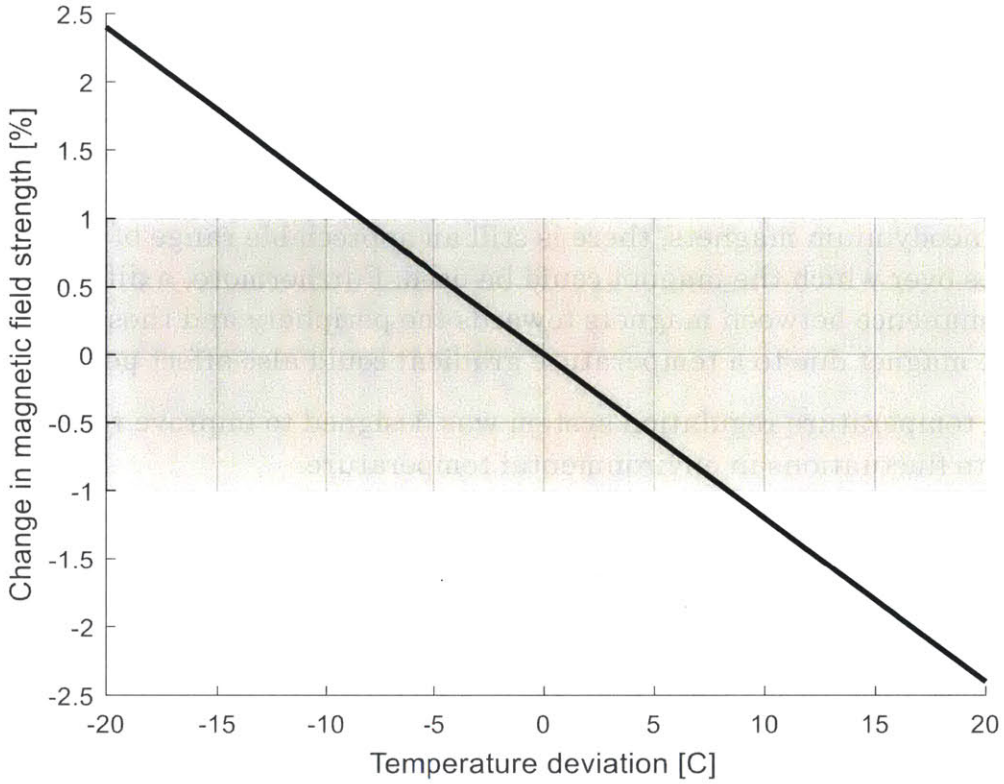

Figure 3.25. Calculated relationship between temperature and deviation in magnetic field strength.

3.4.2 Effect of temperature gradient on magnet performance

Numerical simulations using COMSOL were performed to understand the impact of temperature gradients on the magnet. Without a temperature regulation system, a temperature gradient would naturally form within the magnet as its environmental temperature changed. In a simple approximation, this temperature gradient could be treated as a linear function ranging from the old temperature inside of the magnet to the new temperature outside of the magnet. Performing simulations with temperature gradients of 1 and 10 C° resulted in changes in B_0 at the center of the uniform region of 0.0755% and 0.7627%, respectively. This suggests that a dynamic temperature gradient within the magnet ranging from 0 to 10 C° would be problematic to operation of the system at maximal sensitivity.

3.4.3 Integrated heat exchange system

A temperature regulation system was designed to reduce the impact of temperature variations on the magnet and ultimately system performance. This system could be used by either stabilizing the magnet temperature at a temperature different than that of the ambient temperature or it could be used to allow the magnet

temperature to more accurately track a change in ambient temperature through active temperature regulation.

The temperature regulation system consists of a fluid paths integrated into an aluminum housing that surrounds the magnet assembly. By circulating water at the desired temperature, the aluminum housing and subsequently the magnets will equilibrate at the same temperature as the water through conductive heat transfer. Fluid for this system can come from a water bath, ice bath, or, in a clinical setting, an FDA cleared water circulating pump [92].

The housing consists of four distinct blocks of milled aluminum. Figure 3.26 shows a rendering of a section view, where the top of the system has been removed, which clearly illustrates the first of four parallel fluid paths (diameter = 6.35 mm) milled into the aluminum. The four components of the housing are tightly secured to the magnet and each other to keep interfacial thermal conductivity high. Additionally, thermal paste, identical to that used in assembling the magnets, is used between the aluminum blocks and the magnet assembly. Fluid passes between the distinct components through direct couplings, each sealed with an O-ring.

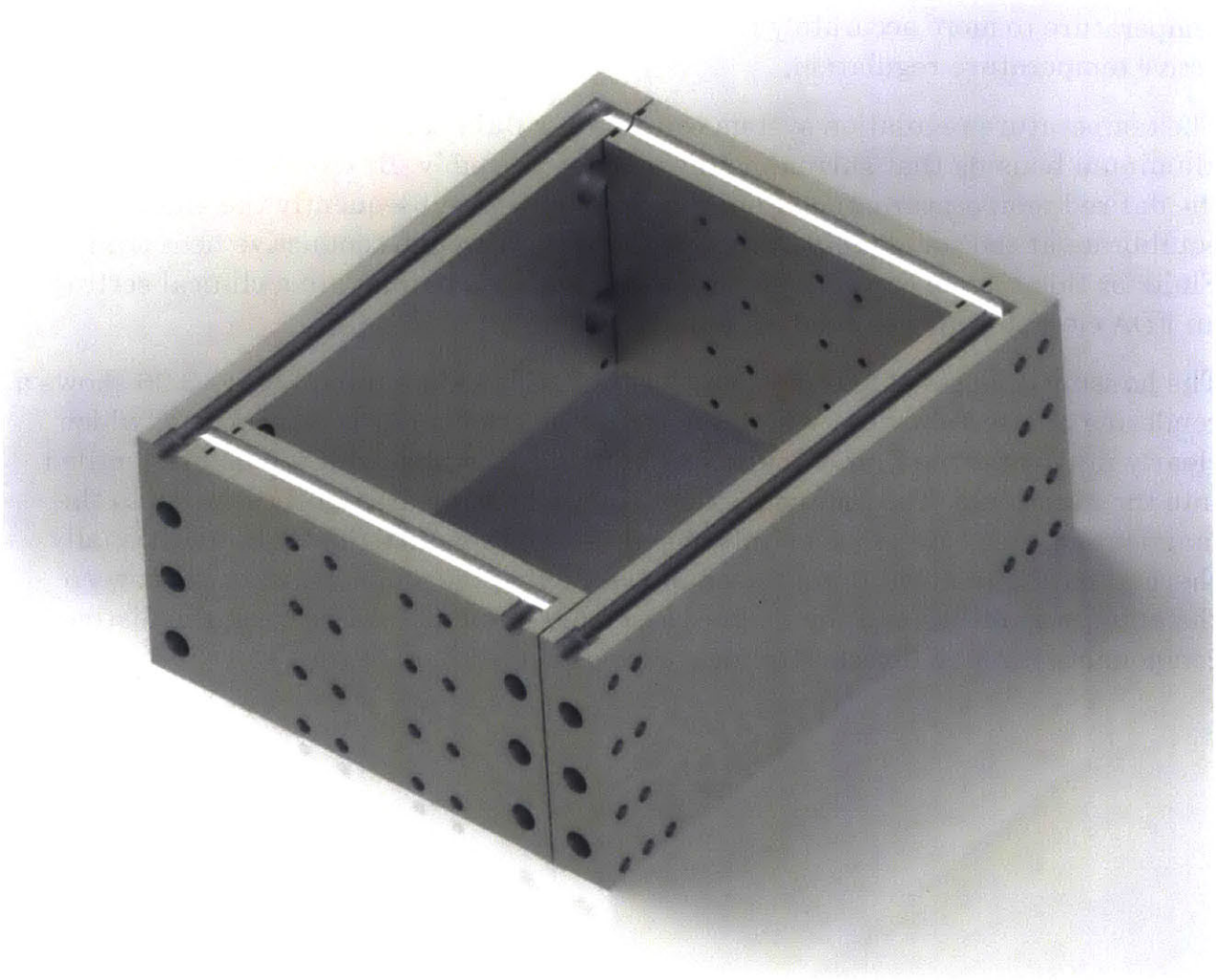

Figure 3.26. Temperature regulation system rendering, section view.

3.5 Magnet construction

3.5.1 Permanent magnet characterization

The magnet assembly was created with custom fabricated 12.7 mm (0.5 inch) cube, grade N52 neodymium magnets (Viona Magnets, Hicksville, NY) manufactured with a dimensional tolerance of 50.8 µm (0.002 inch).

Measurement of the magnetization properties of the custom manufactured neodymium magnets was performed. Data was acquired with a Hysteresisgraph AMH-500 BH-tracer (Laboratorio Elettrofisico Engineering, Milan, Italy) as shown in Figure 3.27. In order to fit inside of the testing chamber, the magnet was demagnetized, ground down to a cylinder of diameter 10.79 mm and thickness 2.52 mm, and then subsequently magnetized. This demagnetization/magnetization process was not a source of error in these measurements as it was validated to

produce reproducible magnetization within 0.2% of the original magnetization. Measurements of magnet performance were made at a temperature of 22 C°.

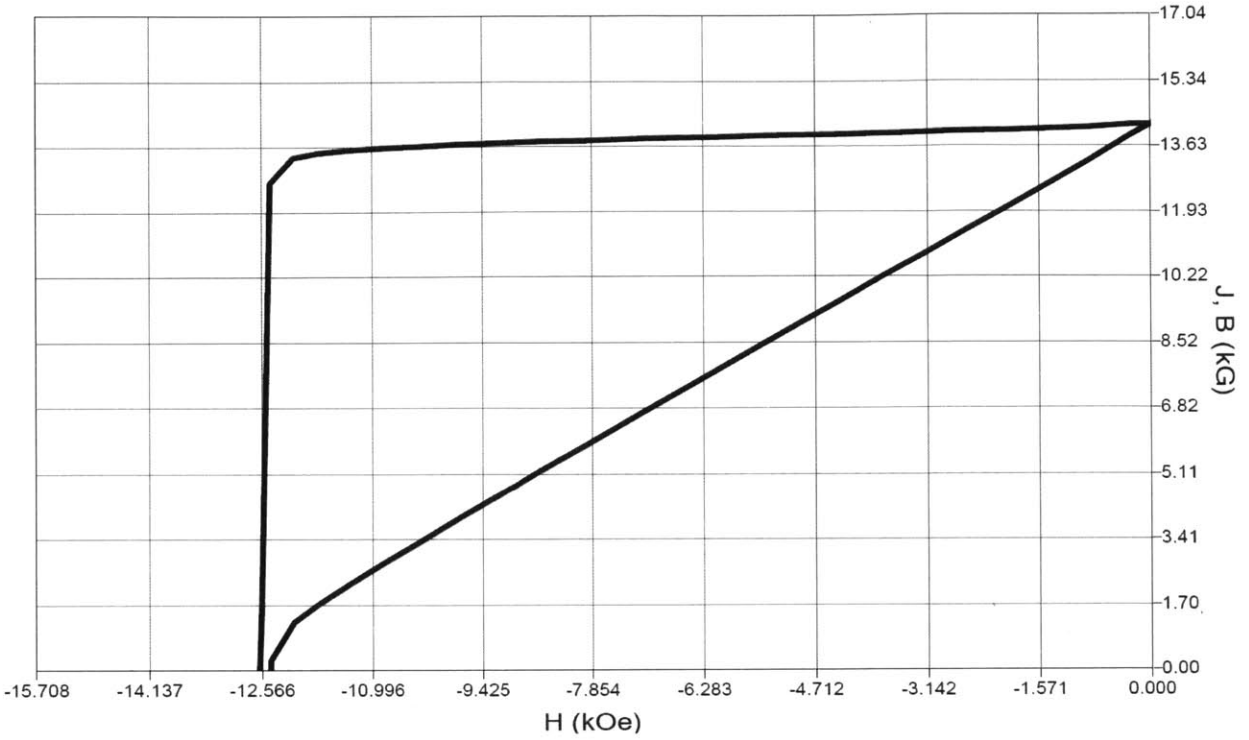

Figure 3.27. BH curve of cylindrical N52 neodymium magnet.

The custom manufactured magnets did not exactly meet the expected specifications, as shown in Table 3.15. The relative permeability is calculated based on the slope of the BH curve, as shown in Figure 3.27. This value of the relative permeability is valid when H is less than approximately 875 kA/m. This is of particular interest when attempting to explain the deviation between the expected and measured value of the strength of the magnetic field generated by the magnet assembly.

Magnetic property	Expected	Measured (mean ± std. dev.)	Error
Maximum energy product [T*MA/m]	0.414	0.384 ± 0.001	–7.3%
Remanence [T]	1.48	1.4243 ± 0.003	–3.8%
Coercivity [MA/m]	–	0.999 ± 0.003	–
Relative permeability	1	1.055	5.5%

Table 3.15. Expected and measured magnetic property values for N52 neodymium magnets.

3.5.2 Permanent magnet flux distribution

3.5.2.1 Characterizing flux distribution of permanent magnets

The flux produced by each magnet through a remote area was measured in a highly controlled manner. These values were then converted to remanence values by measurement of the remanence of a small subset of the magnets and subsequent derivation of a calibration curve. The results of this measurement are shown in Figure 3.28. A subset of the magnets was selected that maximized the average strength of the magnets with the added effect of reducing the range of variability. The blue region includes all 1000 magnets. The orange region includes the strongest 432 magnets excluding very strong outliers. μ indicates the mean of the region, Δ indicates the range of the region.

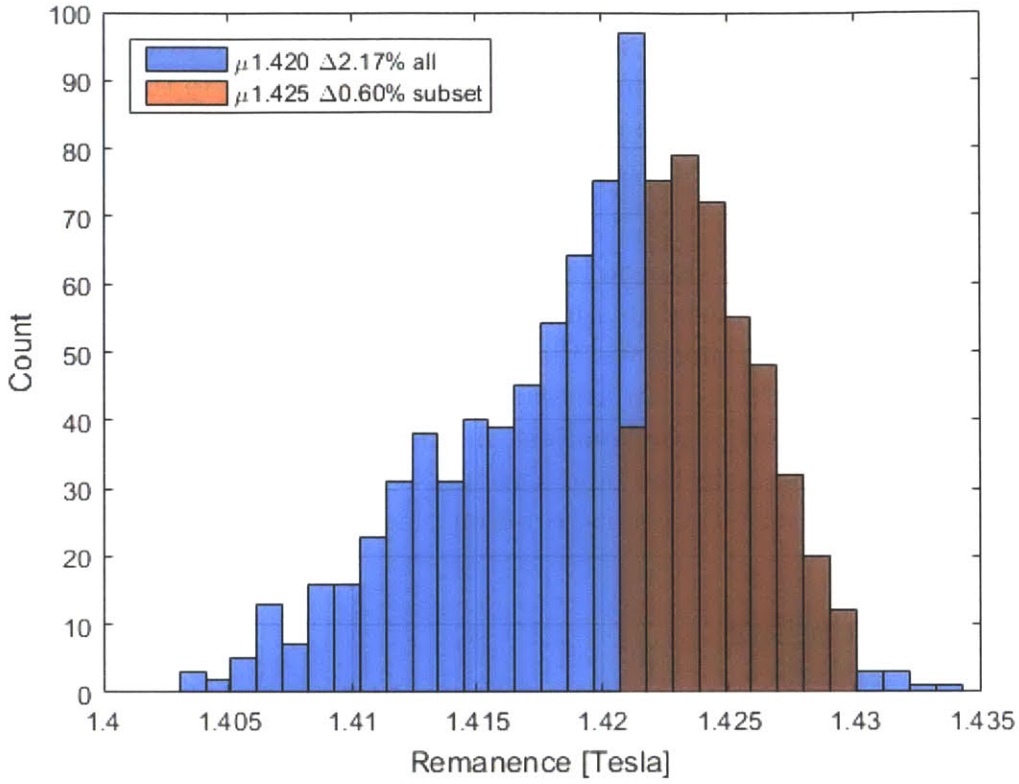

Figure 3.28. Histogram of remanence of each neodymium magnet.

By selecting a continuous subset of magnets the field strength of the magnet assembly was increased by about 0.5% due to the increased mean remanence of the magnets.

3.5.2.2 Effect of flux distribution of magnets on field of magnet assembly

A secondary question, motivated by the non-zero range of magnetic flux, or remanence, values found in the permanent magnets, asked if there was a particular placement of individual magnets into the assembly that would produce a superior magnetic field. Conversely, we asked if there were particular arrangements that ought to be avoided to prevent degradation of the magnetic field performance.

The answer this question, a numerical simulations of the magnet were performed with various placements of a randomly generated set of individual magnet remanence values.

A set of random magnet remanence values were generated, for all experiments, that were uniformly distributed over the range $\pm 0.8\%$ which closely approximated the distribution seen in a previously set of custom fabricated magnets from the same vendor. In the first experiment, each magnet was assigned its position within the

magnet assembly such that the strongest remaining magnet from the generated list was assigned to the unfilled position located nearest to the center of the uniform region of the magnetic field. In the second experiment, the same process was followed, but instead the weakest magnets were placed nearest to the uniform region. In the final experiment, the magnets were randomly assigned their position to simulate magnet assembly without any placement guidelines based on magnet strength.

The results of this simulation showed that random placement did not alter the magnetic field strength compared to a magnet assembly with no variation in the remanence of its constituent magnets. Placement of the strongest magnets nearest to the uniform region resulted in an increase in the field strength by 0.21% and complementarily, placement of the weakest magnets furthest from the uniform region resulted in a decrease in the field strength by 0.21%. This is not a significant change in field strength and, therefore, random placement of the magnets in the assembly was justified.

3.5.3 Magnet housing

The neodymium magnets are in a highly unstable, high energy state when placed into the desired configuration. Therefore, a housing capable of restraining the individual magnets was necessary. This housing was designed in Solidworks 2015 (Waltham, MA) and then milled from aluminum.

3.5.3.1 Material selection

The magnet housing was constructed from 6061 aluminum, a heat treated, high strength, nonmagnetic alloy. The main consideration in the choice of this material was its high strength and low magnetic susceptibility. It also exhibits good electrical and thermal conductivity. Electrical conductivity is important to reduce noise of system by allowing it to act as a ground plane. Thermal conductivity is important because it allows the temperature regulation system to control the temperature of the magnets more quickly and effectively than otherwise would be the case.

3.5.3.2 Magnet housing mechanical design

The magnet housing needed to constrain the position and orientation of each of the individual magnets that comprise the magnet assembly uniquely. Further, the housing needed to be designed such that the magnets could be easily and safety inserted without experiencing intractable forces from adjacent magnets. To avoid undue cost, the housing was designed to be milled using standard CNC milling techniques.

A modular design strategy was chosen which involved nine fixtures, or slices, each containing 48 magnets which were placed face to face after the magnets were inserted into their pockets. Figure 3.29 shows a rendering of a single aluminum fixture for housing the magnets that comprise a single xy plane of the magnet.

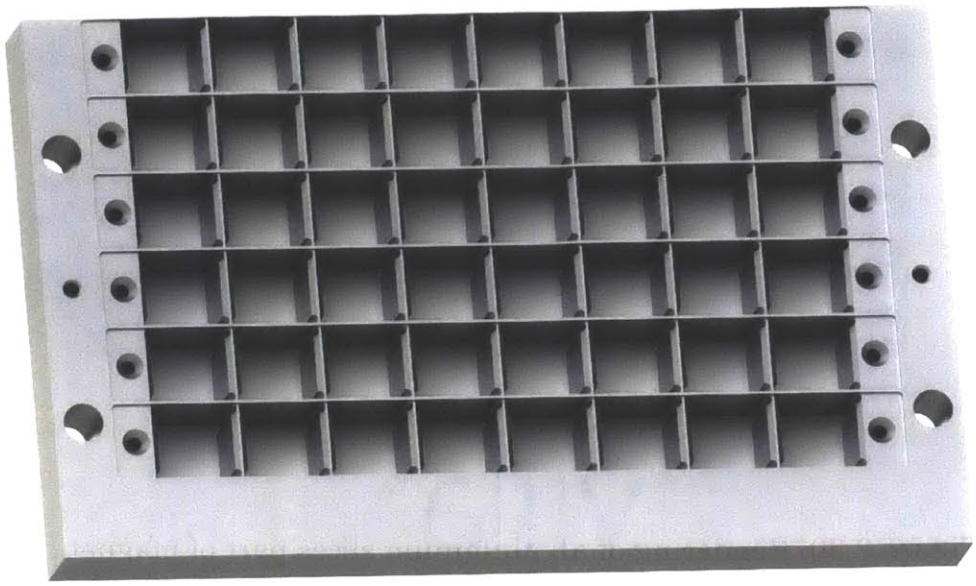

Figure 3.29. Rendering of a single aluminum fixture for the magnet assembly. Each square pocket has a side length of 12.7mm.

Figure 3.30 shows a rendering of all of the aluminum slices that are part of the housing assembly. For illustrative purposes, a single magnet is placed in the first row, a single row has its aluminum cover in place, and a single brass screw is fastening the cover on the right. Figure 3.31 shows an exploded view of all of the aluminum slices that are part of the housing assembly for illustrative purposes.

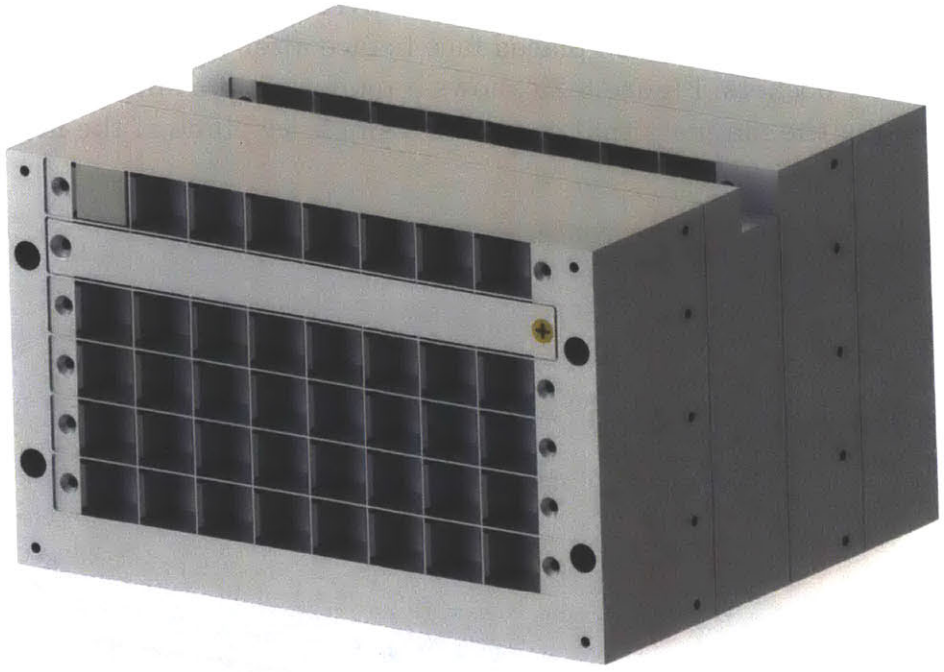

Figure 3.30. Rendering of all aluminum slices part of magnet assembly.

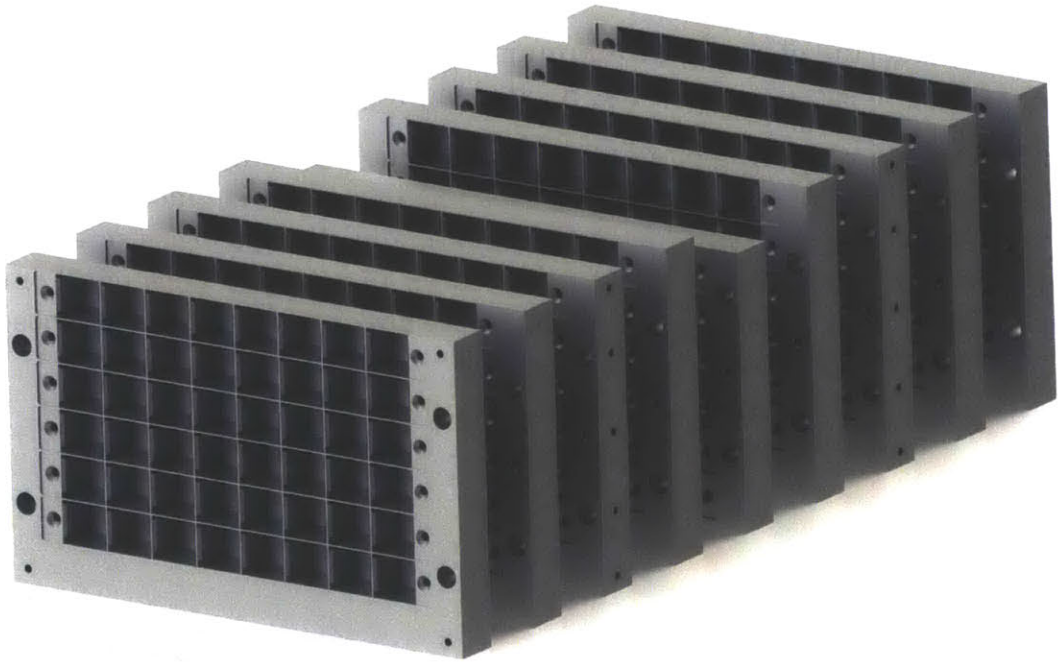

Figure 3.31. Rendering of all aluminum slices part of magnet assembly, exploded view.

The aluminum wall at the top of each slice was milled to the thickness of 318 μm to minimally intrude upon the uniform region. The vertical spacing between the magnets (y direction) was minimized under the constraint that the aluminum would not flex substantially under load from adjacent magnets. The same was true of the walls separating the magnets horizontally (x direction). The large through holes on each corner of the slice were used to align all of the slices face to face during assembly. For further alignment, brass dowel pins were placed in the small holes between each pair of alignment holes on the left and right side.

3.5.4 Magnet assembly

In order to improve the integrity of the magnet and efficiency of assembly, fixtures were designed to aid in assembly.

3.5.4.1 Magnet guidance fixtures

When inserting magnets into a slice fixture, previously inserted magnets in adjacent locations attempted to repel and rotate the magnet. This proved problematic at these forces of rotation were oftentimes greater than that which could be easily and consistently resisted manually. The consequences of failing to properly constrain the magnet during assembly were serious. The magnet that was about to be inserted would almost certainly snap onto an adjacent magnet. This was problematic because, due to the brittle nature of sintered neodymium magnets, there was a high risk of fracture and loss of magnetization when the magnets snapped together. This meant that both magnets needed to be discarded, or, at the minimum, tested again to ensure that magnetization was unchanged. Additionally, the strong attraction that the two magnets produced was difficult to overcome manually and had the potential to significantly contribute to assembly time.

An aluminum fixture was designed and milled to guide the placement of each magnet to address this issue. This allowed the maximum rotational or repulsive load that had to be manually resisted to be drastically reduced. A rendering of these fixtures is shown in Figure 3.32. Figure 3.33 shows a photograph of all four of the fixtures side by side. Four unique fixtures were designed where each, based on its orientation, was capable of guiding the placement of a magnet into two of the eight market pockets within a row.

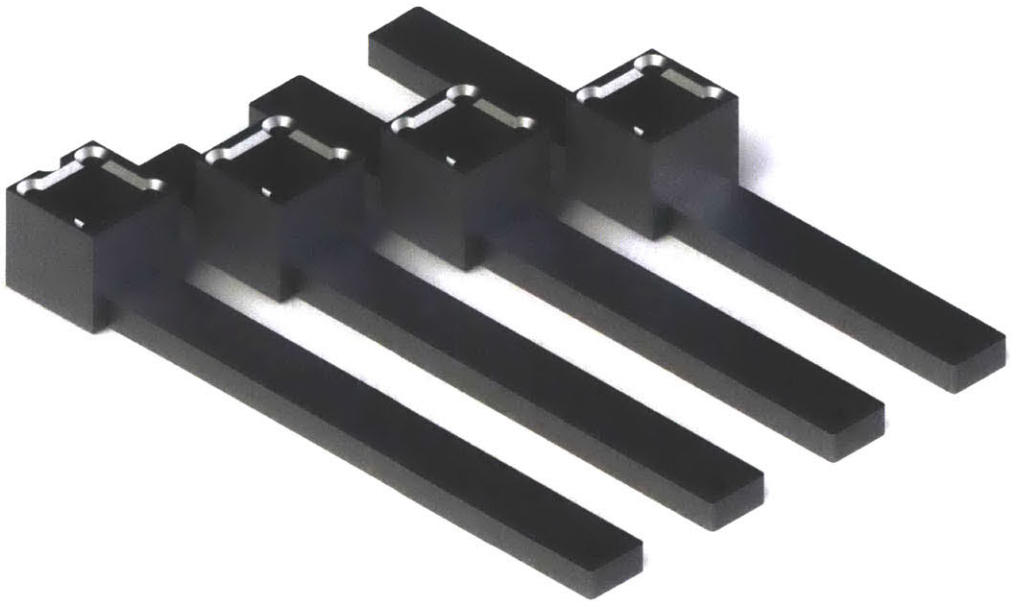

Figure 3.32. Rendering of fixture for magnet guidance during insertion.

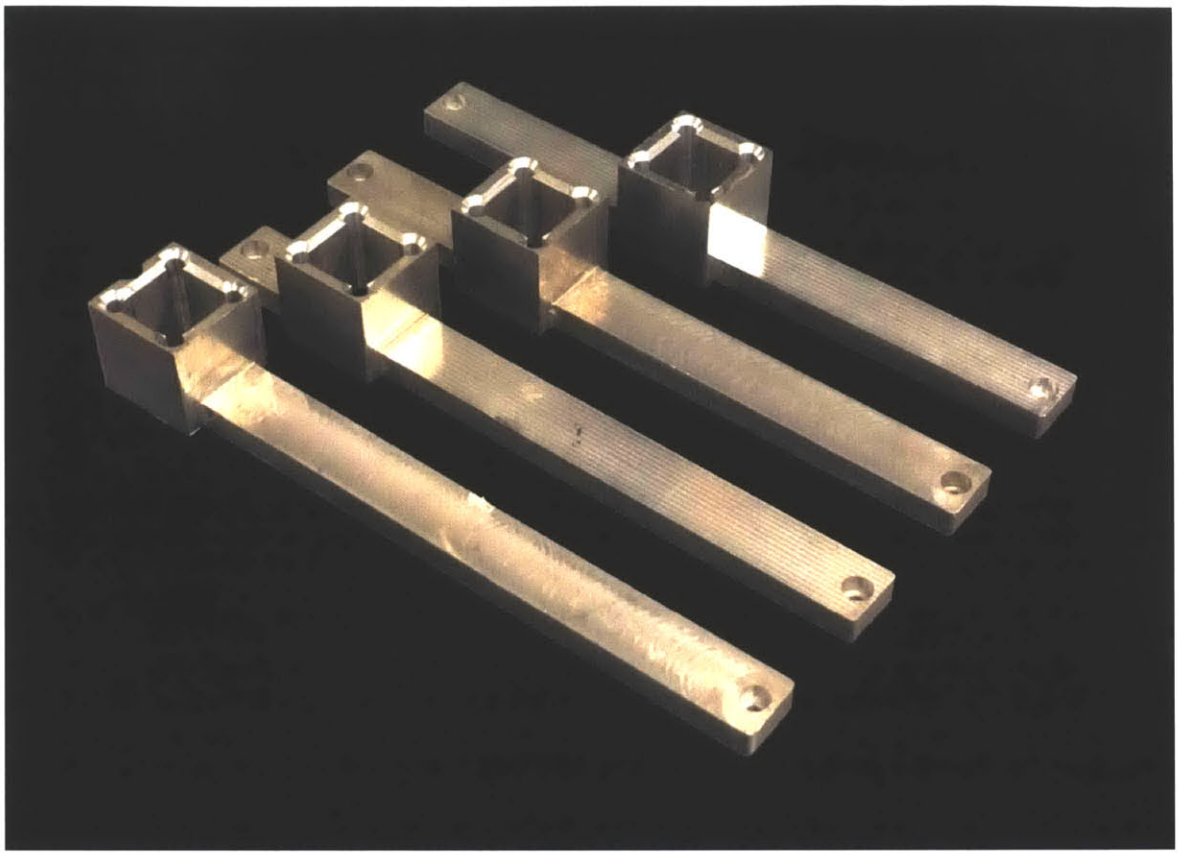

Figure 3.33. Photograph of fixtures for magnet guidance during insertion.

3.5.4.2 Thermally conductive paste

The thermal conductivity of aluminum is 235 W/(K*m) while that of a neodymium magnet is only 8.95 W/(K*m). These two materials are still both significantly higher than the thermal conductivity of air which is less than 0.05 W/(K*m). It is important to reduce regions of high thermal resistivity which would otherwise act to increase the time required for bring the entire magnet to thermal equilibrium in order to improve heat transfer from the temperature regulation system.

The deposition of highly thermally conductive (thermal conductivity 8.7 W/(K*m)) silver paste (AI Technology, Inc, Princeton Junction, New Jersey) into each pocket before insertion of a magnet was performed. This brought the space surrounding the magnet to a thermal conductivity much more similar to that of the magnet which will improve heat transfer from the aluminum fixture into the individual magnets.

3.5.4.3 Steel and PTFE backing on each slice

The magnets are in an unstable equilibrium when placed into a slice. As a result, a very small vibration or perturbation by an external magnetic field can cause the magnet to shift enough that it is now unstable. When this occurs, the magnets are

very quickly drawn out of their pocket and can either snap to an adjacent magnet or be ejected from the entire assembly with a high velocity. Both of these are very undesirable situations. The stress placed on the aluminum covers on each row of magnets was dramatically reduced by placing a thin (3.2 mm) sheet of steel behind the back face of each slice during and after magnet insertion. This improved the stability of the magnets both because the magnets were attracted to the steel and because the steel acted to shunt field lines away from adjacent magnets.

The steel remained at the back of each slice until assembly of adjacent slices was nearly complete. When the magnets were sufficiently physically constrained that perturbations would be unable to dislodge them, the steel was removed from the slice. A thin (0.25 mm) layer of low friction polytetrafluoroethylene (PTFE) was adhered to the surface of the steel, that was to be placed against the aluminum slice in order to facilitate its removal.

3.6 Magnet characterization

It was predicted that the field profile of the magnet would be similar to that predicted by numerical simulations. The shape and strength of the field were of particular interest as they define the region over which the system is sensitive.

3.6.1 Magnetic field characterization

A Hall effect based gaussmeter (Model 475 DSP Gaussmeter) combined with a hall probe (HMMT-6J04-VR, Lake Shore Cryotronics) was scanned in three dimensions through a Cartesian grid by three perpendicularly oriented linear stages (a ILS50PP stage and two ILS150PP stages, Newport Corporation, Irvine, California) controlled by a motion controller and driver (ESP300, Newport Corporation).

The field profile was measured in a 2D grid located immediately above the center of the magnet. After interpolation to aid in visualization, the field profile was rendered as a contour plot, as shown in Figure 3.34. Measurements were taken with a grid spacing of 150 μm.

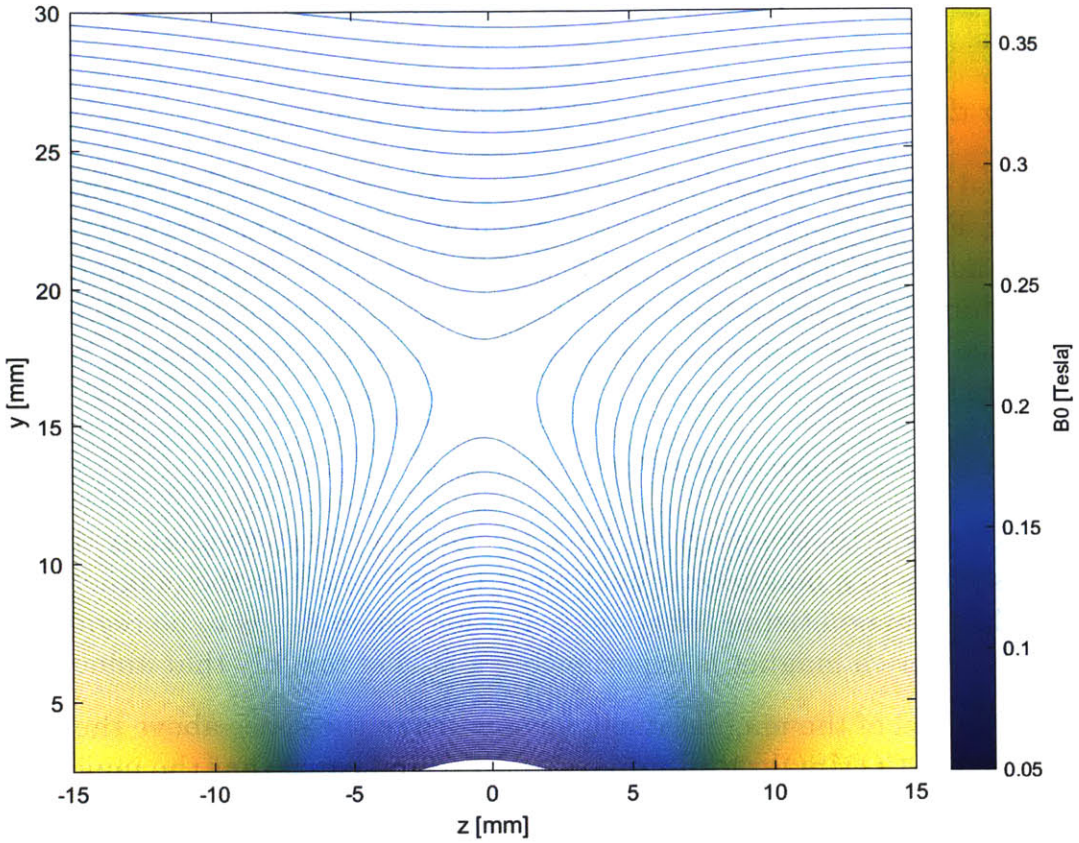

Figure 3.34. Measured field profile above center of magnet.

A second field profile was measured in a 3D grid located immediately above the center of the magnet to compute the location and size of the uniform region more precisely.

	Simulation	**Measured**
Magnetic field strength [Tesla]	0.243	0.169
Distance from surface [mm]	17	17
Size, z-dir [mm]	3	3
Size, y-dir [mm]	4	4

3.6.2 Discrepancy between measured and simulated magnet

The shape of the field generated by the magnet agrees well with that predicted by numerical models. The strength of the field, however, was approximately 30% lower

than predicted by numerical simulations. Attempting to understand the reasons for this deviation is valuable both to identify errors in assembly as well as guide future design efforts.

3.6.2.1 Error due to differences in expected magnetic properties

The numerical simulations rely upon a correct value of the remanence and relative permeability. Furthermore, there is an implicit assumption that both the remanence and relative permeability are both independent of the magnetic field strength within the magnet. As shown in Table 3.15, there was a deviation in both the remanence and the relative permeability of the magnets which may have contributed to the error.

3.6.2.2 Error due to interactions between magnets

As shown in Table 3.15, the magnets have a coercivity of approximately 999 kA/m which corresponds to a magnetic induction of 1.255 Tesla. For the magnets to have an appreciable demagnetizing effect on each other, there needs to be regions within the assembly where a magnet is experiencing a field of roughly that amount.

A numerical model of the magnet itself, as opposed to the space above the magnet, was performed in COMSOL. Preliminary analysis indicated that the majority of the volume of the magnets was not exposed to magnetic fields greater than their coercivity in the direction opposing their magnetization. Further analysis of the effect of coercivity may be necessary, will almost certainly not account for the majority of the observed deviation in field strength.

3.6.2.3 Error due to environmental effects

The laboratory can fluctuate in temperature by at most 10 C° over the duration of several days. Assuming that the temperature coefficient of remanence of our magnets is –0.12%, this would explain at most a 1.2% decrease in the field strength.

We are unable to ultimately fully account for the difference in field strength between the simulated and measured magnet. 4% of the 30% error can be accounted for by the lower remanence of the individual magnets. The remaining difference may be a result of measurement error, unaccounted for interactions between magnets within the assembly, or an error our implementation of the numerical model.

3.7 Future work

3.7.1 Temperature regulation

The temperature regulation system has been designed and constructed, but not yet tested. It is important to develop an understanding of the effect of temperature on the size, shape, and strength of the uniform region of the magnetic field with and without the active temperature regulation afforded by this system. If the magnetic field changes in strength significantly from environmental temperature fluctuations, active control over the temperature or the matching circuit and spectrometer will need to be implemented. Highly repeatable measurements for investigative purposes may be more easily acquired and compared when taken with an NMR system operating at a constant field strength. Depending on the use case, deployment of the measurement system with a fluid circulating temperature regulation system may not be feasible.

3.7.2 Numerical modeling

The discrepancy between the simulated and measured field strength of the magnet has not yet been accounted for. Further efforts directed at uncovering the source of this error will be critical before further magnet development can be justified. Although the shape of the field strength was accurately characterized by the simulation, both the shape and the strength of the field are important parameters that define the behavior of the measurement system. Next steps will include attempting to simulate and build simpler magnet assemblies to characterize the interaction between nearby magnets.

This page intentionally left blank

Chapter 4

RF impedance matching circuit

NMR is typically conducted at frequencies in the megahertz range which falls within the radio frequency range of the electromagnetic spectrum due to the gyromagnetic ratio relevant to ^{1}H NMR and the field strength of the static magnetic field used. Radio frequency signals cannot be efficiently transmitted over traditional conductors and, therefore, transmission lines must be utilized. These transmission lines possess a characteristic impedance which others loads coupling to the transmission line must match to achieve efficient power transfer. Poor impedance matching can lead to reflection and standing waves which both have the potential to both corrupt the signal, reduce signal to noise ratio, and damage either of the loads.

In NMR, during application of the electromagnetic B_1 pulse, an RF amplifier generates a pulse which must be transmitted into the sample through an RF coil, or NMR probe. The pulse cannot be directly sent from the transmission line to the RF coil due to an impedance mismatch.

Therefore, an impedance matching circuit is necessary to transform the impedance of the coil into a load that couples to the transmission line effectively. We hypothesized that an impedance matching circuit build from discrete components, including tunable nonmagnetic capacitors, would provide suitable matching while providing a foundation for future work in automated impedance matching systems. This chapter details the theoretical basis, design, fabrication, and testing of this circuit.

4.1 Theory of impedance matching

The difference in impedance between the source and the load in a system causes reflection of some of the input power which reduces the efficiency of the system. The magnitude of the reflected power can be quantified by the reflection coefficient as given by

$$\Gamma = \frac{Z_L - Z_s}{Z_L + Z_s} \tag{4.1}$$

where Γ is the reflection coefficient, Z_L is the load impedance, and Z_s is the source impedance. Setting Γ to zero and solving for a relationship between Z_L and Z_s

indicates that minimal reflection is achieved when the two impedances are equal to each other.

Maximal power transfer is achieved when $Z_L = Z_S^*$ where Z_S^* is the complex conjugate of Z_S. In the general case, there is not necessarily a Z_L that satisfies both conditions. Fortunately, the transmission line has a characteristic impedance of 50 Ω with no imaginary component. Therefore, if Z_L is also set to 50 Ω then reflection is minimized and power transfer is maximized. In order to do this, the impedance of the RF probe must be transformed to 50 Ohm through the use of a matching circuit.

4.2 Design of the RF circuit

A matching circuit, designed to transform the impedance of the NMR probe to the desired load impedance, Z_L, needs to be designed. This circuit needs to operate across a range of RF frequencies and have minimal resistive losses to allow most of the power dissipation in the load to occur across the NMR probe itself.

4.2.1 Circuit topology

There are circuit topologies that enable wideband impedance matching, but a narrow band circuit was selected due to simplified design requirements, less resistive losses, its ability to achieve a more accurate match, and its more effective noise suppression.

A lumped element L-network was chosen for the desired circuit topology as it has been shown to provide a simple, high Q factor matching network for radio frequency operation.

An NMR probe typically consists of a coil wound into a solenoid or surface coil from insulated wire. Therefore, using a lumped parameter model, the probe can be modeled using an inductive and a resistance component in series. Its complex impedance can be expressed as

$$\mathrm{Z_{coil}} = R_{coil} + sL_{coil} \tag{4.2}$$

where Z_{coil} is the complex impedance of the coil, R_{coil} is the resistance of the coil, L_{coil} is the inductance of the coil, and s is a complex frequency equal to $j\omega$. Based on typical values of NMR probes, the resistance of the coil is less than 50 Ohm and its reactive term is always inductive rather than capacitive.

Therefore, the L-network shown in Figure 4.1 is guaranteed to be able to provide the required impedance transformation for a unique set of values for C_M and C_T.

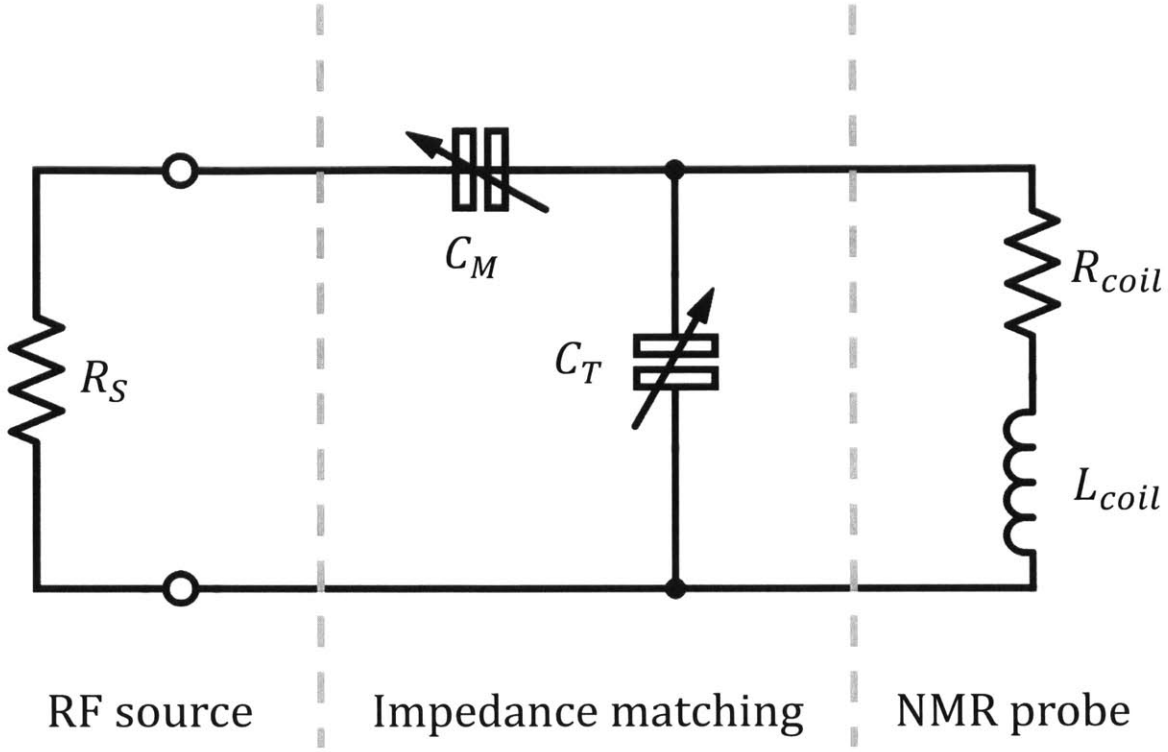

Figure 4.1. Circuit schematic illustrating impedance matching circuit.

4.2.2 Matching conditions

The equivalent impedance of the load that the source sees is given by

$$Z_L = Z_M + Z_T \parallel Z_{coil} \tag{4.3}$$

where Z_M is the complex impedance of the matching capacitor and Z_T is the complex impedance of the tuning capacitor.

This can be expanded as given by,

$$Z_L = \frac{1}{C_M s} + \frac{1}{C_T s} \parallel (R_{coil} + L_{coil} s) \tag{4.4}$$

where C_M is the capacitance of the matching capacitor and C_T is the capacitance of the tuning capacitor.

Further expansion and rearrangement gives,

$$Z_L = \frac{1}{C_T s + (R_{coil} + L_{coil} s)^{-1}} + \frac{1}{C_M s} \tag{4.5}$$

The real component of Z_L is given by

$$Re\{Z_L\} = \frac{R_{coil}}{(\omega^2 C_T L_{coil})^2 + (\omega C_T R_{coil})^2 - 2\omega^2 C_T L_{coil} + 1} \tag{4.6}$$

and the imaginary component of Z_L is given by

$$Im\{Z_L\} = -\frac{1}{\omega C_M} - \frac{\omega(\omega^2 C_T L_{coil}^2 - L_{coil} + C_T R_{coil}^2)}{(\omega^2 C_T L_{coil})^2 + (\omega C_T R_{coil})^2 - 2\omega^2 C_T L_{coil} + 1} \tag{4.7}$$

This suggests that the real component can be matched to 50 Ohm by only adjusting C_T. Then, for a given value of C_T, the necessary value of C_M to bring the imaginary component to 0 can be found. This turns out to be theoretically valid though accurate to implement in practice.

These results show that the frequency to which the circuit is tuned to is only dependent on the inductance of the coil and the value of the tuning capacitor, as given by

$$\omega_M = \frac{1}{\sqrt{L_{coil} C_T}} \tag{4.8}$$

where ω_M is the match frequency.

Furthermore, the set of values of C_T can be constrained to one of two possible values by setting the real component of the load impedance equal to the source impedance as given by

$$C_T = \frac{L_{coil} \pm \sqrt{\frac{R_{coil} L_{coil}^2 \omega^2 + R_{coil}^3 - R_{coil}^2 R_s}{R_s \omega^2}}}{L_{coil}^2 \omega^2 + R_{coil}^2} \tag{4.9}$$

where R_S is the source impedance. Note that ω_M differs from ω as ω_M is the frequency at which the real component of Z_L is maximized while ω is the desired operating frequency of the NMR probe. This desired operating frequency is set by the strength of the magnetic field.

Setting the imaginary component of Z_L to 0 and solving for C_M gives an expression for C_M as shown by

$$C_M = \pm \frac{\sqrt{\frac{1}{R_s}(R_{coil} L_{coil}^2 \omega^2 + R_{coil}^3 - R_s R_{coil}^2)}}{L_{coil}^2 \omega^3 + R_{coil}^2 \omega} \tag{4.10}$$

Figure 4.2 and Figure 4.3 illustrates the complex impedance of the load at the end of the transmission line and reflection coefficient as a function of frequency when both tuned and matched to a particular NMR probe. The transmission line

characteristic impedance was 50 Ω, the operating frequency was 7.195 MHz, the resistance of the coil was 5 Ω and its inductance was 6 μH in this case. The values of C_T and C_M necessary to achieve tuning and matching were 55.8 pF and 27.4 pF, respectively.

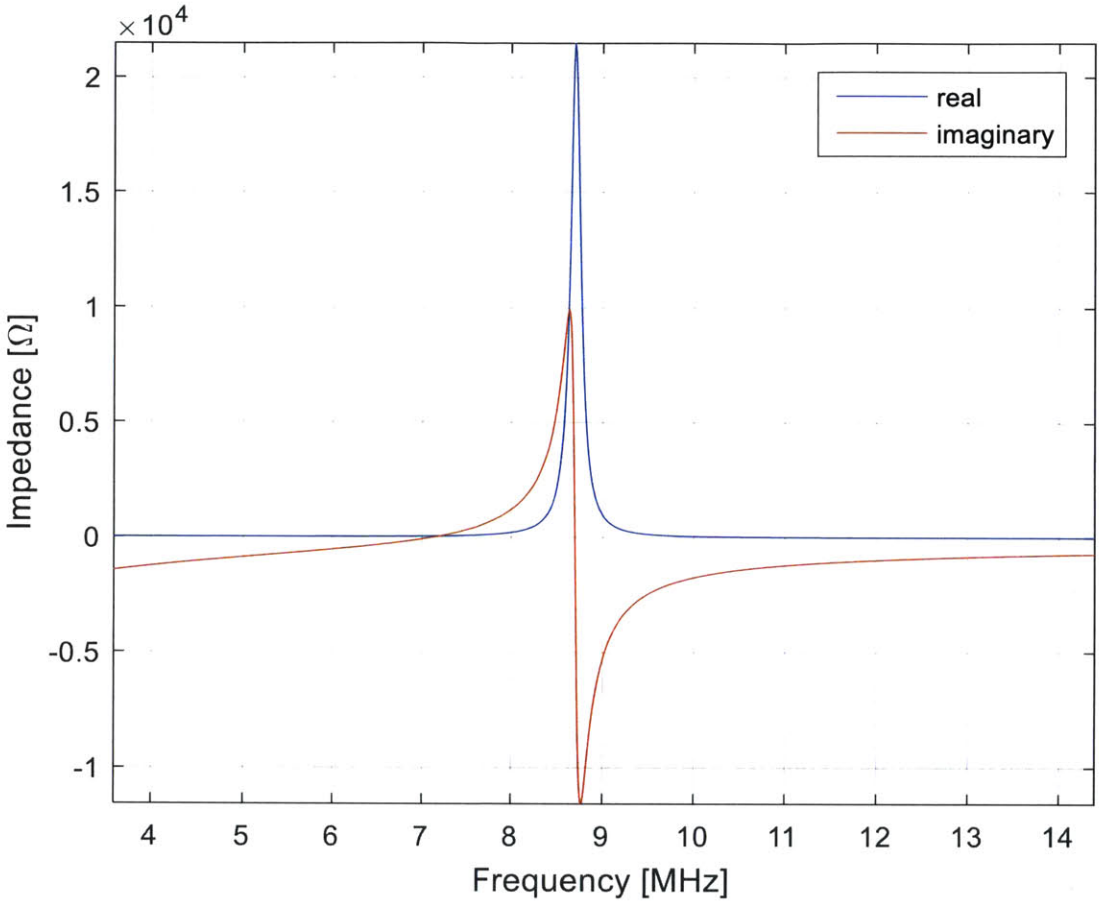

Figure 4.2. Complex impedance of load versus frequency after matching.

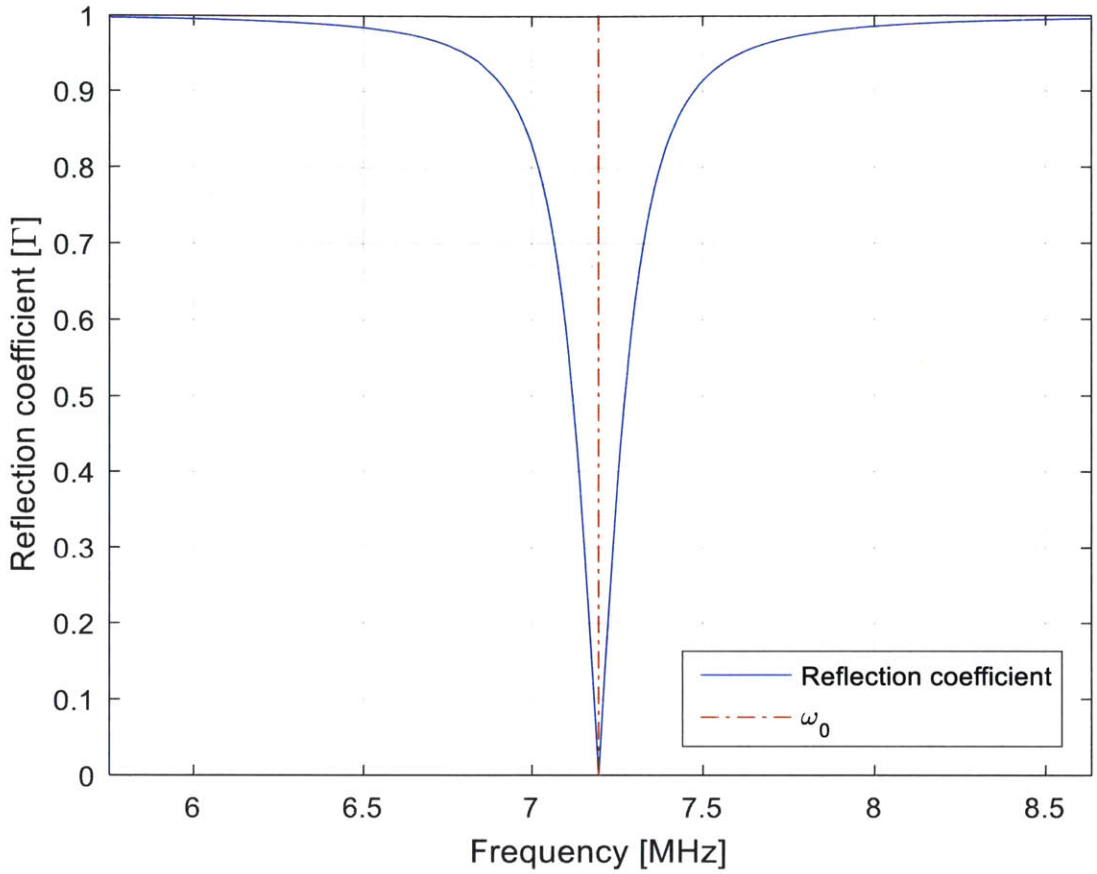

Figure 4.3. Reflection coefficient verses frequency when both tuned and matched.

Figure 4.4 and Figure 4.5 show the impedance of the load, as seen from the transmission line, as a function of frequency when tuned and matched to a coil with various resistance values with the same parameters as previously described. Successful tuning is possible across this wide range of resistance values. It is important to note that different values of capacitors as well as tuning frequencies are required to achieve proper impedance transformation. A summary of these different values is shown in Table 4.1.

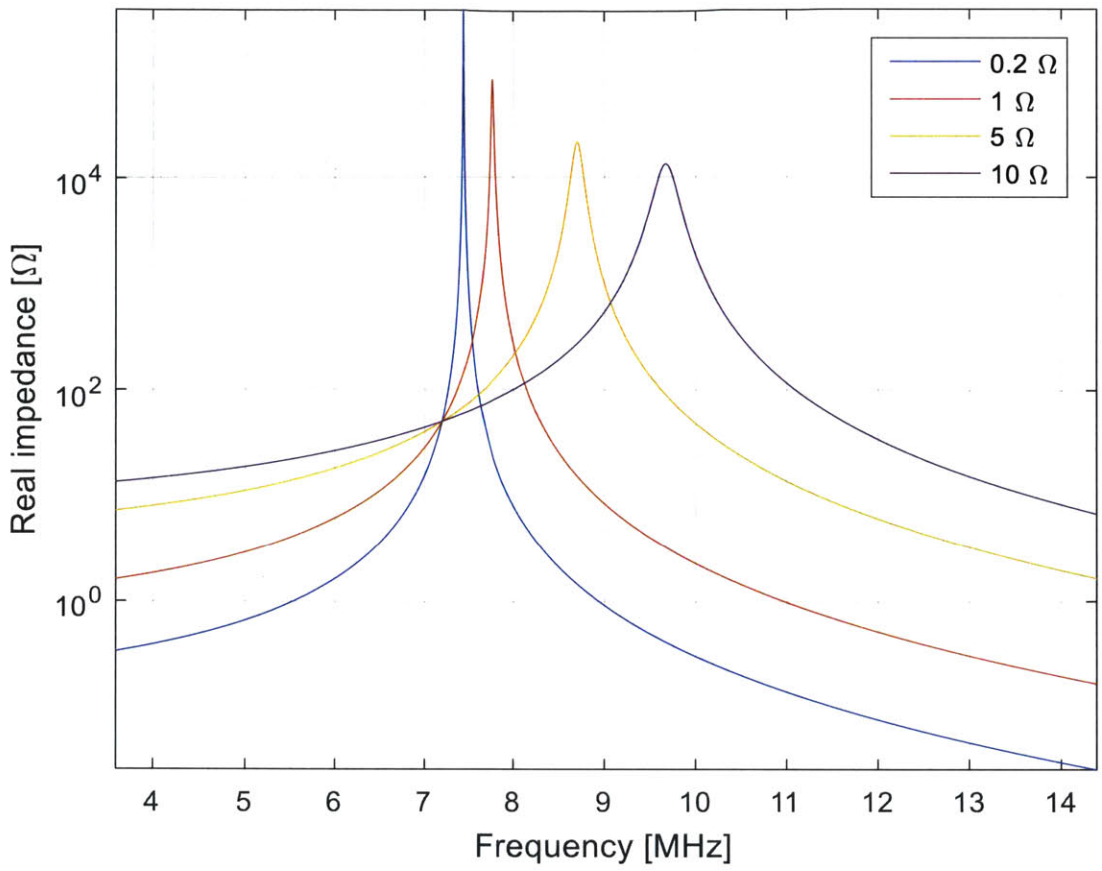

Figure 4.4. Real component of matched load with various coil resistances.

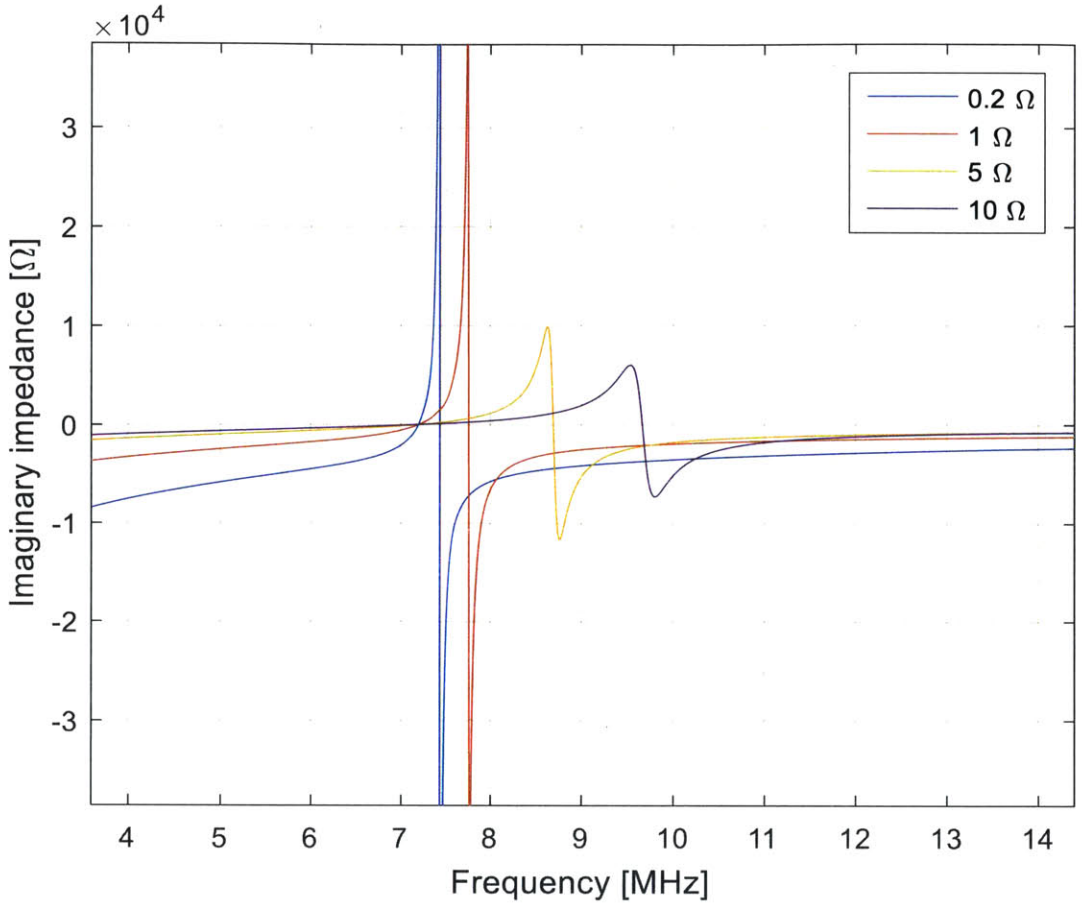

Figure 4.5. Imaginary component of matched load with various coil resistances.

R_{coil} [Ω]	C_T [pF]	C_M [pF]	ω_M [Mrad/sec]
0.2	76.39	5.16	46.71
1	70.02	11.54	48.79
5	55.78	25.83	54.66
10	45.11	36.57	60.78

Table 4.1. Capacitor values and match frequencies for various coil resistances.

Figure 4.6 and Figure 4.7 show the impedance of the load, as seen from the transmission line, as a function of frequency when tuned and matched to a coil with various inductance values with the same parameters as first described. Once again, successful tuning is possible across this wide range of inductance values, but different values of capacitors and tuning frequencies are required to achieve proper impedance transformation. A summary of these different values is shown in Table 4.2.

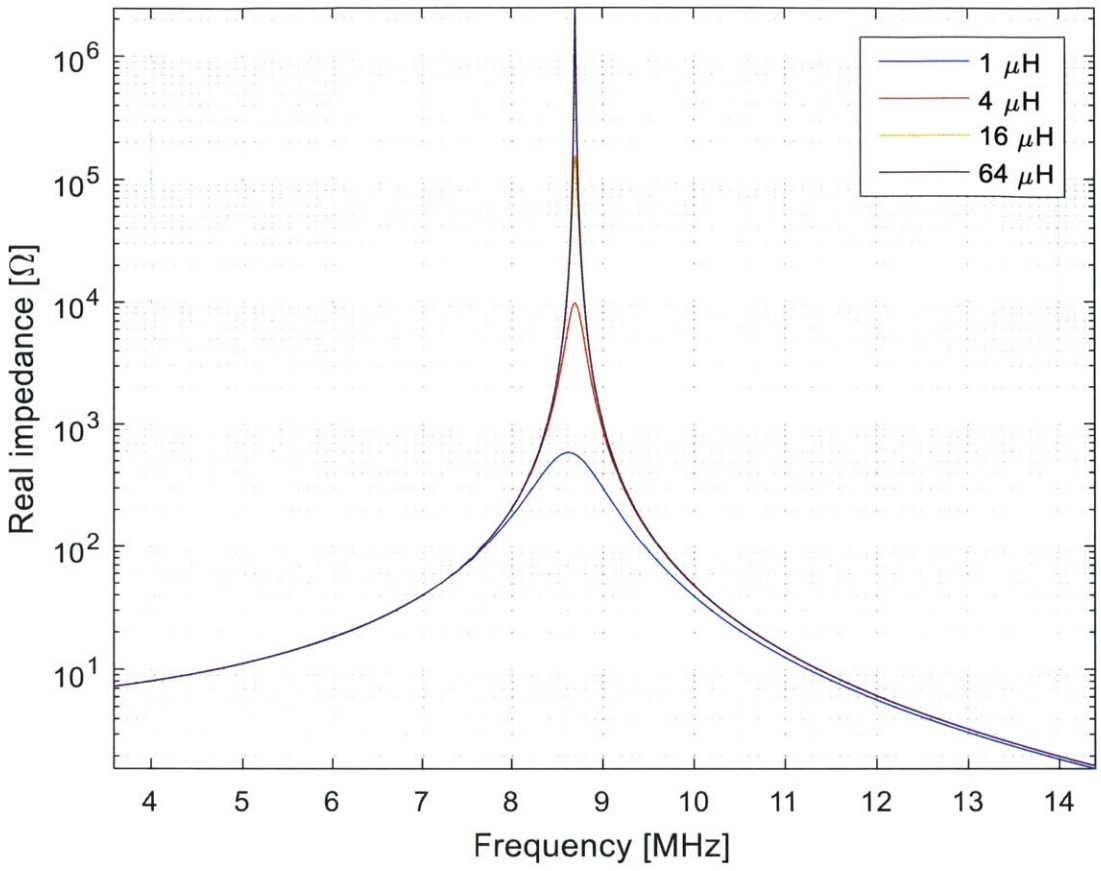

Figure 4.6. Real component of matched load with various coil inductances.

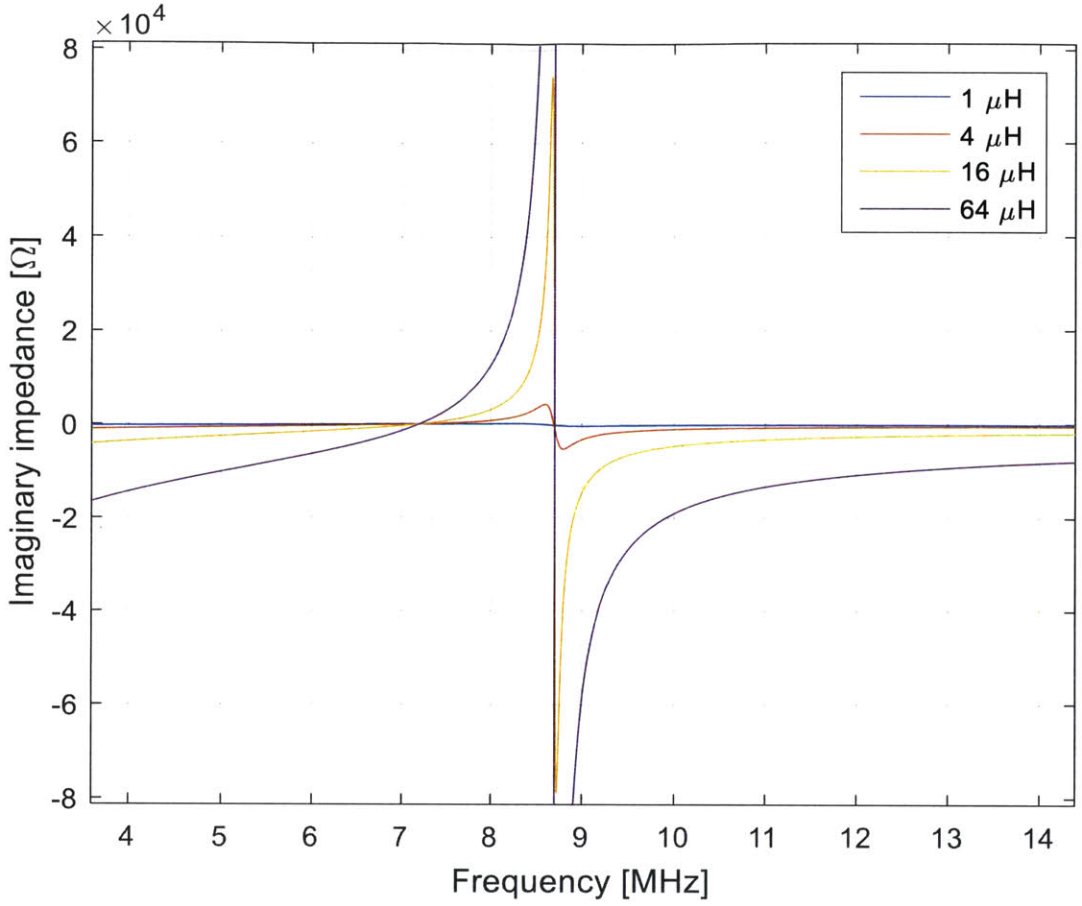

Figure 4.7. Imaginary component of matched load with various coil inductances.

L_{coil} [μH]	C_T [pF]	C_M [pF]	ω_M [$Mrad/sec$]
1	339.19	164.02	54.30
4	83.71	38.82	54.65
16	20.91	9.67	54.67
64	5.23	2.42	54.67

Table 4.2. Capacitor values and match frequencies for various coil inductances.

These results may, at first, suggest that any arbitrary coil can be successfully matched using this circuit. Rather, upon examination of these results, it is evident that this network is only capable of matching loads which satisfy the following expression

$$\omega^2 L_{coil}^2 + R_{coil}^2 - R_S R_{coil} > 0 \tag{4.11}$$

While a very precise value of R_S and ω are typically known in practice, the same is not true of L_{coil} and R_{coil}. R_{coil} is dependent on the amount of wire used to both wind the coil and connect it to the impedance matching circuit. This length can be variable depending on the final positioning of the NMR probe. L_{coil} is dependent on coil geometry which, while usually well-established when impedance matching, is not always well controlled as minor deformation can occur during final positioning.

Furthermore, the inductance of the coil is a dependent on the environment that the coil is placed within. The presence of materials with variable relative permeability, conductance, or surface currents can create a mutual inductance with the NMR probe coil in a highly uncontrolled manner. Therefore, approximate tuning of the circuit during assembly is sufficient as further tuning often occurs immediately before and during measurements.

4.2.3 Mechanical design

4.2.3.1 Design constraints

A housing for the impedance matching circuit was designed to mechanical secure all of the components, provide electrical isolation, and electrical shielding. All components were press fit into holes in the inside of the hollow box and subsequently glued into place with cyanoacrylate.

The inside of the box was fabricated from PEEK (polyether ether ketone) for electrical isolation, essential to reduce contamination of the signal with noise and maintain safe operation. PEEK is highly insulating (electrical resistivity of $4.9 * 10^{14}\ \Omega\, m$), easily machined, durable enough to support press fitting, and has a high melting temperature (340 C°) which enables soldering without damaging its surface.

The outside of the housing was fabricated from aluminum for electrical shielding which was important to avoid contamination of the signal from external electromagnetic radiation, such as that from nearby electronics. Aluminum provides a good compromise between conductivity, strength, ease of machining, and affordability.

4.2.3.2 Components

A female SMA jack (SMA Straight PCB Jack, Amphenol RF #132291) was used to interface the transmission line to the circuit. The jack was press fit into the hole on the left in both the aluminum and the PEEK. The maximum voltage that can be applied across this jack is 670 V_{rms} which may be of interest when attempting to send very high power B_1 pulses. Unfortunately, there is no definitive, nondestructive method of establishing if the jack has failed upon application of high

voltages. It is possible that the insulation resistance would decrease or a short circuit between the ground and signal pins would form at a lower voltage due to the presence of a carbon track. Figure 4.8 and Figure 4.9 show a rendering and photograph, respectively, of the impedance matching circuit with an SMA jack already mounted. The holes on the right side of the housing serve as mounting points for the variable capacitors. The four holes on the corner of the housing serve as mounting points for the entire housing onto the housing of the magnet. It is important to keep this circuit as close as possible to the RF coil to minimize resistance losses which maximize power transmission into and out of the coil.

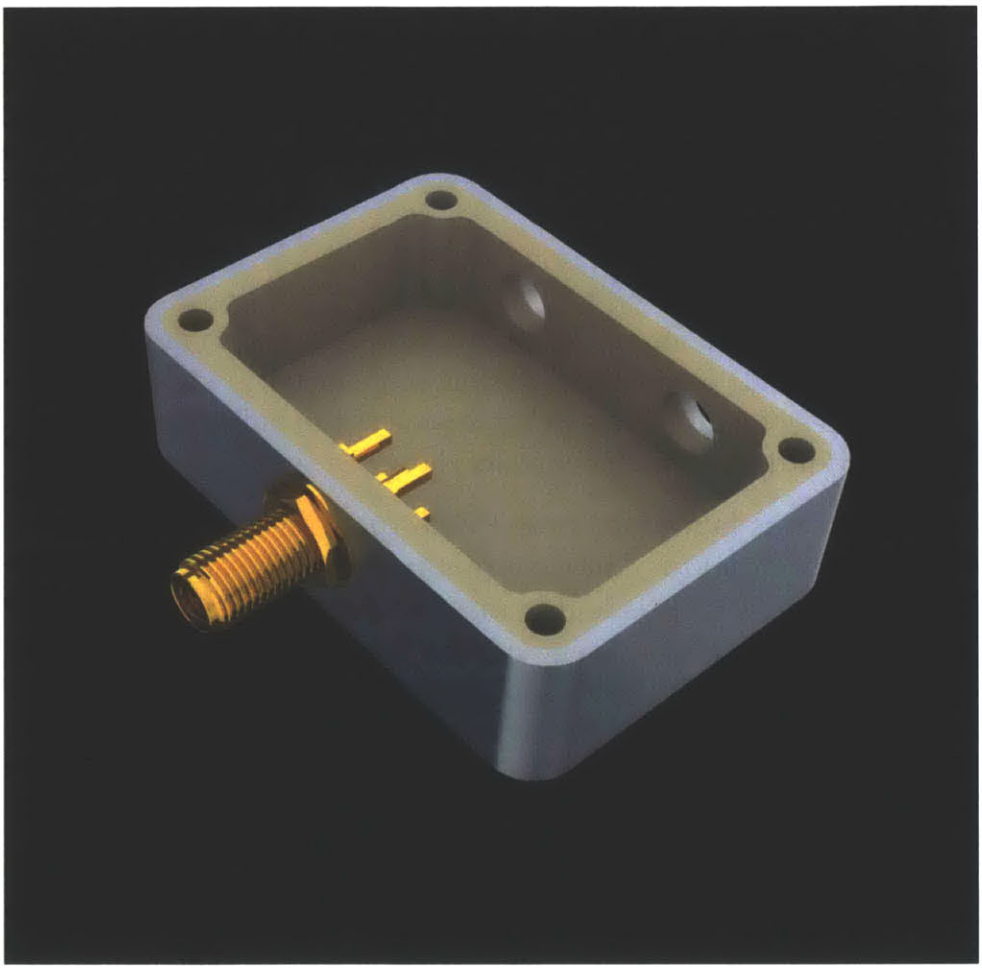

Figure 4.8. Rendering of impedance matching circuit housing with SMA jack.

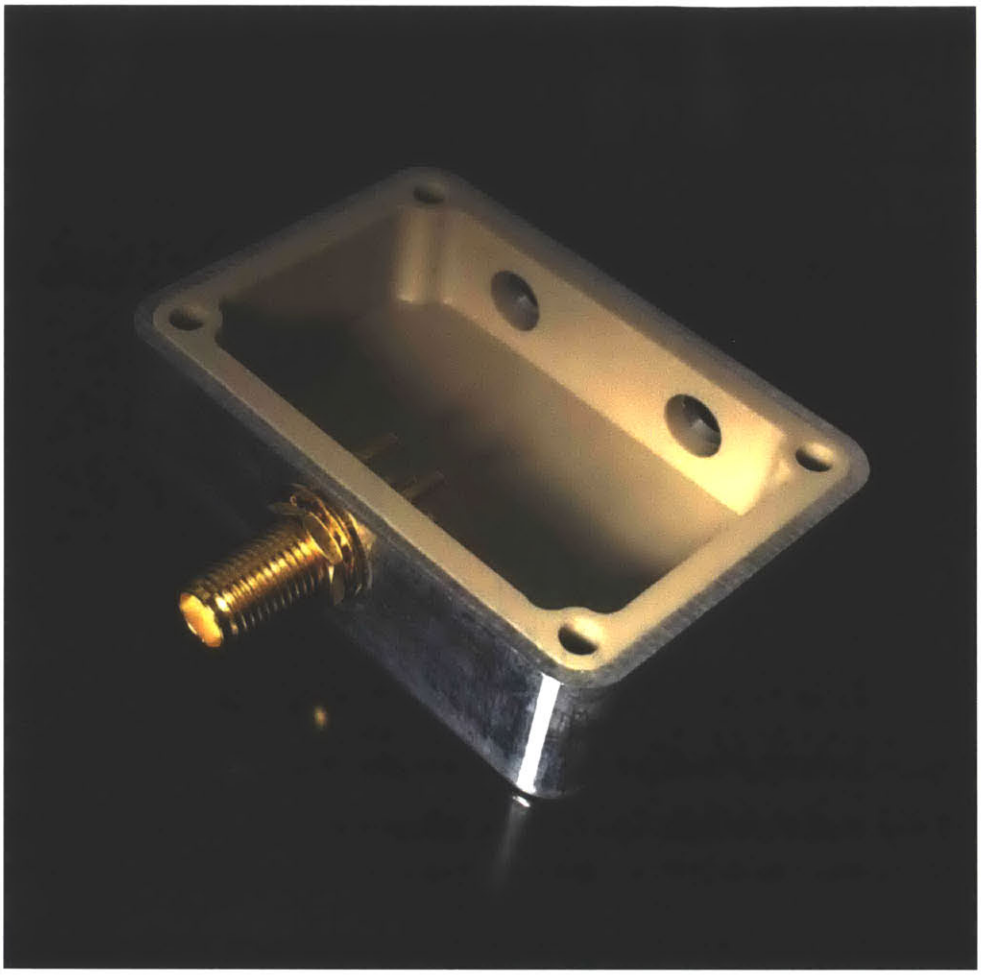

Figure 4.9. Photograph of impedance matching circuit housing with SMA jack.

Two non-magnetic, self-locking constant torque variable capacitors (Johanson Manufacturing 5641) were mounted within the housing to serve as the tuning and matching capacitors of the circuit in Figure 4.1. Each capacitor had a range of 1 to 30 pF and a Q factor of 100 at 100 MHz. The capacitors were designed to withstand a continuous voltage limit of 250 V and a pulsed (60 sec) voltage limit of 500 V. Once again, damage from high voltage is not easily detectable and can result in an increased dissipation factor as dielectric breakdown would result in carbon deposition on the electrodes.

4.2.3.3 Constructed circuit

Figure 4.10 shows a photograph of the fully assembled impedance matching circuit. The tuning capacitor is at the bottom and the matching capacitor is at the top of the image.

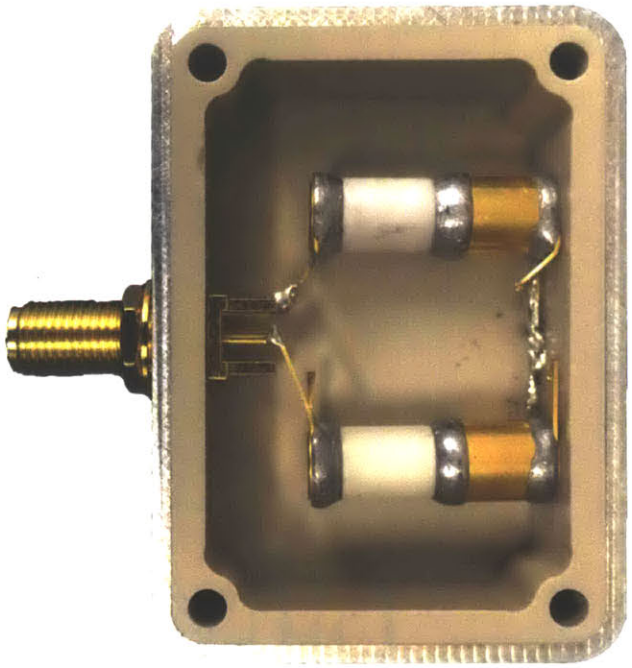

Figure 4.10. Photograph of fully assembled impedance matching circuit.

4.3 Experimental validation

A densely wound solenoid coil with 26 turns was wound around a PTFE bobbin with a diameter of 20 mm using 32 AWG (200 μm diameter) copper wire. The coil had a resistance and inductance of 1.0495 Ω and 18.88 μH when measured at 100 kHz using an LCR meter (SR720, Stanford Research Systems, Sunnyvale, California) with SR726 Kelvin clips. A photograph of this coil is shown in Figure 4.11.

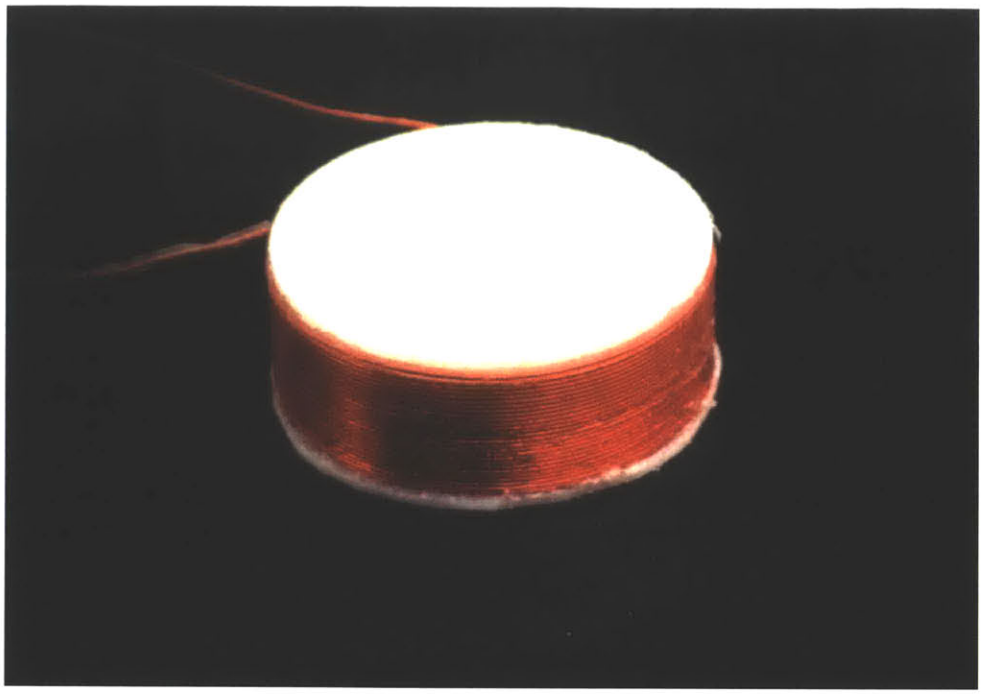

Figure 4.11. Photograph of solenoid coil on PTFE bobbin.

The coil was connected to the RF circuit across the tuning capacitor. The Impedance matching circuit was then tuned at 7.195 MHz to match Larmor frequency of the single sided magnet while observing the real and imaginary components of the impedance on a network analyzer (4396A, Hewlett Packard, Palo Alto, California).

Once suitably matched on the network analyzer, the circuit and NMR probe, mounted to the side of the single sided magnet, were connected to a NMR spectrometer (Kea2, Magritek, Wellington, New Zealand). The reflection coefficient as a function of frequency is shown in Figure 4.12 and Figure 4.13. In Figure 4.12, which indicates the reflection coefficient over a broad frequency range, it is evident that the match is suboptimal as the reflection coefficient at ω_0 is roughly one quarter that at an unmatched frequency. While observing the reflected signal at a smaller frequency range, as shown in Figure 4.13, the circuit was further tuned to bring the reflection coefficient down to approximately 2%. This indicates that the matching is effective as the reflection coefficient tends towards zero at the frequency to which the circuit was tuned, which, in this case was the Larmor frequency of the magnet (ω_0, 7.195 MHz).

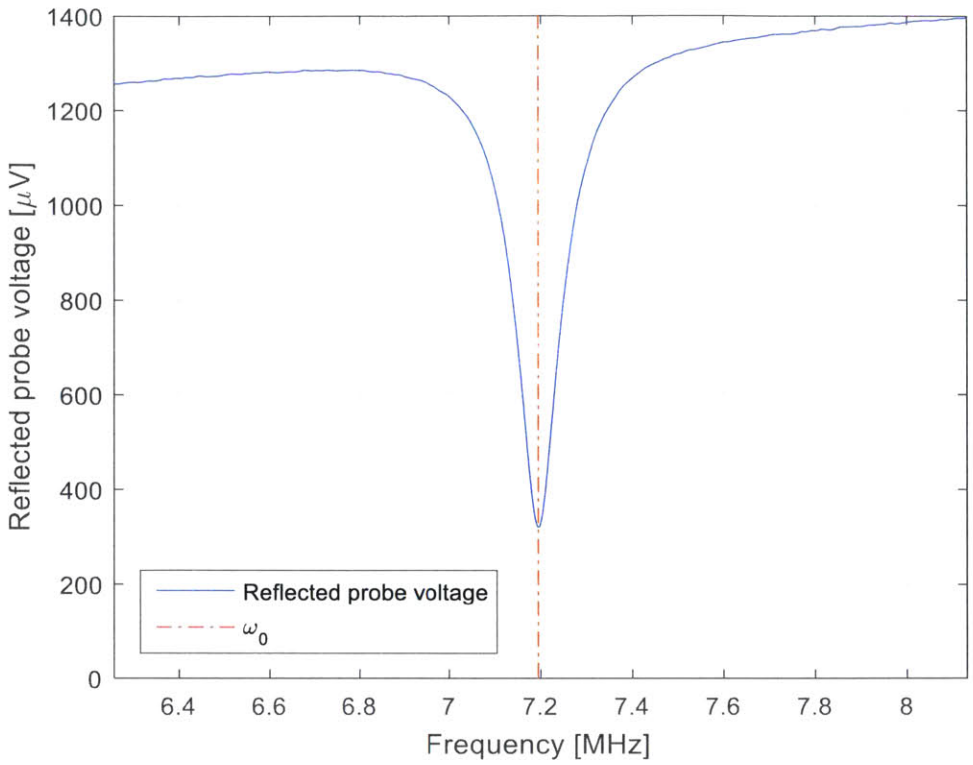

Figure 4.12. Measured reflection coefficient of tuned and matched NMR probe versus frequency.

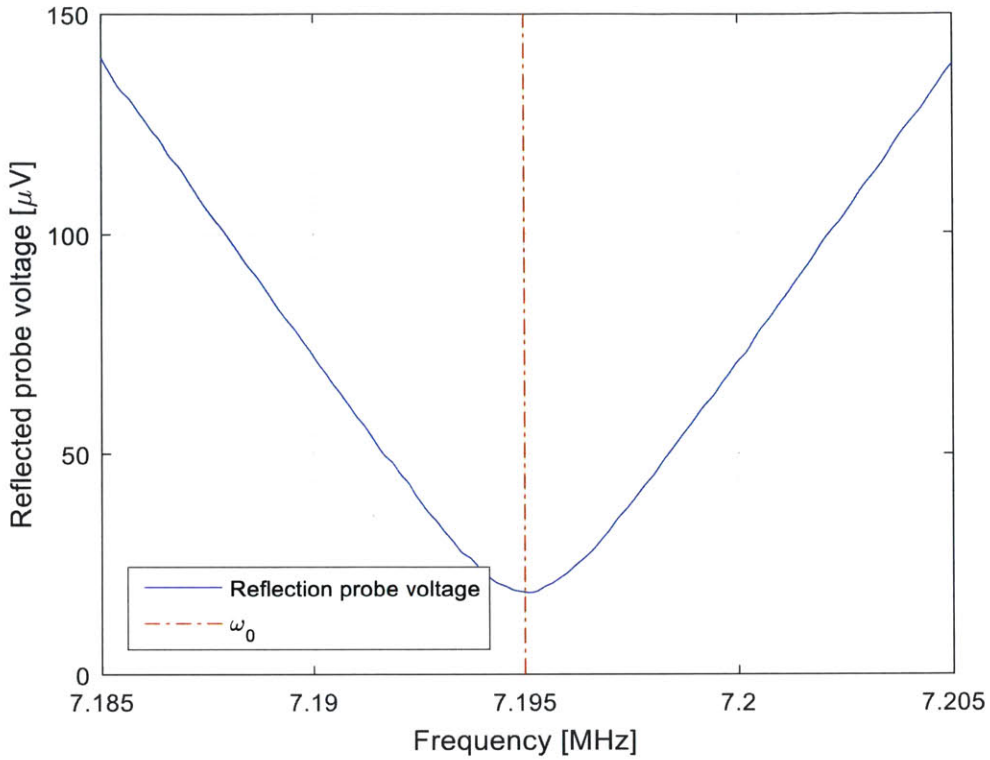

Figure 4.13. Measured reflection coefficient of precisely tuned and matched NMR probe versus frequency.

4.4 Future Work

4.4.1 Noise characterization

The primary functional requirement of the impedance matching is to transform the impedance of the load into that which maximizes power transmission with the source impedance. This operation cannot be performed without introducing noise into the signal. This is of particular concern in NMR applications as the measured signal is oftentimes on the order of a few microvolts.

Future development of the impedance matching circuit would begin with a characterization of amplitude of the noise introduced into the measurement by the circuit. Further work would seek to decrease this noise by improving the shielding and isolation of the circuit and by decreasing the length of the unshielded wires connecting the NMR probe to the circuit.

4.4.2 Automated tuning

The strength of the magnetic field fluctuates continuously due to environmental efforts, particular temperature. These fluctuations change the Larmor frequency. Therefore, the frequency of the B_1 pulse must be adjusted to compensate for this shift and to effectively rotate the nuclei into the transverse plane. Efficient transmission of this pulse from the spectrometer into the NMR probe requires a well matched and tuned impedance matching circuit. Currently the circuit is tuned manually which limits bot the accuracy to which it can be tuned and the rate at which that tuning can occur.

An automated system which can tune the circuit to transform a load to a new frequency with a well-defined precision would improve the quality and acquisition rate of NMR measurements. This improved tuning would enable a new set of analyses incorporating the amplitude of the signal since it would now only be affected by the current induced by the precession of the magnetization vector within the sample.

The existing circuit is constructed with easily accessible, variable capacitors designed to interface with a stepper motor. Next steps in development of the impedance matching circuit will focus on implementing this automated system in feedback with a measurement of the impedance of the circuit or its reflection coefficient.

This page intentionally left blank

Chapter 5

Conclusion

5.1 Overview

This thesis presented a new magnet design, associated matching circuitry, and initial NMR probe designs to enable single-sided remote NMR sensing within tissue. This system will find applications in sensing of fluid volume status, molecular oxygen, and pH for a wide range of clinical indications. ^{1}H NMR of the tissue, for hydration sensing, will directly measure water, the predominant source of protons within the body. Oxygen and pH measurements will require the use of a contrast agent encapsulated within a biopsy implantable sensor to provide field amplification and signal localization. Translation of either set of approaches towards clinical use requires a single-sided NMR sensor comprised of a magnet capable of producing a remote field and an appropriate transceiver coil.

The magnet design discussed in Chapter 3 provides a solution to the limited sensitivity and impractical geometric restrictions associated with previous approaches towards single-sided magnet design. The field profile of the constructed magnet matched the shape of the simulated magnet. The generated uniform field provides sufficient depth, field strength, and size to enable NMR measurements within tissue. Future work will improve the stabilization of the magnet against untoward temperature fluctuations and seek to better understand reasons for the discrepancy between simulated and measured field strength in the magnet.

The impedance matching circuit presented in Chapter 4 successfully transform the impedance of an NMR probe to that of the transmission line. This circuit enables high efficiency power transmission into the NMR probe and high sensitivity measurement of the induced voltage across the probe. Future work will pursue automated tuning to reduce variability and increase the speed of measurements.

5.2 Future hardware

Successful acquisition of an NMR signal will require the design of an NMR probe capable of both generating a uniform B_1 field in the same region that the magnetic field exists and receiving the induced free induction decay signal from the relaxation of the nuclei within the sample. This probe may consist of a single coil, known as a transceiver coil, or two separate coils for transmit and receive

capabilities. Further efforts in NMR probe design will begin with design of these coils. The transmit coil must be optimized for field uniformity while the receive coil must be optimized for sensitivity.

5.3 Fluid volume status measurement

Further efforts in hydration measurement will seek to extend our understanding of the physiological mechanisms regulating the balance of water between body compartments, such as the vascular, intracellular, and interstitial space, while also characterizing the ability of our system to measure a sample consisting of nuclei with differing relaxation times. We predict that accurate differentiation of differently bound water will be indicative of the location of the water within a particular compartment. It has been demonstrated that fluid within the body shifts between compartments during changes in fluid status [47].

A thoroughly validated understanding of the mechanisms of fluid balance during both hypervolemia and hypovolemic will motivate further studies in animal models and ultimately humans. A well-controlled study of our measurement technique in humans undergoing induced shifts in fluid balance will indicate its suitability as a tool to diagnose fluid imbalance or guide treatment.

Works Cited

[1] L. P. Kamolz and D. B. Lumenta, *Dermal replacements in general, burn, and plastic surgery: Tissue engineering in clinical practice*, vol. 9783709115. Vienna: Springer Vienna, 2013.

[2] H. W. Hopf, T. K. Hunt, J. M. West, P. Blomquist, W. H. Goodson, J. A. Jensen, K. Jonsson, P. B. Paty, J. M. Rabkin, R. A. Upton, K. von Smitten, and J. D. Whitney, "Wound Tissue Oxygen Tension Predicts the Risk of Wound Infection in Surgical Patients," *Arch Surg*, vol. 132, no. 9, pp. 997–1004, Sep. 1997.

[3] J. Z. Wang, X. A. Li, and N. A. Mayr, "Dose escalation to combat hypoxia in prostate cancer: A radiobiological study on clinical data," *Br. J. Radiol.*, vol. 79, no. 947, pp. 905–911, Nov. 2006.

[4] K. G. Elliott and A. J. Johnstone, "Diagnosing acute compartment syndrome," *J. Bone Jt. Surgery-British*, vol. 85, no. 5, pp. 625–632, 2003.

[5] J. a Bertout, S. a Patel, and M. C. Simon, "The impact of O2 availability on human cancer.," *Nat. Rev. Cancer*, vol. 8, no. 12, pp. 967–975, Dec. 2008.

[6] D. Lindner and D. Raghavan, "Intra-tumoural extra-cellular pH: a useful parameter of response to chemotherapy in syngeneic tumour lines.," *Br. J. Cancer*, vol. 100, no. 8, pp. 1287–1291, Apr. 2009.

[7] J. Chiche, M. C. Brahimi-Horn, and J. Pouysségur, "Tumour hypoxia induces a metabolic shift causing acidosis: A common feature in cancer," *J. Cell. Mol. Med.*, vol. 14, no. 4, pp. 771–794, Apr. 2010.

[8] M. W. Dewhirst, Y. Cao, and B. Moeller, "Cycling hypoxia and free radicals regulate angiogenesis and radiotherapy response.," *Nat. Rev. Cancer*, vol. 8, no. 6, pp. 425–437, Jun. 2008.

[9] B. Y. Jing, X. B. Kong, Z. Liu, and P. Mykland, "On the jump activity index for semimartingales," *J. Econom.*, vol. 166, no. 2, pp. 213–223, Jan. 2012.

[10] R. L. Schilsky, "Personalized medicine in oncology: the future is now.," *Nat. Rev. Drug Discov.*, vol. 9, no. 5, pp. 363–366, May 2010.

[11] X. Sun, S. Vilar, and N. P. Tatonetti, "High-Throughput Methods for Combinatorial Drug Discovery," *Sci. Transl. Med.*, vol. 5, no. 205, pp. 205rv1–205rv1, Oct. 2013.

[12] O. Jonas, H. M. Landry, J. E. Fuller, J. T. Santini, J. Baselga, R. I. Tepper, M. J. Cima, and R. Langer, "An implantable microdevice to perform high-throughput in vivo drug sensitivity testing in tumors," *Sci. Transl. Med.*, vol. 7, no. 284, pp. 284ra57–284ra57, Apr. 2015.

[13] W. Köstler, P. C. Strohm, and N. P. Südkamp, "Acute compartment syndrome of the limb," *Injury*, vol. 36, no. 8, pp. 992–998, Aug. 2005.

[14] S. a Olson and R. R. Glasgow, "Acute compartment syndrome in lower extremity musculoskeletal trauma.," *J. Am. Acad. Orthop. Surg.*, vol. 13, no. 7, pp. 436–444, Nov. 2005.

[15] A. Tiwari, A. I. Haq, F. Myint, and G. Hamilton, "Acute compartment syndromes," *Br. J. Surg.*, vol. 89, no. 4, pp. 397–412, Apr. 2002.

[16] G. J. Mar, M. J. Barrington, and B. R. McGuirk, "Acute compartment syndrome of the lower limb and the effect of postoperative analgesia on diagnosis," *Br. J. Anaesth.*, vol. 102, no. 1, pp. 3–11, Jan. 2009.

[17] N. Wisniewski, F. Moussy, and W. M. Reichert, "Characterization of implantable biosensor membrane biofouling," *Fresenius J. Anal. Chem.*, vol. 366, no. 6–7, pp. 611–621, Mar. 2000.

[18] A. Carreau, B. Hafny-Rahbi}, A. Matejuk, C. Grillon, and C. Kieda, "Why is the partial oxygen pressure of human tissues a crucial parameter? Small molecules and hypoxia, Why is the partial oxygen pressure of human tissues a crucial parameter? Small molecules and hypoxia," *J. Cell. Mol. Med. J. Cell. Mol. Med.*, vol. 15, 15, no. 6, 6, pp. 1239,1239–1253,1253, 2011.

[19] Y. Mendelson, "Pulse oximetry: theory and applications for noninvasive monitoring," *Clin. Chem.*, vol. 38, no. 9, pp. 1601–1607, Sep. 1992.

[20] S. Sakadžić, E. Roussakis, M. A. Yaseen, E. T. Mandeville, V. J. Srinivasan, K. Arai, S. Ruvinskaya, A. Devor, E. H. Lo, S. A. Vinogradov, and D. A. Boas, "Two-photon high-resolution measurement of partial pressure of oxygen in cerebral vasculature and tissue," *Nat. Methods*, vol. 7, no. 9, pp. 755–759, Aug. 2010.

[21] J. E. Sinex, "Pulse oximetry: Principles and limitations," *Am. J. Emerg. Med.*, vol. 17, no. 1, pp. 59–66, Jan. 1999.

[22] T. O. McBride, B. W. Pogue, E. D. Gerety, S. B. Poplack, U. L. Österberg, and K. D. Paulsen, "Spectroscopic diffuse optical tomography for the quantitative assessment of hemoglobin concentration and oxygen saturation in breast tissue," *Appl. Opt.*, vol. 38, no. 25, pp. 5480–5490, 1999.

[23] D. A. Boas, D. H. Brooks, E. L. Miller, C. A. DiMarzio, M. Kilmer, R. J. Gaudette, and Q. Zhang, "Imaging the body with diffuse optical tomography," *Signal Process. Mag. IEEE*, vol. 18, no. 6, pp. 57–75, 2001.

[24] V. H. Liu, C. C. Vassiliou, S. M. Imaad, and M. J. Cima, "Solid MRI contrast agents for long-term, quantitative in vivo oxygen sensing.," *Proc. Natl. Acad. Sci. U. S. A.*, vol. 111, no. 18, pp. 6588–93, 2014.

[25] C. C. Vassiliou, V. H. Liu, and M. J. Cima, "Miniaturized, biopsy-implantable

chemical sensor with wireless, magnetic resonance readout.," *Lab Chip*, vol. 15, no. 17, pp. 3465–72, 2015.

[26] C. C. Vassiliou, V. H. Liu, and M. J. Cima, "Miniaturized, biopsy-implantable chemical sensor with wireless, magnetic resonance readout.," *Lab Chip*, vol. 15, no. 17, pp. 3465–72, 2015.

[27] J. L. Kaplan, R. S. Porter, P. G. Szilagyi, and M. H. Beers, *The Merck manual of medical information*. Pocket Books, 2007.

[28] C. Yancy and W. T. Abraham, "Noninvasive hemodynamic monitoring in heart failure: utilization of impedance cardiography.," *Congest. Heart Fail.*, vol. 9, no. 5, pp. 241–50, 2003.

[29] J. J. You, P. C. Austin, D. A. Alter, D. T. Ko, and J. V Tu, "Relation between cardiac troponin I and mortality in acute decompensated heart failure," *Am Hear. J*, vol. 153, no. 4, pp. 462–470, 2007.

[30] J. Scallan, V. H. Huxley, and R. J. Korthuis, "Capillary Fluid Exchange: Regulation, Functions, and Pathology," in *Colloquium Series on Integrated Systems Physiology: From Molecule to Function*, 2010, vol. 2, no. 1, pp. 1–94.

[31] A. L. Hendrich, P. S. Bender, and A. Nyhuis, "Validation of the Hendrich II Fall Risk Model : A Large Concurrent Case / Control Study of Hospitalized Patients," *Appl. Nurs. Res.*, vol. 16, no. 1, pp. 9–21, 2003.

[32] D. Passe, M. Horn, J. Stofan, C. Horswill, and R. Murray, "Voluntary dehydration in runners despite favorable conditions for fluid intake," *Int. J. Sport Nutr. Exerc. Metab.*, vol. 17, no. 3, pp. 284–295, 2007.

[33] J. E. Greenleaf and F. Sargent, "Voluntary dehydration in man.," *J. Appl. Physiol.*, vol. 20, no. 4, pp. 719–724, 1965.

[34] J. Coresh, B. C. Astor, T. Greene, G. Eknoyan, and A. S. Levey, "Prevalence of chronic kidney disease and decreased kidney function in the adult US population: Third National Health and Nutrition Examination Survey," *Am J Kidney Dis*, vol. 41, no. 1, pp. 1–12, 2003.

[35] K. Kalantar-Zadeh, R. DL, K. CP, V. W. D, S. Bunnapradist, H. TB, and F. GC, "Fluid retention is associated with cardiovascular mortality in patients undergoing long-term hemodialysis.," *Circulation*, vol. 119, no. 5, pp. 671–679 9p, 2009.

[36] S. Chaudhry, Y. Wang, J. Concato, T. Gill, and H. Krumholz, "Patterns of weight change preceding hospitalizations for heart failure," *Circulation*, vol. 116, no. 14, pp. 1549–54, 2007.

[37] S. M. Shirreffs, "Markers of hydration status," *J. Sports Med. Phys. Fitness*, vol. 40, no. 1, pp. 80–84, 2000.

[38] Z. Laron, "Skin turgor as a quantitative index of dehydration in children," *Pediatrics*, vol. 19, no. 5, pp. 816–822, 1957.

[39] C. R. Gross, R. D. Lindquist, A. C. Woolley, R. Granieri, K. Allard, and B. Webster, "Clinical indicators of dehydration severity in elderly patients," *J. Emerg. Med.*, vol. 10, no. 3, pp. 267–274, 1992.

[40] M. H. Gorelick, K. N. Shaw, and K. O. Murphy, "Validity and Reliability of Clinical Signs in the Diagnosis of Dehydration in Children," *Pediatrics*, vol. 99, no. 5, pp. e6–e6, 1997.

[41] S. Cho and J. E. Atwood, "Peripheral edema," *Am. J. Med.*, vol. 113, no. 7, pp. 580–586, 2002.

[42] K. G. Brodovicz, K. Mcnaughton, and N. Uemura, "Reliability and Feasibility of Methods to Quantitatively Assess Peripheral Edema," *Clin. Med. Res.*, vol. 7, no. 1, pp. 21–31, 2009.

[43] W. F. Peacock and K. M. Soto, "Current techniques of fluid status assessment," *Contrib. Nephrol.*, vol. 164, pp. 128–142, 2010.

[44] S. M. Butman, G. A. Ewy, J. R. Standen, K. B. Kern, and E. Hahn, "Bedside cardiovascular examination in patients with severe chronic heart failure: Importance of rest or inducible jugular venous distension," *J. Am. Coll. Cardiol.*, vol. 22, no. 4, pp. 968–974, 1993.

[45] P. R. Lichstein., *Clinical Methods: The History, Physical, and Laboratory Examinations.*, vol. 4, no. 3. 1990.

[46] L. E. Rohde, L. Beck-da-Silva, L. Goldraich, T. C. Grazziotin, D. V Palombini, C. A. Polanczyk, and N. Clausell, "Reliability and prognostic value of traditional signs and symptoms in outpatients with congestive heart failure.," *Can. J. Cardiol.*, vol. 20, no. 7, pp. 697–702, 2004.

[47] S. Ishibe and A. J. Peixoto, "Methods of assessment of volume status and intercompartmental fluid shifts in hemodialysis patients: implications in clinical practice," in *Seminars in dialysis*, 2004, vol. 17, no. 1, pp. 37–43.

[48] W. D. V. M. Lichtenbelt, K. R. Westerterp, and L. Wouters, "Deuterium dilution as a method for determining total body water: effect of test protocol and sampling time," *Br. J. Nutr.*, vol. 72, no. 04, pp. 491–497, 1994.

[49] S. Borgonha, R. Kuriyan, C. Petracchi, A. Perro-Luzzi, and A. V Kurpad, "Total body water measurements by deuterium dilution in adult Indian males and females," *Indian J. Physiol. Pharmacol.*, vol. 41, pp. 47–51, 1997.

[50] F. M. Andrews, J. A. Nadeau, L. Saabye, and A. M. Saxton, "Measurement of total body water content in horses, using deuterium oxide dilution.," *Am. J. Vet. Res.*, vol. 58, no. 10, pp. 1060–1064, 1997.

[51] A.-S. Androne, S. D. Katz, L. Lund, J. LaManca, A. Hudaihed, K. Hryniewicz, and D. M. Mancini, "Hemodilution is common in patients with advanced heart failure," *Circulation*, vol. 107, no. 2, pp. 226–229, 2003.

[52] S. A. Kavouras, "Assessing hydration status," *Curr. Opin. Clin. Nutr. Metab. Care*, vol. 5, no. 5, pp. 519–524, 2002.

[53] J. H. Laragh and S. A. Atlas, "Atrial natriuretic hormone: a regulator of blood pressure and volume homeostasis.," *Kidney Int. Suppl.*, no. 25, 1988.

[54] M. Horowitz and S. Samueloff, "Plasma water shifts during thermal dehydration," *J. Appl. Physiol.*, vol. 47, no. 4, pp. 738–744, 1979.

[55] B. A. Shanholtzer and S. M. Patterson, "Use of bioelectrical impedance in hydration status assessment: reliability of a new tool in psychophysiology research," *Int. J. Psychophysiol.*, vol. 49, no. 3, pp. 217–226, 2003.

[56] H. El-Sayed, S. R. Goodall, and R. Hainsworth, "Re-evaluation of Evans blue dye dilution method of plasma volume measurement," *Clin. Lab. Haematol.*, vol. 17, no. 2, pp. 189–194, 1995.

[57] C. Jimenez, B. Melin, N. Koulmann, A. M. Allevard, J. C. Launay, and G. Savourey, "Plasma volume changes during and after acute variations of body hydration level in humans," *Eur. J. Appl. Physiol. Occup. Physiol.*, vol. 80, no. 1, pp. 1–8, 1999.

[58] L. E. Armstrong, R. J. Maughan, L. C. Senay, and S. M. Shirreffs, "Limitations to the use of plasma osmolality as a hydration biomarker," *Am. J. Clin. Nutr.*, vol. 98, no. 2, pp. 503–504, 2013.

[59] E. Perrier, A. Demazieres, N. Girard, N. Pross, D. Osbild, D. Metzger, I. Guelinckx, and A. Klein, "Circadian variation and responsiveness of hydration biomarkers to changes in daily water intake," *Eur. J. Appl. Physiol.*, vol. 113, no. 8, pp. 2143–2151, 2013.

[60] S. M. Shirreffs and R. J. Maughan, "Urine osmolality and conductivity as indices of hydration status in athletes in the heat.," *Med. Sci. Sports Exerc.*, vol. 30, no. 11, pp. 1598–1602, 1998.

[61] R. A. Oppliger, S. A. Magnes, L. A. Popowski, and C. V Gisolfi, "Accuracy of urine specific gravity and osmolality as indicators of hydration status," *Int J Sport Nutr Exerc Metab*, vol. 15, no. 3, pp. 236–251, 2005.

[62] F. H. Epstein, E. R. Levin, D. G. Gardner, and W. K. Samson, "Natriuretic peptides," *N. Engl. J. Med.*, vol. 339, no. 5, pp. 321–328, 1998.

[63] P. M. Kouw, J. P. Kooman, E. C. Cheriex, C. G. Olthof, P. M. De Vries, and K. M. Leunissen, "Assessment of postdialysis dry weight: a comparison of techniques.," *J. Am. Soc. Nephrol.*, vol. 4, no. 1, pp. 98–104, 1993.

[64] F. Lauster, R. Gerzer, J. Weil, H.-J. Fülle, and H. Schiffl, "Assessment of dry body-weight in haemodialysis patients by the biochemical marker cGMP," *Nephrol. Dial. Transplant.*, vol. 5, no. 5, pp. 356–361, 1990.

[65] C. Zoccali, F. Mallamaci, F. A. Benedetto, G. Tripepi, S. Parlongo, A. Cataliotti, S. Cutrupi, G. Giacone, I. Bellanuova, and E. COTTINI, "Cardiac natriuretic peptides are related to left ventricular mass and function and predict mortality in dialysis patients," *J. Am. Soc. Nephrol.*, vol. 12, no. 7, pp. 1508–1515, 2001.

[66] C. Crepaldi, M. Rosner, C. Teixeira, L. B. Martos, F. K. Martino, M. P. Rodighiero, and C. Ronco, "Is brain natriuretic peptide a reliable biomarker of hydration status in all peritoneal dialysis patients?," *Blood Purif.*, vol. 37, no. 3, pp. 238–242, 2014.

[67] S. W. Lee, J. H. Song, G. a Kim, H. J. Lim, and M.-J. Kim, "Plasma brain natriuretic peptide concentration on assessment of hydration status in hemodialysis patient.," *Am. J. Kidney Dis.*, vol. 41, no. 6, pp. 1257–1266, 2003.

[68] W. Kosiak, D. Swieton, and M. Piskunowicz, "Sonographic inferior vena cava/aorta diameter index, a new approach to the body fluid status assessment in children and young adults in emergency ultrasound—preliminary study," *Am. J. Emerg. Med.*, vol. 26, no. 3, pp. 320–325, 2008.

[69] A. Fenster and D. B. Downey, "3-D ultrasound imaging: A review," *Eng. Med. Biol. Mag. IEEE*, vol. 15, no. 6, pp. 41–51, 1996.

[70] M. Packer, W. T. Abraham, M. R. Mehra, C. W. Yancy, C. E. Lawless, J. E. Mitchell, F. W. Smart, R. Bijou, C. M. O'Connor, and B. M. Massie, "Utility of impedance cardiography for the identification of short-term risk of clinical decompensation in stable patients with chronic heart failure," *J. Am. Coll. Cardiol.*, vol. 47, no. 11, pp. 2245–2252, 2006.

[71] B. H. Greenberg, D. D. Hermann, M. F. Pranulis, L. Lazio, and D. Cloutier, "Reproducibility of impedance cardiography hemodynamic measures in clinically stable heart failure patients," *Congest. Hear. Fail.*, vol. 6, no. 2, pp. 74–82, 2000.

[72] R. M. Kelsey and W. Guethlein, "An evaluation of the ensemble averaged impedance cardiogram," *Psychophysiology*, vol. 27, no. 1, pp. 24–33, 1990.

[73] M. T. Allen, J. Fahrenberg, R. M. Kelsey, W. R. Lovallo, and L. J. P. Doornen, "Methodological guidelines for impedance cardiography," *Psychophysiology*, vol. 27, no. 1, pp. 1–23, 1990.

[74] J. D. Meler, M. A. Solomon, J. R. Steele, C. W. Yancy Jr, R. W. Parkey, and J. L. Fleckenstein, "The MR appearance of volume overload in the lower extremities," *J. Comput. Assist. Tomogr.*, vol. 21, no. 6, pp. 969–973, 1997.

[75] M. Li, C. C. Vassiliou, L. a. Colucci, and M. J. Cima, "^{1}H nuclear magnetic resonance (NMR) as a tool to measure dehydration in mice," *NMR Biomed.*, vol. 28, no. 8, pp. 1031–1039, 2015.

[76] N. Tavassolian, M. Li, C. C. Vassiliou, and M. J. Cima, "A novel magnetic relaxation-based platform for hydration monitoring," *IEEE Sens. J.*, vol. 14, no. 8, pp. 2851–2855, 2014.

[77] Z. Wang, P. Deurenberg, W. Wang, A. Pietrobelli, R. N. Baumgartner, and S. B. Heymsfield, "Hydration of fat-free body mass: new physiological modeling approach," *Am. J. Physiol. Metab.*, vol. 276, no. 6, pp. E995–E1003, 1999.

[78] E. Le Rumeur, J. De Certaines, P. Toulouse, and P. Rochcongar, "Water phases in rat striated muscles as determined by T2 proton NMR relaxation times," *Magn. Reson. Imaging*, vol. 5, no. 4, pp. 267–272, 1987.

[79] W. C. Cole, A. D. Leblanc, and S. G. Jhingran, "The origin of biexponential T2 relaxation in muscle water," *Magn. Reson. Med.*, vol. 29, no. 1, pp. 19–24, 1993.

[80] A.-L. Lin, Q. Qin, X. Zhao, and T. Q. Duong, "Blood longitudinal (T 1) and transverse (T 2) relaxation time constants at 11.7 Tesla," *Magn. Reson. Mater. Physics, Biol. Med.*, vol. 25, no. 3, pp. 245–249, 2012.

[81] M. N. Sawka, R. P. Francesconi, N. A. Pimental, and K. B. Pandolf, "Hydration and vascular fluid shifts during exercise in the heat," *J. Appl. Physiol.*, vol. 56, no. 1, pp. 91–96, 1984.

[82] B. Blümich, V. Anferov, S. Anferova, M. Klein, R. Fechete, M. Adams, and F. Casanova, "Simple NMR-MOUSE with a bar magnet," *Concepts Magn. Reson. Part B Magn. Reson. Eng.*, vol. 15, no. 4, pp. 255–261, Dec. 2002.

[83] F. Bloch, "Nuclear induction," *Phys. Rev.*, vol. 70, no. 7–8, pp. 460–474, 1946.

[84] N. Bloembergen, E. M. Purcell, and R. V. Pound, "Relaxation effects in nuclear magnetic resonance absorption," *Phys. Rev.*, vol. 73, no. 7, pp. 679–712, 1948.

[85] V. I. Chizhik, Y. S. Chernyshev, A. V. Donets, V. V. Frolov, A. V. Komolkin, and M. G. Shelyapina, *Magnetic resonance and its applications*. 2014.

[86] D. Freude and J. Haase, "Quadrupole Effects in Solid-State Nuclear Magnetic Resonance," in *NMR Basic Principles and Progress*, vol. 29, Springer, 1993, pp. 1–90.

[87] A. E. Marble, I. V. Mastikhin, B. G. Colpitts, and B. J. Balcom, "A compact permanent magnet array with a remote homogeneous field," *J. Magn. Reson.*, vol. 186, no. 1, pp. 100–104, 2007.

[88] K. Halbach, "Design of Permanent Multiple Magnets with Orientated Rare Earth Cobalt Material," *Nucl. Instruments Methods*, vol. 169, no. 1, pp. 1–10,

1980.

[89] J. C. Mallinson, "One-sided fluxes – {A} magnetic curiosity?," *IEEE Trans. Magn.*, vol. 9, no. 4, pp. 678–682, 1973.

[90] D. I. Hoult and R. E. Richards, "The signal-to-noise ratio of the nuclear magnetic resonance experiment," *J. Magn. Reson.*, vol. 24, no. 1, pp. 71–85, 1976.

[91] T. T. Song, M. R. Nelson, J. N. Hershey, and B. A. Chowdhury, "Subcutaneous tissue depth differences between males and females: The need for gender based epinephrine needle," *J. Allergy Clin. Immunol.*, vol. 113, no. 2, p. S241, 2004.

[92] R. L. French, R. E. Smith, and M. J. Buch, "Liquid-circulating thermal therapy system." Google Patents, 04-Jul-1989.